ABSTRACT

Title of dissertation: DECODING IMAGES OF DEBRIS DISKS

Christopher C. Stark
Doctor of Philosophy, 2010

Dissertation directed by: Douglas C. Hamilton
Department of Physics
University of Maryland

and

Marc J. Kuchner
Exoplanets & Stellar Astrophysics Laboratory
NASA Goddard Space Flight Center

Current observations of debris disks reveal a wealth of radial and azimuthal structures likely created by planet-disk interactions. Future images of exozodiacal disks may reveal similar structures. In this work I summarize my observations and modeling of the structure of exozodiacal dust clouds.

I present our observations of the 51 Ophiuchi circumstellar disk made with the Keck Interferometer operating in nulling mode at N-band. I modeled these data simultaneously with VLTI-MIDI visibility data and a *Spitzer* IRS spectrum and showed that the best-fit disk model is an optically thin disk with size-dependent radial structure. This model has two components, with an inner exozodiacal disk of blackbody grains extending to ∼4 AU and an outer disk of small silicate grains extending out to ∼1200 AU. This model is consistent with an inner "birth" disk of

continually colliding parent bodies producing an extended envelope of ejected small grains and resembles the disks around Vega, AU Microscopii, and β Pictoris.

I produced models of resonant ring structures created by planets in debris disks. I used a custom-tailored hybrid symplectic integrator to model 120 resonant ring structures created by terrestrial-mass planets on circular orbits interacting with collisionless steady-state dust clouds around a Sun-like star. I used these models to estimate the mass of the lowest-mass planet that can be detected through observations of a resonant ring, and showed that the resonant ring morphology is degenerate and depends on only two parameters: planet mass and $\sqrt{a_{\rm p}}/\beta$, where $a_{\rm p}$ is the planet's semi-major axis and β is the ratio of radiation pressure force to gravitational force on a grain. I introduced a new computationally-efficient "collisional grooming" algorithm that enables us to model grain-grain collisions in structured debris disks and used this algorithm to show how collisions can alter the morphology of a resonant ring structure. My collisional models reveal that collisions act to remove azimuthal and radial asymmetries from the disk. I showed that the collision rate for background particles in a resonant ring structure is enhanced by a factor of a few compared to the rest of the disk, and dust grains in or near mean motion resonances have even higher collision rates. I also used this algorithm to model the 3-D structure of the Kuiper Belt's dust cloud at four different dust levels. I found that our Kuiper Belt dust would look like an azimuthally symmetric ring at 40–45 AU when viewed from afar at submillimeter wavelengths. At visible wavelengths, our Kuiper Belt dust cloud would reveal two resonant ring structures: one created by Saturn near 10 AU and one created by Neptune near 30 AU. A denser version of

our Kuiper Belt dust cloud, with an optical depth 1000 times greater, would look qualitatively similar at submillimeter wavelengths, but would be void of Neptune's resonant ring structure at visible wavelengths. My simulations suggest that mean motion resonances with planets can play strong roles in the sculpting of debris disks even in the presence of collisions, though their roles are somewhat different than what has been anticipated.

DECODING IMAGES OF DEBRIS DISKS

by

Christopher C. Stark

Dissertation submitted to the Faculty of the Graduate School of the
University of Maryland, College Park in partial fulfillment
of the requirements for the degree of
Doctor of Philosophy
2010

Advisory Committee:
Professor Douglas C. Hamilton, Chair/Co-Advisor
Dr. Marc J. Kuchner, Co-chair/Advisor
Professor Douglas P. Hamilton
Professor Kara D. Hoffman
Professor Gregory W. Sullivan

Dedication

For my wife, Angela, who pulled up her stakes and moved halfway across the country so I could pursue my interests, whose encouragement propelled me to where I am, who trusted me to complete this journey.

Acknowledgments

A great many people in my life made this work possible and I am indebted to all of them for their help, support, and guidance.

First and foremost I'd like to thank my advisor, Marc Kuchner, for providing me with so many fantastic research opportunities that seemed like a dream only a few years ago. I am grateful to him for taking me under his wing on his first day at NASA. He has provided me with limitless help, challenged me, and molded me into a better scientist. I am most thankful to him for leading me into this area of research that I enjoy so much. Marc has been a pleasure to worth with and I am glad to call him a mentor and a friend.

I owe thanks to my colleagues at Goddard, Aki Roberge, Hannah Jang-Condell, and John Debes, for their great mentoring, valuable expertise, and friendship. I appreciate all the advice they have given me and thank them for helping to integrate me into the astronomy community.

I am also thankful to all of those who have helped me throughout my academic career. I can attribute much of my interest in physics to the faculty at the University of Northern Iowa Department of Physics, especially to my inspiring undergraduate advisor, Paul Shand. Thank you to all of the wonderful faculty and staff at the University of Maryland who made my graduate student experience so rewarding. Thanks are due to the Doug Hamiltons; I would like to thank Douglas C. Hamilton for his academic guidance throughout my graduate career and Douglas P. Hamilton for the insightful conversations we have shared.

I would like to thank my friends, Christian Long, Kyle Gustafson, and Ori Fox. Our countless conversations and games of ping-pong provided an outlet for creative thought that spurred many fresh ideas. I thank them for the friendship and support they provided as we traversed graduate student life.

I am profoundly grateful to my family. I owe a great deal of thanks to my father, who taught me basic physical and mathematical concepts at a young age through the many projects we worked on together, as well as the importance of logic and critical thinking. I am grateful to my mother for her encouragement and love, and for instilling within me the belief that I could do anything I set my mind to. And I am thankful to my brother, who got me involved in computer programming at an age when I was only interested in making video games and getting into trouble, and without whom I would have never enrolled in the physics course that set all of this in motion.

Lastly, I would like to thank my wife who was by my side prior to my interest in physics, and who stayed by my side even after realizing what she had gotten herself into. The past six years of study have been remarkably challenging at times. Without her, they would have been overwhelmingly daunting. Her support and love have been crucial to my success.

I would like to acknowledge financial support from the NASA Graduate Student Researchers Program (GSRP), the Harvard-Smithsonian Center for Astrophysics, and NASA's Navigator Program. I would also like to acknowledge the NASA Center for Computational Sciences, which provided the computational resources that enabled much of this work.

Table of Contents

List of Tables

List of Figures

Chapter 1

Introduction

1.1 Debris disks

Approximately 15–20% of nearby Sun-like stars exhibit excess emission at infrared wavelengths that has been interpreted as emission from a circumstellar disk of dust (Trilling et al., 2008). These dusty circumstellar disks, or debris disks, are believed to be mature planetary systems harboring planets and planetesimals, the remnants of planet formation. Typical dust lifetimes are much shorter than the age of these systems, so the dust must be continually replenished, likely by the outgassing and colliding of planetesimals (Backman & Paresce, 1993).

Planets embedded in a debris disk gravitationally interact with the planetesimals and dust. Planets can stir up a population of planetesimals, enhancing the collision and dust production rates (Kenyon & Bromley, 2001). Planets can act as a shield, preventing dust grains or planetesimals from penetrating into a region of orbital space (e.g. Moro-Martín & Malhotra, 2002; Quillen, 2006). Also, planets may trap dust in exterior mean motion resonances (MMRs), amplifying the dust density at specific locations (e.g. Jackson & Zook, 1989; Kuchner & Holman, 2003). These interactions can lead to large-scale structure in the debris disk, such as clumps of dust, gaps, circumstellar rings, and stellocentric offsets of the disk (e.g. Deller & Maddison, 2005; Stark & Kuchner, 2008; Chiang et al., 2009).

The discovery of circumstellar debris disks around nearby stars has revolutionized astronomy. Disks provide us with the opportunity to study the formation, evolution, and composition of planetary systems. And searching for asymmetries in debris disks may be a promising method for discovering and characterizing otherwise undetectable extrasolar planets (exoplanets) (e.g. Quillen, 2006; Chiang et al., 2009).

However, these disks may also be a troublesome source of noise for upcoming exoplanet-imaging efforts; future missions that aim to directly image Earth-like exoplanets will have to contend with the diffuse glow of dust in debris disks. Structure within these disks may only further complicate our ability to distinguish a planet's signal from the surrounding disk.

In this dissertation, I present my work on detecting and "decoding" the structure of debris disks. Chapter 2 presents my observations and models of one of the first debris disks to be resolved in the inner few AU. In Chapter 3, I introduce my numerical techniques for modeling tenuous, structured debris disks and present my simulations and analysis of the geometry of resonant ring structures induced by terrestrial-mass planets. In Chapter 4, I expand my models to include collisional debris disks by creating a novel algorithm for modeling grain-grain collisions. Finally, I apply these collisional models to the Solar System's Kuiper Belt in Chapter 5. I predict what our Kuiper Belt would look like from 10 pc in its current state and what it may have looked like at a younger age when the collision rate was hundreds of times higher.

The remainder of this introductory chapter introduces key concepts and back-

ground material in debris disks and disk-planet interactions. My goal is to provide context for the results presented in Chapters 2–5.

1.2 The dynamics of dust grains in our zodiacal cloud

The Solar System is an evolved debris disk with a warm, inner disk of dust extending from the dust sublimation radius (approximately 0.03 AU for a 10 μm silicate grain) to the asteroid belt and a cool, outer dust component likely associated with Kuiper Belt objects. The inner few AU of the Solar System's debris disk, the zodiacal cloud, is composed of a mixture of dust produced by collisions between asteroids in the asteroid belt, outgassing of comets as they approach the Sun, and the tidal disruption of Jupiter-family comets (e.g. Nesvorny et al., 2009). The relative contributions of these sources is still debated, with estimates of the ratio of asteroid to cometary dust ranging from 1:10 to 7:10 (Ipatov et al., 2008).

Our zodiacal cloud is not a smooth, uniform disk of dust. The geometric center of the zodiacal cloud is shifted from the Sun by approximately 0.01 AU and inclined with respect to the ecliptic by approximately 2° (Kelsall et al., 1998). Observations of our zodiacal cloud obtained with the Infrared Astronomical Satellite (IRAS) revealed several bright bands of dust at distinct declinations (Low et al., 1984). These bands have been associated with the inclinations of specific asteroid families, such as the Koronis, Eos, and Themis families, and provide direct evidence for the production of dust in the asteroid belt (Dermott et al., 1984).

Dust grains in the zodiacal cloud experience a number of forces in addition to

gravitational forces. Upon the release of a dust grain from its parent body, radiation pressure immediately changes the orbit of the dust grain. Radiation pressure, which scales as $1/r^2$, effectively reduces the gravitational influence of the star and increases the semi-major axis and eccentricity of the dust grain's orbit according to

$$a = a_0 \, \frac{1-\beta}{1-2a_0\beta/r} \tag{1.1}$$

and

$$e = \left[1 - \frac{(1-2a_0\beta/r)\,(1-e_0^2)}{(1-\beta)^2}\right]^{1/2} , \tag{1.2}$$

where we have assumed that the dust grain's velocity is conserved upon launch, a_0 and e_0 are the semi-major axis and eccentricity prior to launch, respectively, r is the stellocentric distance, and β is the ratio of radiation pressure force to the gravitational force on the grain. For spherical grains, β is given by

$$\beta = \frac{3L_\star Q_{\rm PR}}{16\pi G M_\star c \rho s} , \tag{1.3}$$

where $L_\star$ is the stellar luminosity, $M_\star$ is the stellar mass, G is the gravitational constant, c is the speed of light, ρ is the mass density of a grain, s is the grain radius, and $Q_{\rm PR}$ is the radiation pressure coefficient (Burns et al., 1979).

For grains on initially circular orbits, the smallest grains, with $\beta > 0.5$, will no longer be bound to the system and will leave on hyperbolic orbits. Of those grains still bound to the star ($\beta < 0.5$), the orbits of the smallest grains will undergo the largest changes in eccentricity, causing them to spread out and occupy a larger range of stellocentric distances. Large grains will remain relatively unaffected and will appear to trace the paths of their parent bodies.

Dust grains will also experience corpuscular and radiative drag forces. As a dust grain orbits a star, it travels through a soup of solar wind ions that collide with the grain, producing a solar wind drag force (see, e.g. Gustafson, 1994). The dust grain will also feel the relativistic Poynting-Robertson (PR) drag force (Robertson, 1937). A dust grain in orbit around a star will absorb some of the incident starlight and warm to an equilibrium temperature. In the process the dust grain emits radiation isotropically in its rest frame. However, in the system's inertial reference frame, the grain emits more radiation (and momentum) in the forward direction. The grain slowly loses momentum and spirals in toward the star in an amount of time known as the PR time, which can be expressed as (Wyatt & Whipple, 1950)

$$t_{\rm PR}(r) = \frac{c\, r^2}{4GM_\star \beta_{\rm eff}} \ , \tag{1.4}$$

where $\beta_{\rm eff} = \beta(1 + {\rm sw})$ and sw is the ratio of corpuscular drag to PR drag, typically ~ 0.3 for solar type stars (Gustafson, 1994). The median silicate grain size in our zodiacal cloud is on the order of 10 μm, which would reach the Sun in less than 10^5 years if launched from the asteroid belt.

Dust grains may also be removed by collisions with other dust grains. The collision time for a dust grain in a uniform disk is approximately

$$t_{\rm coll} \approx \frac{t_{\rm orbit}}{4\pi\tau} \ , \tag{1.5}$$

where $t_{\rm orbit}$ is the orbital period of the dust grain and τ is the geometric, face-on optical depth of the disk (Wyatt, 2003). Our tenuous zodiacal cloud has an optical depth on the order of 10^{-7}; the collision time for a typical asteroidal dust grain is on the order of a few million years, significantly longer than the PR time. Hence,

collisions are typically ignored when simulating debris disks similar to our zodiacal cloud.

As drag forces remove momentum from the dust grains, the grains spiral inward toward the star. Along the way the grains gravitationally interact with any existing planets. Planets may simply eject grains from the system via close encounters, directly collide with dust grains, or produce complex dynamical effects when the dust grains migrate into external MMRs with the planet. Roughly speaking, an MMR occurs when the ratio of the dust grain's orbital period to the planet's orbital period is approximately a ratio of two integers. For example, the 3:2 resonance implies that the dust grain's orbital period is approximately 1.5 times longer than the planet's orbital period.

MMRs produce a periodic gravitational forcing, and can trap the inward-spiraling dust grains for an extended period of time at a nearly-fixed semi-major axis. While trapped in resonance, the combination of drag forces and the gravitational periodic forcing pump up the dust grain's eccentricity until the grain's orbit becomes planet-crossing, at which point the grain may be removed from resonance. The dust grain may be ejected from the system altogether, continue to spiral inward, or move to another resonance.

Figure 1.1 illustrates the resonant trapping of dust grains. This figure shows a sample simulation of four dust grains orbiting in the Sun-Earth system. Drag forces cause the semi-major axes of the grains to decay over time. The Earth temporarily halts the migration of all four dust grains, trapping them in exterior MMRs until they are chaotically ejected from resonance. Figure 1.1 illustrates that resonant

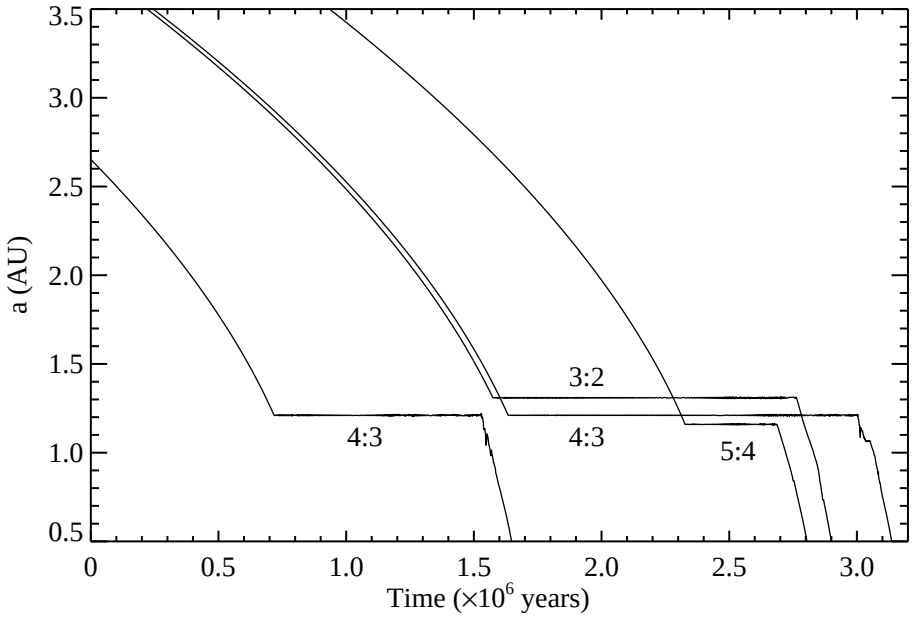

Figure 1.1: Resonant trapping of dust grains by an Earth-mass planet on a circular orbit around the Sun at 1 AU. Four 120 μm blackbody grains are launched exterior to the planet's orbit; drag forces migrate the grains inward over time. Grains become trapped in exterior MMRs (labeled) for a significant fraction of their lifetimes.

trapping may occupy a significant fraction of the dust grain's lifetime.

This temporary trapping of dust grains creates a build-up of grains in semi-major axis space. As a result, an overdense circumstellar ring of dust forms near the semi-major axis of the planet. Figure 1.2 shows the face-on surface density for one such ring, created by an Earth-mass planet on a circular orbit at 1 AU around the Sun in a cloud of 40 μm blackbody grains. This figure also illustrates the azimuthal asymmetries that resonances can create in a dust cloud, including clumps of dust trailing the planet and a gap near the planet's location.

A resonant dust ring created by the Earth has been detected in our zodiacal cloud. In 1998, infrared observations of our zodiacal cloud made by the Diffuse Infrared Background Experiment (DIRBE) on board the Cosmic Infrared Background Explorer (COBE) showed two surface brightness enhancements in the infrared sky, leading and trailing the Earth (Reach et al., 1995). These enhancements, shown in Figure 1.3, are evidence for a ring of dust in resonant lock with the Earth (like that shown in Figure 1.2); they have been interpreted as projections of an overdense torus of dust, as viewed from the Earth's perspective (Reach et al., 1995). The surface brightness enhancements also exhibit the leading-trailing asymmetry predicted by models of the Earth's resonant ring (Jackson & Zook, 1989; Dermott et al., 1994).

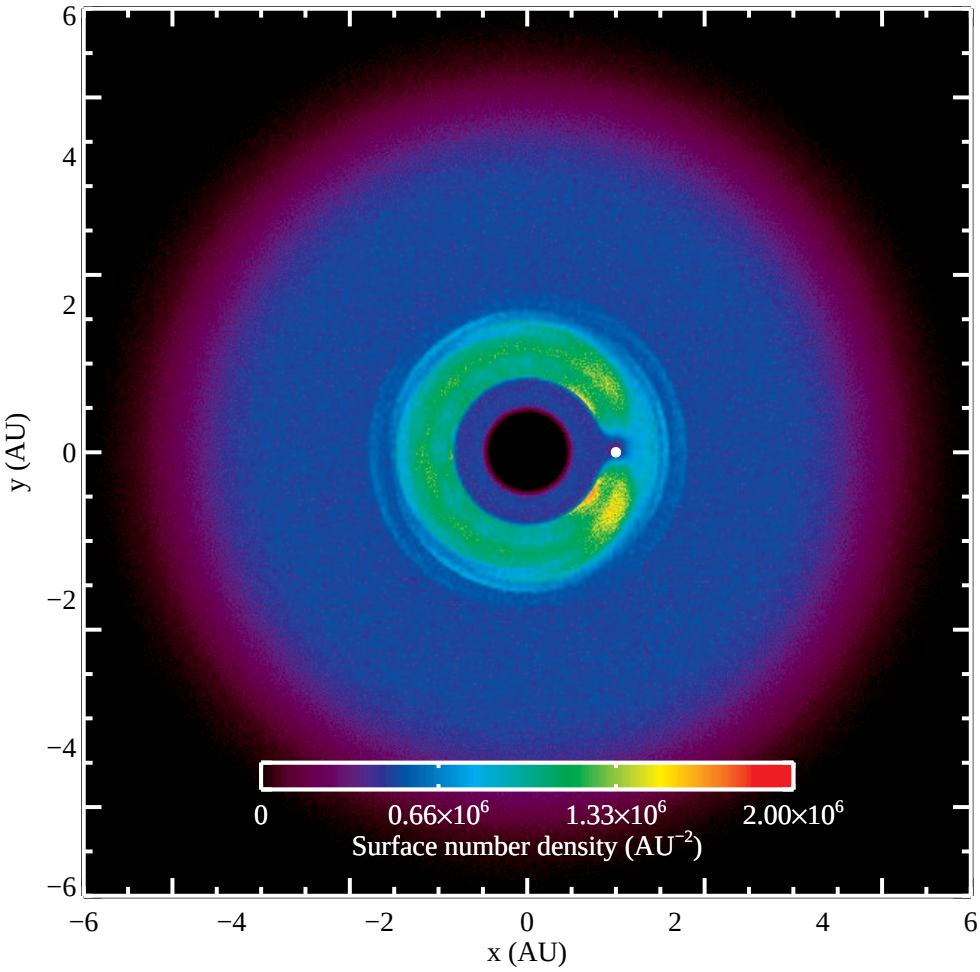

Figure 1.2: Face-on surface density of a debris disk model with a resonant ring structure created by a 1 $M_\oplus$ planet orbiting a Sun-like star at 1 AU in a cloud of 40 μm blackbody grains. The Earth, marked with a white dot, orbits counter-clockwise. Dust grains interior to 0.5 AU were removed from the model; the central hole is artificial.

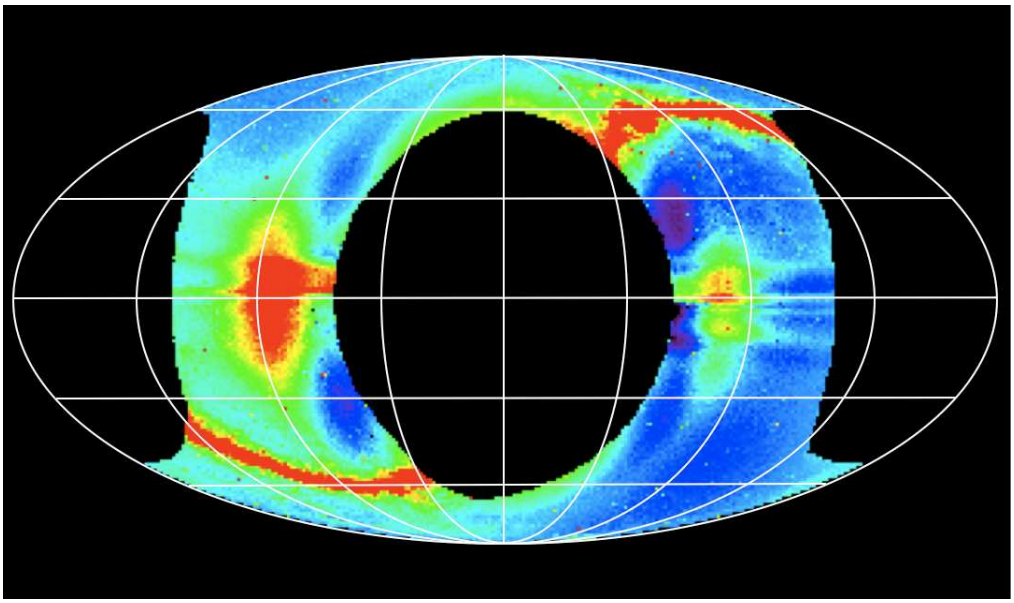

Figure 1.3: COBE-DIRBE image of our zodiacal cloud at 12 μm after subtraction of the smooth component of the best-fit model to the data. Black marks regions of missing data. The center of the image is in the direction of the Sun, the left side trails the Earth's orbit, and the right side leads the Earth's orbit. The galactic plane appears as a red curve extending from the bottom left of the image to the top right. The Earth's resonant dust ring appears as two surface brightness enhancements leading and trailing the Earth's orbit. The trailing enhancement is brighter, in agreement with models.

1.3 Exozodiacal clouds: a complication for future exo-Earth-imaging missions

A major science driver for flagship NASA missions over the next few decades will probably be the detection and characterization of extrasolar Earth-like planets (exo-Earths) via direct imaging. The zodiacal cloud, although tenuous, has a large emitting and scattering surface area; when viewed from a distance, a face-on 0.4 × 0.4 AU patch of our zodiacal cloud scatters as much sunlight as the Earth. If exoplanetary systems harboring Earth-like planets are anything like the Solar System, these future missions will have to cope with the scattered and emitted light from dust within the habitable zone.

Extrasolar zodiacal clouds, or exozodiacal clouds, may well be more dense than our own zodiacal cloud, potentially obscuring the planet signal altogether. At least 10–20% of nearby stars harbor an outer debris disk much denser than the Solar System's (Beichman et al., 2006). In both images and spectra, light from the zodiacal and exozodiacal dust will likely dominate an exo-Earth's signal. The magnitude of the exozodiacal emission within the point-spread function of a 4-m telescope is V≈28, assuming a Solar System twin viewed at an inclination of 60° from face-on. That is two magnitudes brighter than the Earth viewed at quadrature from 10 pc away (Roberge et al., 2009).

For these reasons, the detection of exozodiacal clouds and determination of typical exozodiacal dust levels is of significant importance in planning for future exo-Earth imaging missions. In the near future, interferometric observation tech-

niques will likely lead the way in exozodiacal dust detection. Currently the nulling interferometer at the twin Keck telescopes is the most sensitive instrument that spatially resolves exozodiacal clouds, capable of detecting disks with optical depths down to several hundred times the optical depth of our zodiacal cloud (several hundred "zodis"). I present our detection of one such exozodiacal cloud, made with the Keck Interferometer Nuller, in Chapter 2. Future ground-based interferometers, like the Large Binocular Telescope Interferometer, aim to achieve exozodiacal disk detection down to 10 zodis (Lunine et al., 2008), while proposed space-based probes, like the Fourier Kelvin Stellar Interferometer, aim to detect exozodiacal disks similar to our own zodiacal cloud (Defrère et al., 2008).

In addition to the unknown overall density of exozodiacal clouds, these dust clouds may have structures similar to what we see in our own zodiacal cloud. Will future missions be able to detect a terrestrial-mass planet in spite of these structures? Proposed interferometric missions have suggested filtering out point-symmetric components of the surface brightness, leaving a relatively clean asymmetric signal that contains the planet (Defrère et al., 2010). However, asymmetric structures in the dust cloud may present problems for these missions and may limit them to exozodiacal dust levels less than a few tens of zodis (Defrère et al., 2010). In addition, bright clumps of dust may present false positives for future direct imaging coronagraphs.

While exozodiacal dust structures may be a major source of confusion in direct imaging of exoplanets, they may also provide another method by which we can indirectly detect exoplanets. In fact, information gleaned from disk structure can be used to detect planets that would otherwise be too faint or have a mass that is

too low to be detected using other techniques. We may be able to use the shape and location of the dust structure to constrain the mass and orbit of the perturbing planet, as well as the properties of the dust grains and planetesimals from which they are launched (Stark & Kuchner, 2008). The distribution of planetesimals also tells us about the history of the planetary system (Wyatt, 2003) and provides insight into the planet formation process.

The mere presence of a debris disk is inherently important to planet finding as well. The relatively short removal time of dust grains in a debris disk as compared to the age of the system implies that larger parent bodies must also be present; the detection of an exozodiacal disk is a direct indication of planet-building material.

1.4 Searching for planets with currently detectable debris disk structures

Debris disk images have emerged as important tools for finding extrasolar planets at angular separations greater than a few arcseconds from their host stars. A 2005 Hubble Space Telescope (HST) image of Fomalhaut's debris disk made with the Advanced Camera for Surveys (ACS) showed a ring offset from the central star suggesting perturbations from a hidden planet (Kalas et al., 2005); two years later, new ACS images revealed one of the first ever directly imaged exoplanets orbiting inside the disk (Kalas et al., 2008). Fomalhaut is not the only resolved debris disk to exhibit structure. In fact, the majority of the debris disks imaged to date with HST coronagraphy display a diversity of asymmetric features (Greaves et al., 1998;

Holland et al., 1998; Telesco, et al., 2000; Heap et al., 2000; Kalas et al., 2005; Golimowski et al., 2006; Schneider et al., 2009).

Almost all of the known debris disks have temperatures implying spatial scales like those in the Kuiper Belt, i.e. on the order of 10–100 AU in extent. Current instruments limit us to resolving only the largest ($\gtrsim$ 5 arcsec, or 50 AU at 10 pc) of those disks. The circumstellar dust ring observed around Fomalhaut, for example, has an inner semi-major axis of 133 AU, roughly three times larger than the Kuiper Belt.

Current instruments also limit us to imaging only the brightest disks. The current collection of resolved debris disks, including the disks around the stars Fomalhaut, AU Microscopii, β Pictoris, Vega, and ϵ Eridani, have optical depths on the order of 10^{-4}; these disks are thousands of times more dense than the Kuiper Belt. Dust grains in these dense disks have typical collision times that are hundreds of times shorter than their PR times. For example, for a 10 μm grain in the Fomalhaut system, Equation 1.5 gives a collision time on the order of 10^5 years, while Equation 1.4 gives a PR time on the order of 10^7 years.

These short collision times imply that the observed dust distribution likely resembles the parent body distribution (Wyatt, 2005). Can we learn about the distribution of planetesimals and possibly the dynamical history of the system by observing the dust grains? The debris disk structure around Fomalhaut provides an excellent example of recent attempts to do so: Kalas et al. (2005)'s scattered light observations of the Fomalhaut disk revealed a sharp inner edge to the ring structure at a single semi-major axis. This prompted studies suggesting that an unseen

planetary companion may have sculpted the parent bodies into this well-defined circumstellar ring structure by gravitationally ejecting planetesimals interior to the inner edge (e.g. Quillen, 2006). Every planet creates a "chaotic zone" exterior to its orbit in which MMRs overlap, forming a region of orbital space that is unstable on secular timescales (Wisdom, 1980). Chiang et al. (2009) fit the observed distribution of dust (and the inferred distribution of parent bodies) in the Fomalhaut system with numerical simulations of the parent bodies and dust, and were able to constrain the mass and semi-major axis of the planet based on the appearance of the ring structure. However, future investigations may reveal other possible mechanisms that can create similar looking dust structures, e.g. outward migration of the planet or resonant trapping of dust grains/parent bodies.

The short collision times in observed debris disks also imply that grain-grain collisions are the dominant mechanism for the removal of dust grains. Understanding the appearances of these debris disks will require models that can treat the dynamics of planetary perturbations and grain-grain collisions simultaneously. In Chapter 4, I present a new "collisional grooming" algorithm that allows for the self-consistent inclusion of both of these physical processes. This algorithm will allow us to model the dense disks that will be observed in the near future and provide a more complete means for interpreting disk structures.

Chapter 2

Spatially resolved detection of an exozodiacal cloud with the Keck Interferometer Nuller

2.1 Introduction

51 Ophiuchi (51 Oph), a rapidly rotating B9.5Ve star located at 131^{+17}_{-13} pc (Perryman et al., 1997), shows an infrared (IR) excess ($L_{\rm IR}/L_\star \approx 2\%$) in its spectral energy distribution (SED) due to the presence of silicate grains (Fajardo-Acosta et al., 1993; Meeus et al., 2001; Keller et al., 2008). This system probably represents a rare nearby example of a young debris disk with gas, a planetary system just entering the late stages of formation, after the primordial gas has substantially dissipated, but before terrestrial planets have finished accreting. Its nearly edge-on disk of gas and dust and its variable absorption features (Grady & Silvis, 1993; Roberge et al., 2002) suggests that 51 Oph may be an analog of β Pictoris (β Pic).

Several spectroscopic observations support the presence of an edge-on gaseous disk around 51 Oph. Double-peaked Hα emission marks the presence of ionized hy-

drogen gas in Keplerian orbit (Leinert et al., 2004). Sharp CO bandhead emission features rule out a spherically symmetric wind and reveal a gaseous disk with temperature ranging from 2000 – 4000 K interior to the dust sublimation radius (Thi et al., 2005). The CO bandhead observations also point to a disk with inclination $i = 88^{+2}_{-35}{}^{\circ}$ (Thi et al., 2005) or $i = 83^{+7}_{-0}{}^{\circ}$ (Berthoud et al., 2007). A spectral line analysis performed by Dunkin et al. (1997) revealed a large projected rotational velocity for the star of $v \sin i = 267 \pm 5$ km s^{-1}. Gas absorption features observed by Grady & Silvis (1993) and Roberge et al. (2002) are also consistent with an edge-on disk.

The spatial structure of the 51 Oph dust disk remains puzzling. An HST ACS V-band non-detection (Doering et al., 2007) and a Keck 18 μm non-detection (Jayawardhana et al., 2001) suggest that the disk is relatively compact. However, far-IR photometry reveals cold dust grains extending out to thousands of AU (Waters et al., 1988; Lecavelier des Etangs et al., 1997).

Leinert et al. (2004) obtained the first spatially-resolved measurements of the 51 Oph disk with the Mid-IR Interferometric (MIDI) instrument on the Very Large Telescope Interferometer (VLTI). The large visibility values they measured (~ 0.65) imply that the 51 Oph disk is relatively compact along the VLTI-MIDI projected baseline (101.2 m, 23° E of N). Leinert et al. (2004) fit the VLTI-MIDI visibility with a Gaussian disk and found the FWHM to be 7 mas, or 0.9 AU, at 12.5 μm.

Here we present new spatially-resolved observations of 51 Oph using the Keck Interferometer Nuller that help to constrain the geometry of the dust disk. We compare these to the VLTI-MIDI observations (Leinert et al., 2004) and *Spitzer*

IRS observations (Keller et al., 2008). We simultaneously model all three data sets using two simple, edge-on disk models: an optically-thin model based on our zodiacal cloud and a two-layer model based on the Chiang & Goldreich (1997) disk model.

2.2 Observations

Observations of 51 Oph were conducted using the twin Keck telescopes atop Mauna Kea, Hawaii, operated in nulling interferometric mode on 2 Apr 2007. 51 Oph was observed twice in the N-band (8 - 13 μm) at an hour angle of ≈ 0.5, with a projected baseline of 66.2 m at a position angle of 47°. A calibrator star, Epsilon Ophiuchi (HD146791), was observed once following the target observations. Table 2.1 lists the details of our observations.

Table 2.1: Keck Interferometer Nuller Observation Log

Object	Type	Time (UT)	u (m)	v (m)	Air Mass
51 Oph	target	15:08:24	52.00	48.97	1.39
51 Oph	target	15:09:26	51.90	48.87	1.39
ϵ Oph	calibrator	15:37:21	37.34	59.76	1.21

The Keck Nuller operates with each Keck telescope aperture divided into two sub-apertures for a total of four apertures (see Serabyn et al., 2005; Colavita et al., 2008, for details). Long-baseline fringes formed by combining the light from opposite telescopes are used to null the light from the central star and observe any spatially resolved structures. Short-baseline fringes formed by combining the light

from two neighboring sub-apertures are used to remove the thermal background.

The observable quantity is the "null leakage," the ratio of the amplitude of the short baseline fringe with the long baseline null fringe on target to the amplitude of the short baseline fringe with the long baseline constructive fringe on target (see Serabyn et al., 2005; Barry et al., 2008, for details). We estimated and subtracted the systematic null leakage by comparing the measured null leakage of the calibration star, ϵ Oph, with the expected null leakage for a limb-darkened star with the same diameter. We estimated the diameter of ϵ Oph as 2.94 mas and adopted 1.5 mas error bars—much larger than the true size error bars—as a simple means of enforcing a systematic noise floor based on our estimate of the instrument performance.

2.3 Data & analysis

2.3.1 Keck Nuller null leakage

Figure 2.1 presents the calibrated null leakage for 51 Oph. We combined the data from both observations, which had nearly identical projected baselines. We limited our analyses to the 8 – 11.6 μm range since noise from decreased instrument throughput rendered data beyond 11.6 μm unusable. For wavelengths less than 11.6 μm, the null leakage remains relatively flat with a $\sim$1–σ rise near 9.8 μm.

We first modeled the null leakage at two different wavelengths with uniform disk and Gaussian surface brightness profiles. We found angular diameters of 13.5 ± 0.5 mas and 18.5 ± 0.4 mas at 8 and 10 μm, respectively, for the uniform disk profile. For a Gaussian surface brightness profile, we found FWHM of 8.1 ± 0.3

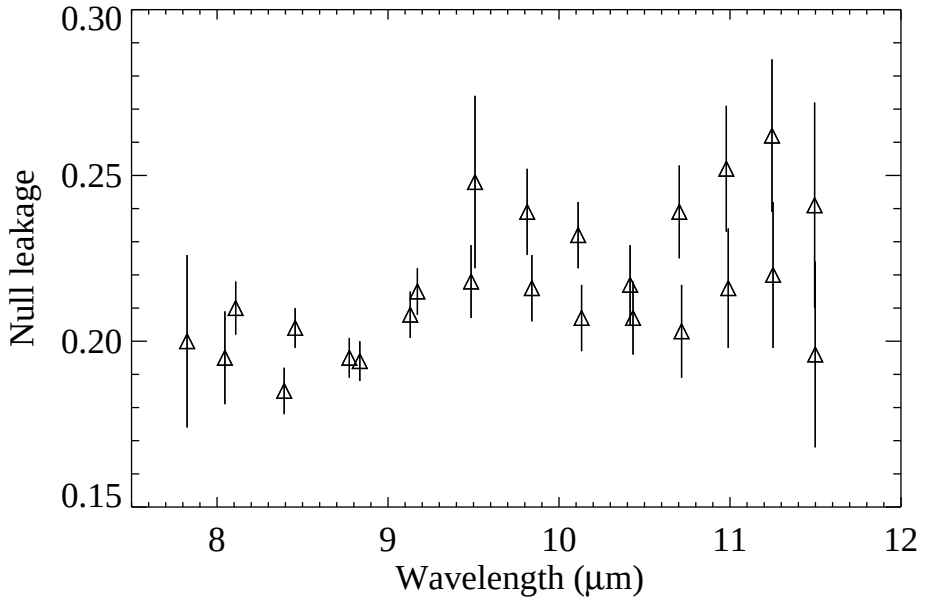

Figure 2.1: Keck Nuller null leakage measurements for 51 Oph.

mas and 11.3 ± 0.2 mas at 8 and 10 μm, respectively. At a distance of 131 pc, 10 mas corresponds to a transverse distance of 1.3 AU, suggesting that the disk is either truncated at a close circumstellar distance, or the axis of rotation of the near edge-on disk is oriented within a few tens of degrees of the projected Keck baseline.

To better understand the geometry of the 51 Oph system, we examined our Keck Nuller observations together with the observations of 51 Oph made with VLTI-MIDI and *Spitzer*. Figure 2.2 shows a collection of three independent data sets from observations of 51 Oph: the *Spitzer* IRS spectrum (Keller et al., 2008) in the top panel, our N-band Keck Nuller null leakage in the middle panel, and the N-band VLTI-MIDI visibility data (Leinert et al., 2004) in the bottom panel.

2.3.2 MIDI visibility

The VLTI-MIDI visibility was obtained on 15 June 2003 with a projected baseline of 101.2 m at a position angle of 23° (Leinert et al., 2004). Figure 2.3 shows how incorporating this data set improves the (u, v) coverage of our analysis. Although the VLTI-MIDI baseline was oriented within 25° of the Keck baseline, modeled uniform disk and Gaussian surface-brightness profile sizes are approximately 35% smaller for VLTI-MIDI measurements than for Keck Nuller measurements. When we modeled the VLTI-MIDI measurements using a uniform surface-brightness disk, we found best-fit angular diameters of 8.5 ± 1.4 mas at 8 μm and 12.4 ± 1.1 mas at 10 μm, consistent with Leinert et al. (2004). For a Gaussian model, we found a FWHM of 5.0 ± 0.9 mas at 8 μm and a FWHM of 7.7 ± 0.6 mas at 10 μm.

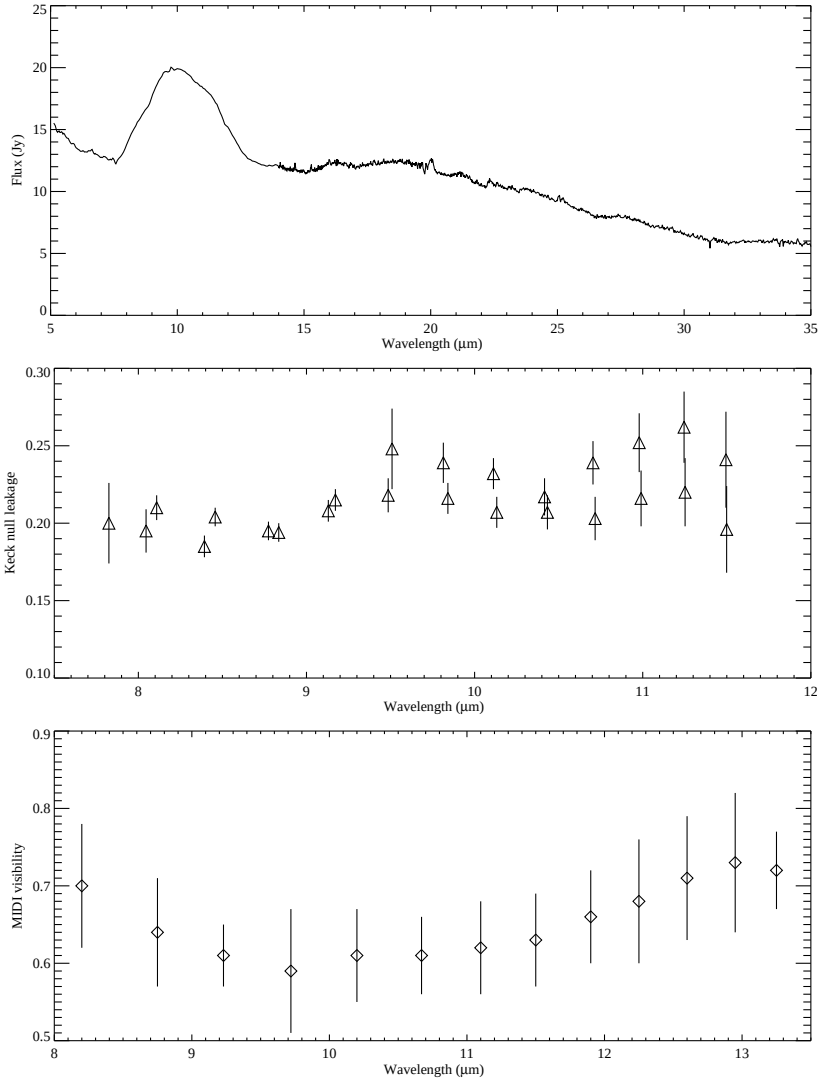

Figure 2.2: Three data sets included in our analysis. *Top:* the observed *Spitzer* IRS spectrum. *Middle:* the observed Keck Nuller null leakage (triangles) shown with error bars. *Bottom:* the observed VLTI-MIDI visibility (diamonds) shown with error bars.

The middle panel in Figure 2.2 shows a 1–σ rise at 9.8 μm in the Keck null leakage. The VLTI-MIDI visibility contains a 1–σ dip at 9.7 μm. These features mirror the 10 μm silicate emission feature shown in the *Spitzer* IRS spectrum (Section 2.3.3) and suggest that 51 Oph is more extended near 10 μm.

2.3.3 Spitzer IRS spectrum

The mid-infrared spectrum, shown in the top panel of Figure 2.2, was obtained on 22 March 2004 using the Infrared Spectrograph (IRS) on the *Spitzer Space Telescope* (Keller et al., 2008). *Spitzer* observed 51 Oph in staring mode from 5 to 36 μm using the Short-Low (SL) module from 5 to 14 μm, the Short-High (SH) module from 10 to 19 μm, and the Long-High (LH) module from 19 to 36 μm. SL has a resolving power of R= 60–128, while SH and LH have R$\sim$600. 51 Oph was observed using three slit positions stepped across the nominal position of the source. The spectral extraction and calibration methods are described in Keller et al. (2008). Figure 2.2 shows that the spectrum exhibits a pronounced 10 μm silicate feature and a small 18 μm silicate feature.

Emission from polycyclic aromatic hydrocarbon (PAH) molecules contributes to the mid-IR spectra of many Herbig Ae/Be stars. We considered the possibility that this emission could contribute to our data on 51 Oph. Keller et al. (2008) included 51 Oph in a study that looked for correlations between disk structure and mid-IR PAH emission from intermediate-mass young stars. They found no measurable emission from PAH features in the 6–13 μm range in the mid-IR spectrum of

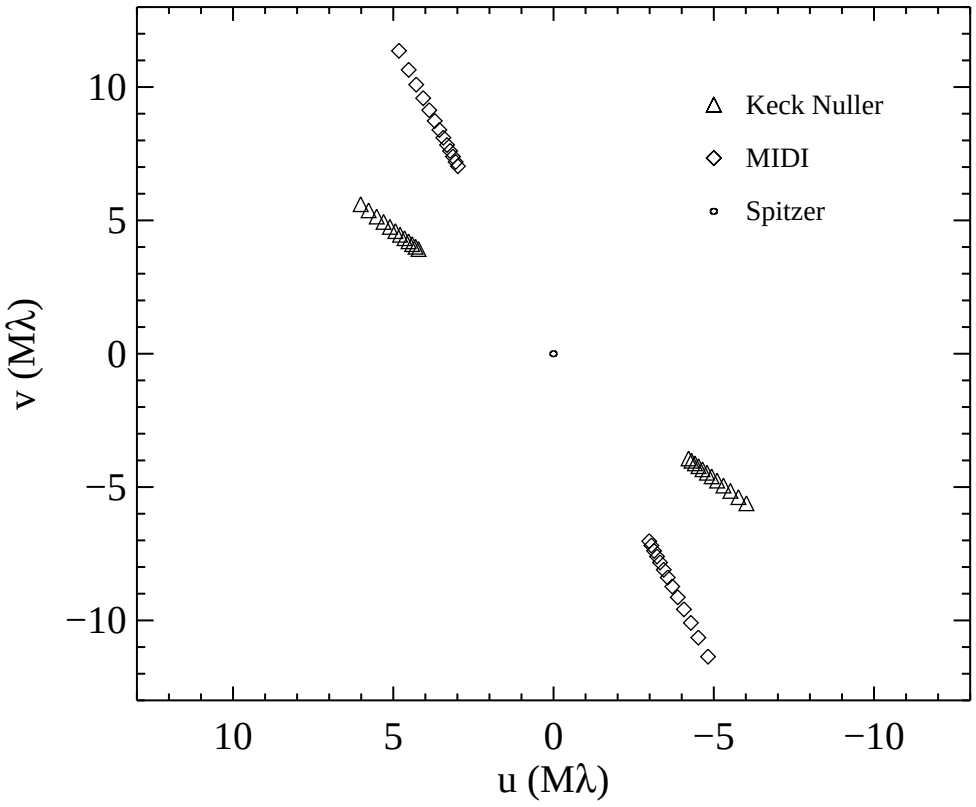

Figure 2.3: (u, v) coverage of the observations discussed in this paper. The outer boundary of the *Spitzer* (u, v) coverage is shown as a circle, corresponding to the *Spitzer* mirror diameter at 8 microns.

51 Oph.

2.4 Modeling the 51 Oph disk

There have been several previous attempts to model the 51 Oph IR excess. Waters et al. (1988) fit IRAS photometric data with an optically thin, spherically symmetric dust shell model and found a best fit model with a dust density proportional to $r^{-1.3}$ and dust temperatures ranging from $\sim$ 100 K to $\sim$ 1000 K. Fajardo-Acosta et al. (1993) modeled photometric data from the Infrared Telescope Facility (IRTF) and estimated that the IR excess could be attributed to astronomical silicates smaller than 5 μm, ranging in temperature from 400 K to 1000 K. Leinert et al. (2004) compared an optically-thick Herbig Ae disk model with a puffed inner rim (Dullemond et al., 2001) to the 51 Oph MIDI visibility in the 8 – 14 μm range and IR ISO spectra and found that such a model fit poorly.

We developed new models for 51 Oph to incorporate the new data from *Spitzer* and the Keck nuller. We do not model the detailed mineralogy of the 51 Oph disk and do not intend for our models to explain all of the observed spectral features to high numerical accuracy. We focus on the 3-D dust density distribution and disk models that qualitatively describe all three data sets.

We adopted the following fitting procedure to simultaneously fit all three data sets:

1. Model the disk contribution to the *Spitzer* IRS spectrum to obtain the radial distribution of grains, the grain size, and the surface density for each model

component.

2. Using the parameters determined by the best-fit *Spitzer* IRS spectrum, fit the interferometric data using 3-D models of the dust distribution to obtain the scale height of each component and the disk position angle.

To model the disk contribution to the *Spitzer* IRS spectrum, we first calculated the IR excess. We modeled the stellar contribution to the *Spitzer* IRS spectrum as an ideal blackbody with an effective temperature of 10,000 K and a luminosity of 260 $L_\odot$ at 131 pc (van den Ancker et al., 2001). The stellar continuum contributes on the order of a few percent in the N-band, so any uncertainties in the stellar luminosity or temperature are too small to significantly impact the interferometric or spectral responses of our models. For example, a 10% increase in the assumed luminosity would only raise the stellar fractional flux contribution from $\sim 5\%$ to $\sim 7\%$ at 10 μm.

The 51 Oph IR excess exhibits a sharp increase in flux at wavelengths shorter than 7.5 μm that resembles a continuum source. However, this feature may not be continuum. Using ISO-SWS spectra with a spectral resolution of $\sim .02\%$, van den Ancker et al. (2001) showed this region exhibits emission features from hot circumstellar gas species, including H_2O, NO, CO, and CO_2. In light of this contamination, we chose to ignore the spectrum at wavelengths shorter than 7.5 μm while we were fitting our dust cloud models. We also resampled the *Spitzer* IRS data to a resolution of $\Delta\lambda/\lambda = 0.0185$ to conserve computer time.

To create 3-D optically-thin disk models, we used the ZODIPIC software pack-

age (Moran et al., 2004). This software (available online at http://asd.gsfc.nasa.gov/Marc.Kuchner/home.html) synthesizes images of optically thin dust disks based on the Kelsall et al. (1998) empirical model of the solar zodiacal cloud as observed by COBE DIRBE. The grain size and inner and outer radius of each modeled disk component were determined by the best fit to the *Spitzer* IRS spectrum.

2.4.1 Single-component optically-thin models

For our first models we used a single component of silicate dust grains of size s distributed from an inner radius, $r_{\rm inner}$, to an outer radius, $r_{\rm outer}$. We assumed a density distribution similar to that of the zodiacal cloud (Kelsall et al., 1998); the surface density $\Sigma(r) \propto r^{-0.34}$. We numerically calculated the temperature as a function of circumstellar distance based on the stellar spectrum and dust optical constants, accounting for the heating of small grains above the local blackbody temperature. We examined 100 grain sizes, s, ranging from 0.05 – 2.5 μm and used the astronomical silicate emissivities from Draine & Lee (1984). We used a non-linear least squares fitting routine to determine the best fit inner and outer disk radii for each grain size.

The best-fit single-component disk model, shown in Figure 2.4, consists of 1.0 μm grains distributed from the grain sublimation radius ($\approx$ 0.65 AU) to 189 AU. As you might imagine, this single component does a poor job of fitting the complexities of the *Spitzer* IRS spectrum. We found that a single-component model cannot adequately reproduce the relative 10 μm to 18 μm flux ratio, the width of

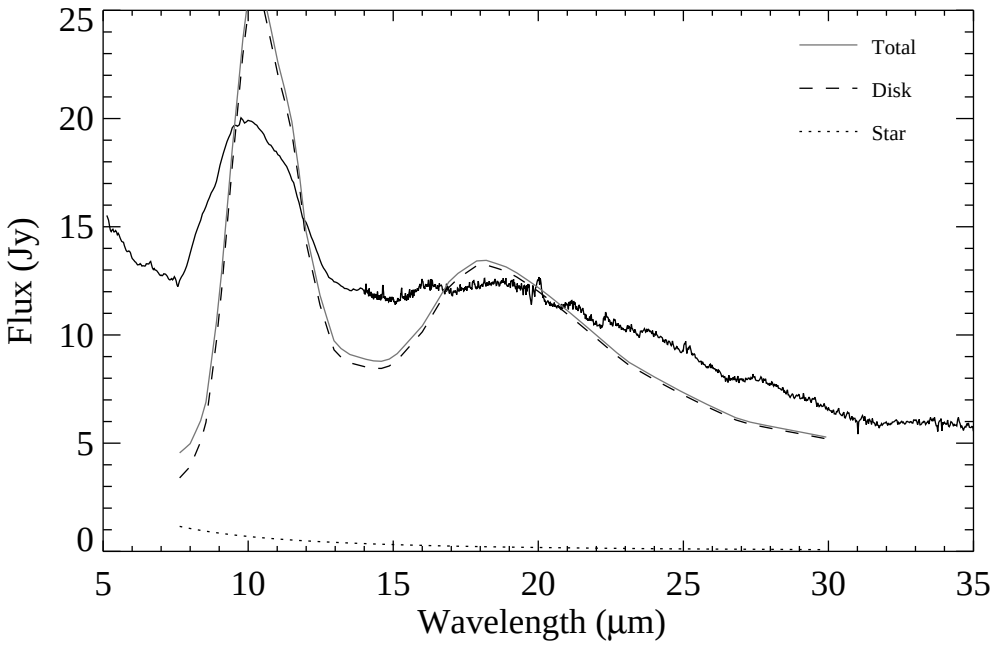

Figure 2.4: Best fit single-component disk model to the *Spitzer* spectrum (solid black line). The best fit features 1 μm grains, distributed from 0.65 AU to 189 AU.

the 10 μm feature, and the flux in the 13 – 15 μm range.

2.4.2 Two-component optically-thin models

An additional disk component, either of different composition, grain size, or location, appears necessary to fit the *Spitzer* IRS spectrum. Therefore, we examined several models consisting of two optically-thin components: an outer disk of small dust grains ($\lesssim 5$ μm), which contribute the 10 μm silicate emission feature, and an inner disk of large blackbody grains. Our optically-thin models are defined by 10

adjustable parameters: inner and outer radii of the outer disk ($r_{\rm in,1}$, $r_{\rm out,1}$), inner and outer radii of the inner disk ($r_{\rm in,2}$, $r_{\rm out,2}$), grain size in the outer disk (s_1), scale height of the outer disk (h_1/r), scale height of the inner disk (h_2/r), surface density scaling factor of the outer disk (Σ_1), surface density scaling factor of the inner disk (Σ_2), and a common position angle for both disk components (PA). We assumed a fixed inner disk grain size, $s_2 = 100$ μm, a fixed dust density radial distribution, $n(r) \propto r^{-1.34}$ (see below), and a fixed disk inclination, $i = 90°$.

First, we fit our two-component model to our resampled *Spitzer* IRS spectrum. We examined 20 values for s_1 ranging from 0.1 – 3 μm and explored a wide range of inner and outer disk radii ranging from the dust sublimation radius for silicate grains (0.65 AU for 1 μm grains) to thousands of AU. Generally, for the models that best fit the spectrum, the large grain component stretched from $\sim$ 0.6 AU out to $\sim$ 5 AU and the small grain component stretched from a few AU out to $\sim$ 1000 AU.

The top panel in Figure 2.5 shows the total flux of the best fit model, which we refer to as "Model A." It also shows the contribution of each component of this model to the total flux. As shown in Figure 2.5, Model A qualitatively reproduces all of the major features in the *Spitzer* IRS spectrum.

We used the parameters that best fit the *Spitzer* IRS spectrum to create 3-D optically-thin disk models using ZODIPIC. We examined 237 values of disk scale heights ranging from $h/r = 0.007$ to $h/r = 0.2$ for both the inner and outer disks. We examined position angles from 0 to 180° in 1° increments. We calculated the Keck Nuller null leakage and VLTI-MIDI visibility for all combinations of disk scale heights and position angle to find the best-fit Model A, the parameters for which

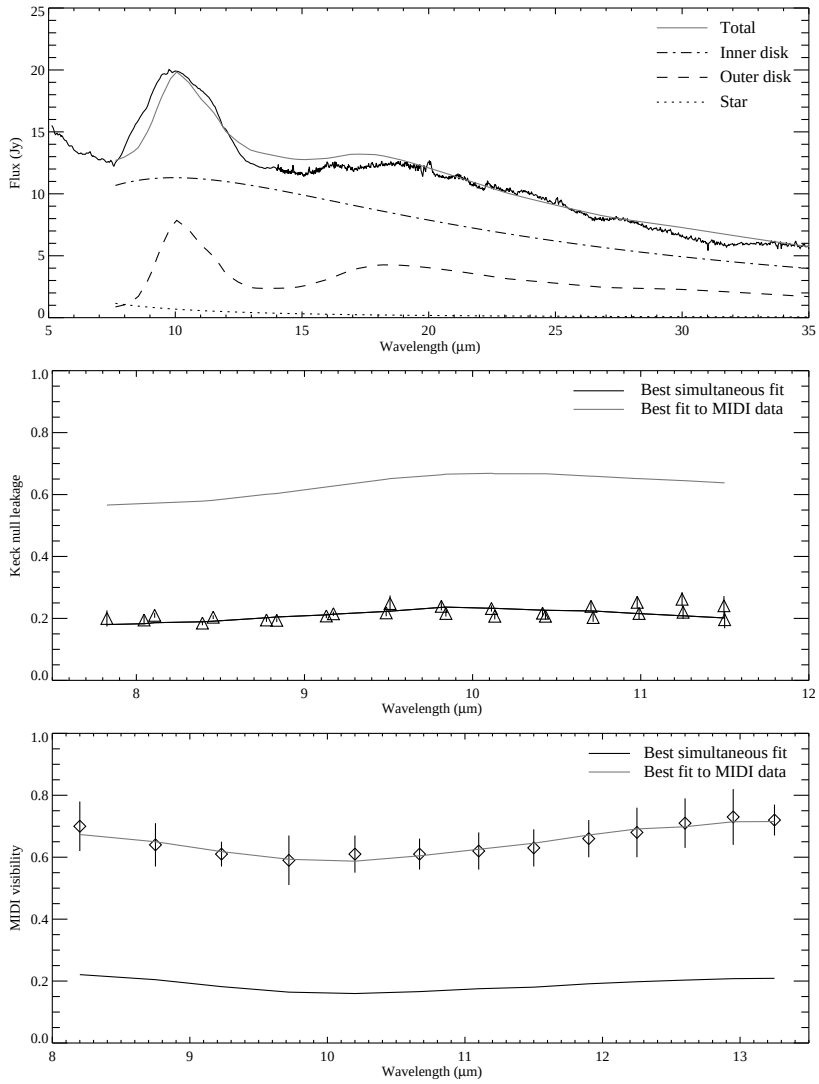

Figure 2.5: Model A, the best fit to the three data sets using a 2-component optically thin disk model. *Top:* best-fit modeled spectrum. *Middle:* best-fit modeled null leakage when simultaneously fitting both Keck and VLTI-MIDI data sets (black line) and when fitting the VLTI-MIDI data set alone (gray line). *Bottom:* modeled VLTI-MIDI visibilities. Table 2.2 lists the best-fit parameters of Model A. The best fit to the VLTI-MIDI data alone gives a disk PA= 117° and outer and inner disk scale heights of $h_1/r \approx 0.038$ and $h_2/r \approx 0.024$, respectively.

Table 2.2: Best-fit optically-thin model parameters with 99.73% joint confidence estimates

Parameter	Model A	Model B
s_1 (μm)	$0.1^{+0.05}_{-0.05}$	$0.1^{\dagger}$
$r_{\rm in,1}$ (AU)	$2.44^{+0.07}_{-0.0}$	$7.1^{+0.3}_{-0.3}$
$r_{\rm out,1}$ (AU)	1200^{+2300}_{-600}	1200^{+2300}_{-600}
h_1/r	$0.03^{\dagger}$	$0.19^{\ddagger}$
Σ_1 (zodis)	$1.15^{+0.08}_{-0.08}\times10^5$	$2.05^{+0.06}_{-0.06}\times10^5$
s_2 (μm)	100^{a}	100^{a}
$r_{\rm in,2}$ (AU)	$0.716^{+0.006}_{-0.005}$	0.54^{b}
$r_{\rm out,2}$ (AU)	$14.5^{+0.4}_{-0.2}$	4.0^{b}
h_2/r	$0.050^{+0.004}_{-0.003}$	$0.04^{\dagger}$
Σ_2 (zodis)	$2.49^{+0.07}_{-0.07}\times10^5$	$4.3^{+0.1}_{-0.1}\times10^5$
PA ($^\circ$)	$131^{+0.15}_{-0.05}$	$122^{+0.5}_{-0.15}$

[a]Fixed parameter in both models
[b]Fixed value in Model B
[c]One "zodi" refers to a face-on optical depth of 10^{-7} at 1 AU
[†]Upper limit
[‡]Lower limit

are listed in Table 2.2. To calculate the Keck Nuller null leakage and VLTI-MIDI visibility, we used a software suite that we designed to model these instruments (see Barry et al., 2008). We confirmed that the results from our software suite agreed with the Visibility Modeling Tool, a tool developed by the NExSci for simulating KIN data (http://nexsciweb.ipac.caltech.edu/vmt/vmtWeb/).

The interferometric responses of Model A are shown in the middle and bottom panels of Figure 2.5. The best simultaneous fit to the Keck Nuller null leakage and VLTI-MIDI visibility, shown in black, illustrates that Model A does not satisfactorily reproduce both interferometric responses simultaneously. The Keck null leakage is well-fit, but the VLTI-MIDI visibility is underestimated by a factor of ~ 3, indicating

that this dust disk model is too extended along the VLTI-MIDI baseline. Figure 2.5 also shows in gray the response corresponding to the best fit to the MIDI data alone, which does not produce a satisfactory Keck null leakage.

Figure 2.6 explains the source of the problem. The top panel in Figure 2.6 shows the Keck and VLTI-MIDI 10 μm responses for Model A as a function of disk position angle. The VLTI-MIDI response of Model A (gray diamonds) crosses the measured VLTI-MIDI value (gray line) at a position angle of $\sim 115°$. The Keck Nuller response of Model A (black triangles) crosses the measured Keck null leakage (black line) at a position angle of $\sim 131°$. To fit both data sets, the 10 μm responses for the model would need to intersect their respective measured values at a single position angle. The top panel in this figure clearly shows that this does not happen; there is no single position angle for the model that works for both the Keck and VLTI-MIDI data.

Figure 2.6 also reveals how a new model can remedy the problem. The position angles of the maximum in the VLTI-MIDI response and the minimum in the Keck response are fixed and correspond to the alignment of the instrument's projected baseline with the disk axis of rotation. So to improve our fit to the interferometric data, we must change the model so that we broaden the widths of the maximum in the VLTI-MIDI response and minimum in the Keck response; we must make the model more azimuthally symmetric.

We attempted to accomplish this improvement manually by increasing the scale height of the disk models. However, making this change alone reduces the maximum VLTI-MIDI visibility of the model until it no longer reaches the measured

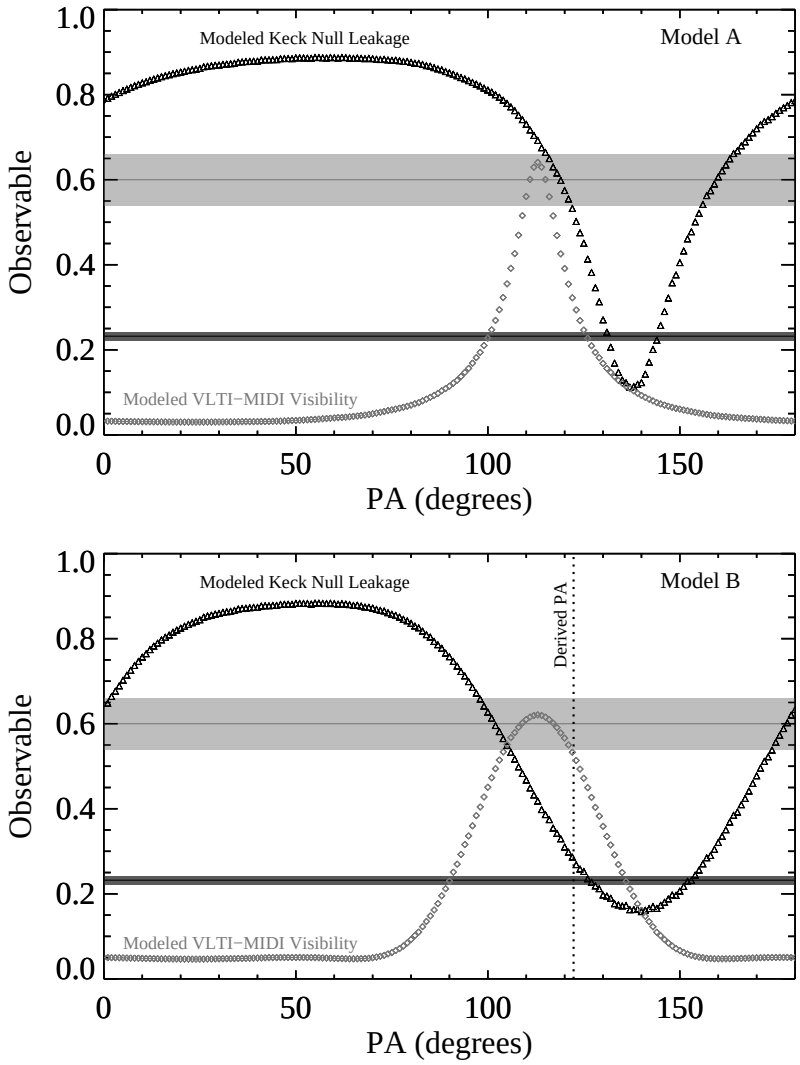

Figure 2.6: *Top:* Modeled 10 μm interferometric response as a function of PA for the Keck Nuller (black triangles) and VLTI-MIDI (gray diamonds) for Model A. The solid black and gray lines show the 10 μm measurements for Keck and MIDI, respectively, along with shaded regions representing their measurement uncertainties. The modeled Keck and MIDI responses do not cross their measured values together at any one PA. *Bottom:* Modeled 10 μm response for Model B. The modeled responses cross the corresponding measured values at $\approx 122°$.

value. So to compensate, we also reduced the outer radius of the inner disk; we forced the inner and outer radii of the inner disk to 0.54 AU and 4 AU, respectively, and re-ran the fitting procedure. We call the resulting best-fit "Model B." The bottom panel in Figure 2.6 shows that the 10 μm interferometric responses of Model B cross the measured values approximately simultaneously at a single position angle of 122°, indicated with a dotted vertical line in the figure.

Although Model B does not fit the *Spitzer* IRS spectrum as well as Model A, it still qualitatively reproduces the spectrum's major features, as shown in the top panel in Figure 2.7. The middle and bottom panels of Figure 2.7 show that these changes significantly improve the fit to the interferometric data; Model B is consistent with both the Keck null leakage and VLTI-MIDI visibility.

Figure 2.8 shows a simulated image of our Model B circumstellar disk at 10 μm with 1 mas pixel resolution. The inner disk of large dust grains, truncated at 30.5 mas (4 AU), is the brightest feature of our model. The outer disk extends from 53 mas to ∼9200 mas, beyond the range of the figure.

Our models imply that 51 Oph hosts a cloud of small grains located at hundreds to thousands of AU from the star, supporting the models of Waters et al. (1988) and Lecavelier des Etangs et al. (1997). Our models are consistent with limits placed on the disk flux by previous non-detections. An HST ACS non-detection at V-band using the 1.8″ occulting spot limits the disk surface brightness to 3×10^{-3} Jy arcsec^{-2} between 2″ and 4″ (Doering et al., 2007) and a Keck 18 μm nondetection places an upper limit on the surface brightness at 1″ of 2% of the peak flux (Jayawardhana et al., 2001). Our Model A, which extends to $\sim$ 1200 AU, has a

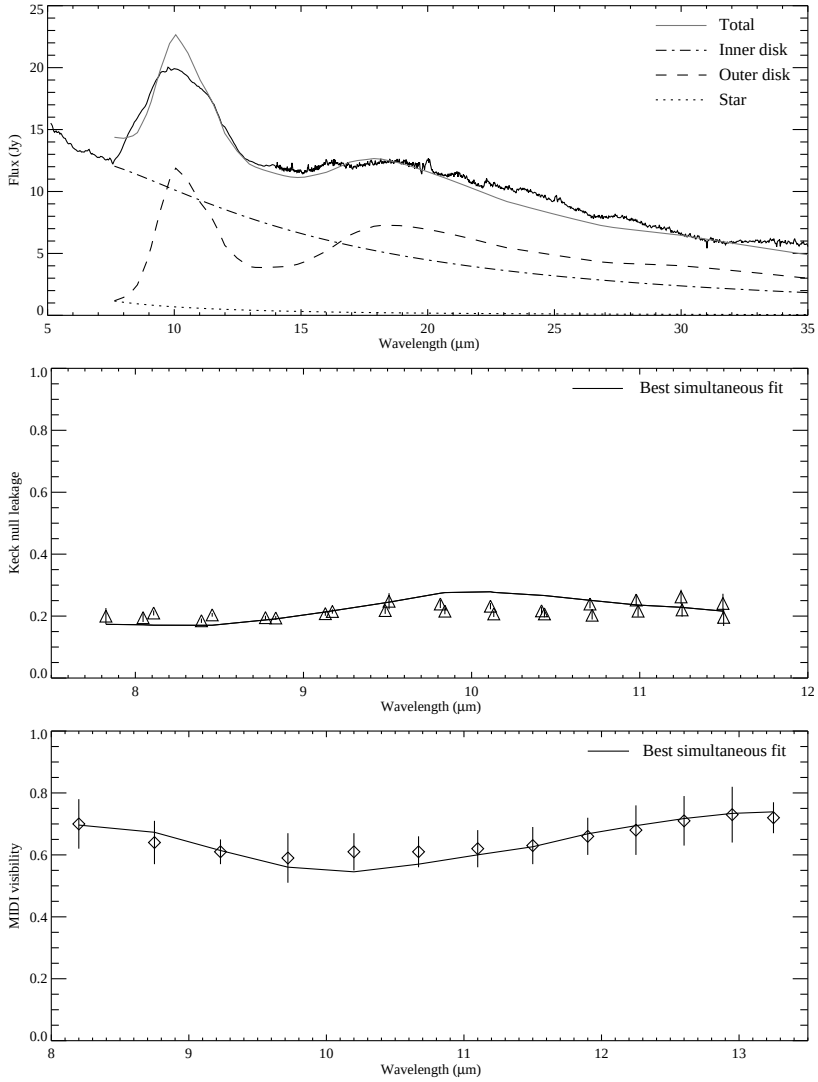

Figure 2.7: Model B, the best fit to the three data sets using a 2-component optically thin disk model where the inner and outer radii of the inner disk are forced to 0.54 AU and 4 AU, respectively. The best-fit parameters of Model B are listed in Table 2.2.

mean V-band surface brightness of 8×10^{-5} Jy arcsec^{-2} between 2″ and 4" and a mean 18 μm surface brightness at 1″ of 0.2% of the peak flux, well within the ACS and Keck non-detection limits. Our Model B has a mean V-band surface brightness of 1.4×10^{-4} Jy arcsec^{-2} between 2″ and 4″ and a mean 18 μm surface brightness at 1″ of 0.4% of the peak flux, also well within the non-detection limits. We also compared a 10.6 μm model image against recent diffraction-limited Keck imaging using segment tilting interferometry on a single telescope (Monnier et al., 2009). Our model appears consistent with these data, which indicate the observed characteristic emission scale to be <30 mas, with >95% of emission arising within an aperture of 1.5".

Tatulli et al. (2008) observed the inner portions of the 51 Oph disk at K-band with VLTI-AMBER. Tatulli et al. (2008) found the best fit to the 2.2 micron continuum visibility measurements using a narrow ring 0.24 AU in radius, well within the dust sublimation radius, and noted that this continuum may result from hot dust interior to the sublimation radius which is shielded from stellar radiation or from free-free emission from an inner gas disk (Muzerolle et al., 2004). We calculated the K-band visibility of our Model B for the three baseline orientations used by Tatulli et al. (2008) and checked these calculations with the Visibility Modeling Tool provided by NExScI. We calculated K-band visibilities of 0.99, 0.74, and 0.74 for baselines of 55 m at 34°, 82 m at 91°, and 121 m at 69°, respectively. These values are close to the measured visibilities of 1.0±0.1, 0.8±0.05, and 0.8±0.03; the latter two modeled visibilities fall just below the lower limit of the measured visibilities given the reported uncertainties.

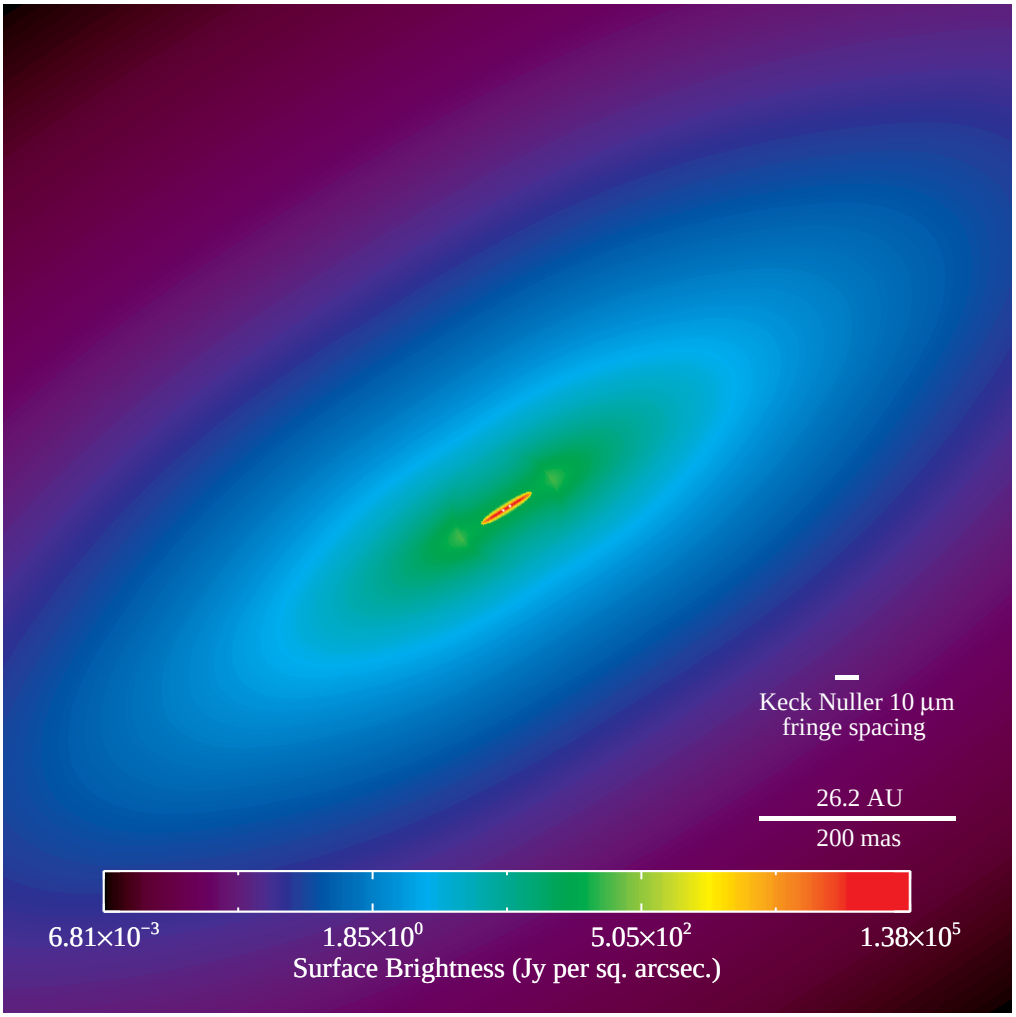

Figure 2.8: Simulated 10 μm image of Model B in units of flux per pixel, with a pixel size of 1 mas. The disk midplane is oriented at 122° East of North. The parameters of Model B are listed in Table 2.2.

Because the Keck Nuller and VLTI-MIDI do not resolve these extreme inner portions of the disk, the K-band observations may probe a different structure than what the N-band observations probe. Tatulli et al. (2008) use photometric data to estimate that the excess continuum contributes 25% of the total flux at 2.2 microns. By estimating the stellar flux at 2.2 microns and modeling the continuum flux source as a blackbody at 1500 K (dust at the sublimation temperature), we calculate that the continuum source's contribution at N-band would be no larger than 1.9 Jy. This contribution is a factor of $\sim$5 less than the flux from the blackbody component of our best fit two-component optically thin disk models. This disparity suggests that an additional blackbody component is necessary beyond what Tatulli et al. (2008) model. Additionally, our Model A and Model B blackbody components contribute only 1.4 Jy and 3.4 Jy of flux at 2.2 microns, respectively, compared to the 3.6 Jy of excess continuum flux calculated by Tatulli et al. (2008). Perhaps Model A plus a continuum source interior to the dust sublimation radius (shielded hot dust or free-free emission from a gas disk), could explain all of the interferometric and spectral data sets.

2.4.3 Two-layer models

Motivated by the Chiang & Goldreich (1997) and Dullemond et al. (2001) circumstellar disk models, we explored an alternative edge-on disk geometry consisting of a blackbody midplane layer sandwiched between two identical optically-thin surface layers of small dust grains. The surface layers are thin; they have a very small

scale height and are unresolved in the direction perpendicular to the midplane. Our models were completely defined by 6 parameters: the disk position angle, the temperature and scale height of the middle layer, and the temperature, grain size, and line density of the surface layers. We investigated 100 middle-layer and 100 surface-layer temperatures ranging from 300 – 1300 K, and 6 surface layer dust sizes from 0.1 – 1.0 μm. We used the surface-layer temperature, which represents the temperature of the surface layer at the outer truncation radius of the disk, to calculate the outer radius of the disk. Because our disk is edge-on, we ignore any contribution by a hot inner wall. We note that Leinert et al. (2004) fit the VLTI-MIDI data with a Dullemond et al. (2001) flared disk model which included a hot inner wall and found this model to fit poorly.

We first derived the total emitting area of each component, and therefore the line density of the surface layers and scale height of the middle layer, by fitting the flux of the two disk components to the *Spitzer* observations. For the 500 best fits to the *Spitzer* IRS spectrum, we calculated the Keck null leakage and VLTI-MIDI visibility as a function of position angle in 1° increments. Figure 2.9 shows the single best fit to the three data sets. The best fit two-layer model qualitatively reproduces the major features of the *Spitzer* IRS spectrum, shown in the top panel of Figure 2.9, although it underestimates the flux near 8 μm and overestimates the flux from 10–18 μm. The lower two panels of Figure 2.9 shows this model can reproduce the mean Keck null leakage, but cannot simultaneously reproduce the VLTI-MIDI visibility. The interferometric data seems to rule out this disk geometry.

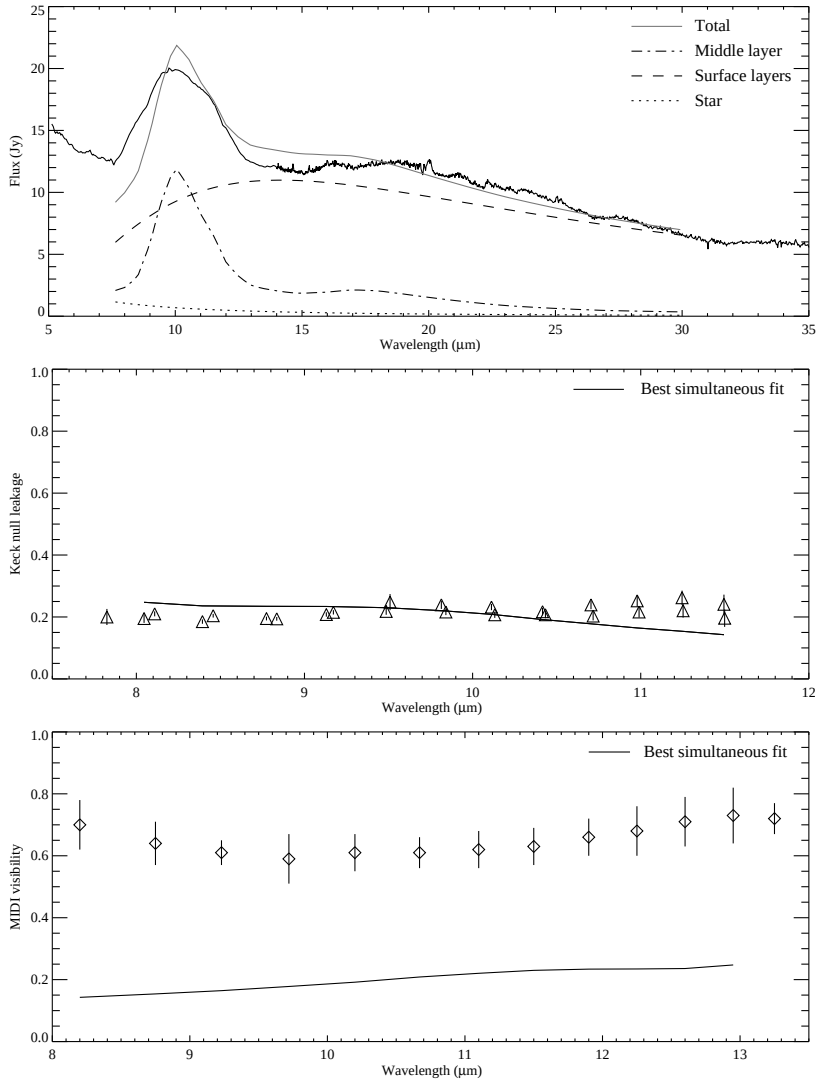

Figure 2.9: Best simultaneous fit to the three data sets using a two-layer optically-thick disk model. The best fit model is a disk oriented with a position angle of 38° and truncated at outer radius 3.4 AU. The disk features a middle layer of 360 K blackbody grains with a disk height of 0.163 AU from the midplane, and 2 surface layers of 0.7 μm grains heated to 835 K, each with line densities of 8.2×10^{32} AU^{-1}.

2.5 Discussion & interpretation of models

Our modeling efforts have yielded an optically-thin disk model that can qualitatively reproduce our 51 Oph observations with the Keck Nuller and also the VLTI-MIDI and *Spitzer* observations of this system. This model, Model B, is composed of an inner ring of large grains distributed from their sublimation radius (~ 0.5 AU) out to ~ 4 AU, and an outer ring of small grains (< 1 μm) distributed from an inner radius of $\sim$7 AU to an outer radius of $\sim$1200 AU. We also experimented with optically-thick models, but found them unsatisfactory.

Our preferred optically-thin disk model could be interpreted as an inner "birth" disk of material producing small dust grains through collisions. Grains produced in the inner ring that are larger than the blowout size either spiral inward under Poynting-Robertson drag or are collisionally fragmented. Grains smaller than the blowout size exit the system on hyperbolic orbits in a dynamical time; the ejected grains and marginally ejected grains correspond to the outer disk component. The blowout size for blackbody dust grains in a disk without gas is given by

$$s_{\rm blowout} = \frac{3L_\star}{8\pi G M_\star c \rho_{\rm s}}, \tag{2.1}$$

where $L_\star$ and $M_\star$ are the luminosity and mass of the star, respectively, G is the gravitational constant, c is the speed of light, and $\rho_{\rm s}$ is the dust density (Burns et al., 1979). Assuming $L_\star \approx 260\,L_\odot$, $M_\star \approx 3\,M_\odot$, and $\rho_{\rm s} = 2$ gm cm^{-3}, the blowout size for 51 Oph is approximately 50 μm, consistent with our preferred model. A similar pattern, a central population of large grains and an outer ring of small grains, has been seen in observations of the debris disks around β Pictoris (Augereau et al.,

2001), Vega (Su et al., 2005), and AU Microscopii (Strubbe & Chiang, 2006).

2.5.1 Gas in the 51 Oph disk

Of course the disk around 51 Oph is not gas free (e.g. Lecavelier des Etangs et al., 1997; van den Ancker et al., 2001; Berthoud et al., 2007), so our scenario of an inner birth ring and outer disk of ejected grains requires that the gas disk is sparse enough to allow the small grains to be ejected from the system. Here we estimate the maximum tolerable gas density for which small grains are unbound in the 51 Oph system.

The stopping time of a dust grain undergoing Epstein drag forces is given by

$$t_{\rm stop} \sim \frac{s\rho_{\rm s}}{\rho_{\rm g} c_{\rm sound}}, \tag{2.2}$$

where $\rho_{\rm g}$ is the gas density and $c_{\rm sound}$ is the sound speed (see, e.g. Weidenschilling & Cuzzi, 1993). The dynamical timescale is given by

$$t_{\rm dynamic} \sim \left(\frac{a^3}{GM_\star}\right)^{1/2}, \tag{2.3}$$

where a is the semi-major axis of the grain. For the dust grains to be significantly affected by gas drag, $t_{\rm stop} < t_{\rm dynamic}$. Substituting $c_{\rm sound} = (kT_{\rm g}/m_{\rm g})^{1/2}$, where k is the Boltzmann constant, $T_{\rm g}$ is the gas temperature, and $m_{\rm g}$ is the mass of an H_2 molecule, we find that entraining a 1 μm grain in the gas would require

$$\left(\frac{n_{\rm g}}{1\ {\rm cm}^{-3}}\right) \lesssim 10^{10}\ T_{\rm g}^{-1/2} \left(\frac{a}{1\ {\rm AU}}\right)^{-3/2}. \tag{2.4}$$

Assuming a gas temperature of 1400 K at a circumstellar distance of 5 AU, near the vicinity of the inner disk, the gas density required to stop a 1 μm grain is $\sim 10^7$

cm^{-3}. We conclude that if the disk around 51 Oph is comprised of an inner birth ring and an outer disk of ejected grains, then the gas density in the 51 Oph disk must be less than ∼100 times the gas density of β Pic (Brandeker et al., 2004) at a circumstellar distance of ∼5 AU.

2.5.2 A possible warp in the disk

The outer disk in Model B has a scale height at least ∼4 times larger than the scale height of the inner disk. So the small grains at high orbital inclinations in the outer disk seem unlikely to have originated from the thin inner disk in our simple model. Such small grains cannot easily be perturbed to high-inclination orbits by hidden planets either, because of their short lifetimes compared to secular time scales.

The difference in scale heights between the two components of our model suggests to us that 51 Oph may have an unobserved sub-disk of larger bodies on inclined orbits in the inner regions of the disk. The limited (u, v) coverage and resolution of the Keck and VLTI-MIDI observations could easily keep such a sub-disk hidden from our observations. This sub-disk might be analogous to the X-pattern, or "warp" imaged by Golimowski et al. (2006) in the β Pictoris disk. The large bodies in this sub-disk could launch the small grains onto inclined orbits, just as Augereau et al. (2001) suggested occurs in the β Pictoris disk.

2.5.3 Limitations of the model & sources of confusion

Here we discuss two possibilities that might complicate our interpretation of the mid-IR interferometry of 51 Oph: a) the disk composition or structure is more complex than can be represented by our models, or b) the disk has changed during the four year interval between VLTI-MIDI and Keck observations.

The chemical composition of the 51 Oph dust disk is not well-known. Our models assumed astronomical silicates only, and ignored the possibility of a more complex composition. A detailed model of the 51 Oph disk composition, along the lines of Reach et al. (2009) for example, which we leave for future work, would help to further refine our models.

The disk geometry could also be more complex than our models can capture. As previously discussed, there are a number of observations which suggest that an inner circumstellar disk is near edge-on in the 51 Oph system. Our optically-thin models of the dust disk assume an outer disk which is coplanar, but the 51 Oph disk inclination may be more complex. Some debris disks show warps or sub-disks at different inclinations (e.g. Golimowski et al., 2006). It is possible that our assumption of coplanar disks does not allow Model A, which best fits the *Spitzer* IRS spectrum, to simultaneously fit the VLTI-MIDI visibility and Keck null leakage.

The 51 Oph disk geometry may also have changed between observations. The blowout time for small grains originating from a belt of material at 1 AU is on the order of a single dynamical time (only a few years). So the outer disk could evolve significantly within the four years between Keck and VLTI-MIDI observations via

a recent collisional event (e.g. van den Ancker et al., 2001). Additionally, 51 Oph's inner disk could feature complex resonant structures, such as clumps or rings due to the presence of planets (e.g. Stark & Kuchner, 2008), which rotate in and out of view on a dynamical timescale.

A comparison of the *Spitzer* IRS spectrum shown in Figure 2.5 and the ISO spectrum published in van den Ancker et al. (2001) reveals that the 51 Oph disk may have changed significantly in the 8 years between spectral observations. The silicate emission feature in the *Spitzer* IRS spectrum peaks at 10 μm, whereas the ISO spectrum peaks at 10.5 to 11 μm. The slope of the right side of the silicate emission feature is also noticeably steeper in the *Spitzer* IRS spectrum; estimated slopes of the right side of the 10 μm silicate emission feature are ~ -1.4 Jy μm^{-1} and ~ -2.9 Jy μm^{-1} for ISO and *Spitzer* observations, respectively. These differences indicate that the 51 Oph disk may have had larger grains at the time of the ISO observations. Finally, the flux longward of 20 μm in the ISO spectrum is ~ 3 Jy less than the Spitzer IRS spectrum, possibly because there were fewer cold grains at the time of the ISO observations.

2.6 Summary

We observed the 51 Oph disk at N-band using the Keck interferometer operating in nulling mode. We combined the observed Keck null leakage with VLTI-MIDI visibility data and the *Spitzer* IRS spectrum and simultaneously modeled all three data sets. We experimented with a variety of optically-thin dust cloud models and

also an edge-on optically-thick disk model. The *Spitzer* IRS spectrum ruled out the single-component optically-thin model, while the interferometric data ruled out our optically-thick model.

Our preferred model consists of two separate populations of large and small grains. The three data sets are best simultaneously fit by our Model B (Table 2.2). This model, shown in Figure 2.7, contains a disk of larger grains that extends from the grain sublimation radius out to ~ 4 AU and a disk of 0.1 μm grains that extends from ~ 7 AU to ~ 1200 AU.

This model may be consistent with an inner "birth" disk of continually colliding parent bodies. The large grains ($\gtrsim 50$ μm) produced by the parent bodies make up the inner disk, while the small grains ($\lesssim 50$ μm) are blown outward and eventually ejected from the system by radiation pressure. The large scale height of the outer disk compared to the inner disk suggests that the small grains which compose the outer disk may originate from an unseen inclined sub-disk or from a population of inclined cometary bodies.

Although the 51 Oph disk seems puzzling at first, perhaps it is not so strange after all. The distribution of grain sizes in our models is not unique to the 51 Oph system, but has been observed in the β Pictoris (Augereau et al., 2001), Vega (Su et al., 2005), and AU Microscopii (Strubbe & Chiang, 2006) disks. Our models suggest that the 51 Oph disk may be another member of a class of debris disks which exhibit similar dust distributions. Our models also indicate that there may be two sources of dust at different inclinations around 51 Oph. These models, together with previous observations of variable absorption features (Grady & Silvis, 1993; Roberge et al.,

2002) which may be due to transient infalling bodies suggest that the 51 Oph dust disk may well be an example of a β Pictoris-like system.

Chapter 3

Decoding the morphologies of exozodiacal cloud structures

3.1 Introduction

A number of proposed experiments like the Terrestrial Planet Finder (TPF) aim to directly image the scattered and emitted light from extrasolar planets (Lawson & Traub, 2006). These experiments will also excel at detecting exozodiacal dust, circumstellar dust analogous to zodiacal dust in the Solar System (e.g. Agol, 2007; Beckwith, 2007). Zodiacal dust in the Solar System consists of $\sim 1 - 100$ μm dust grains released through asteroidal collisions and the outgassing of comets (e.g. Schramm et al., 1989). This dust forms the zodiacal cloud, extending from the solar corona (e.g. Mann et al., 2000) to beyond Jupiter (e.g. Krüger et al., 1999).

Our zodiacal cloud exhibits several structures interpreted as dynamical signatures of planets (Dermott et al., 1985, 1994; Reach et al., 1995). Several dusty disks around nearby main-sequence stars show similar structures (e.g. Greaves et al., 1998; Wilner et al., 2002; Kalas et al., 2005). This trend suggests that exozodiacal

clouds may be full of rings, clumps and other asymmetries caused by planets and other phenomena.

This situation raises some important questions. Will the structures in exozodiacal clouds be harmful astrophysical noise for direct imaging of extrasolar planets (Beichman, 1996; Beichman et al., 1999)? Or can the dynamical signatures of planets in these clouds help us find otherwise undetectable planets (e.g. Kuchner & Holman, 2003)?

Several studies have examined the geometry of resonant signatures of planets in debris disks (e.g. Kuchner & Holman, 2003; Reche et al., 2008). However, most simulations cannot quantitatively study the contrast in these structures: how bright they are relative to the background cloud. We need to model the contrast of the structures in exozodiacal clouds to understand their roles as astrophysical noise and as signposts of hidden planets. However, accurately simulating the contrast of these structures demands computational resources that have only recently become available (e.g. Deller & Maddison, 2005).

In this paper we examine the contrast of resonant structures induced by planets in steady-state exozodiacal clouds and the detectability of these structures via direct imaging. We simulate high-fidelity images of collisionless exozodiacal clouds containing a terrestrial-mass planet—an exo-Earth or super-Earth. By using roughly an order of magnitude more particles than most previous simulations, we overcome the Poisson noise associated with constructing histograms of the column density and populating the external mean motion resonances (MMRs) of planets. We use our simulations to estimate the minimum planet mass that can be indirectly de-

tected via observations of these structures as a function of the planet semi-major axis and dominant grain size under the assumption of circular planet orbits. Our models apply to tenuous exozodiacal clouds less than ∼10 times the optical depth of the solar zodiacal cloud, clouds for which the collision time is longer than the Poynting-Robertson (PR) time for typical grains.

Section 3.2 describes our numerical techniques. We present a synthetic catalog of resonant debris disk structures in Section 3.3. We describe our multiple-particle-size cloud models and discuss their detectability in Section 3.4. In Section 3.5, we discuss the limitations of our simulations; we summarize our conclusions in Section 3.6.

3.2 Numerical method

Dust grains in the inner Solar System are primarily released from parent bodies via collisions or outgassing. Radiation pressure ejects the smallest particles from the Solar System in a dynamical time while the larger particles slowly spiral inward due to PR drag (Robertson, 1937; Burns et al., 1979). During their spiral toward the Sun, particles may become temporarily trapped in the MMRs of planets, extending their lifetimes by a factor of a few to ten (Jackson & Zook, 1989). This trapping locally enhances the particle density, creating structures within the zodiacal cloud, which have been described as circumsolar rings, bands, and clumps (e.g. Kelsall et al., 1998).

To model these types of structures in exozodiacal clouds we numerically in-

tegrated the equation of motion of dust particles. The equation of motion for a perfectly absorbing particle orbiting a star of mass $M_\star$ is given to first order in v/c by Robertson (1937):

$$\frac{d^2\mathbf{r}}{dt^2} = -\frac{GM_\star}{r^2}(1-\beta)\hat{\mathbf{r}} - \frac{(1+\mathrm{sw})\beta}{c}\frac{GM_\star}{r^2}[\dot{r}\hat{\mathbf{r}} + \mathbf{v}], \tag{3.1}$$

where $\mathbf{r}$ and $\mathbf{v}$ are the heliocentric position and velocity of the particle and sw is the ratio of solar wind drag to PR drag. We assume a value for sw of 0.35 (Gustafson, 1994). For perfectly absorbing spherical particles in the vicinity of the Sun, Equation 1.3 gives $\beta \approx 0.57/\rho s$, where ρ is the mass density of the particle in g cm^{-3} and s is the radius in μm.

3.2.1 A customized hybrid symplectic integrator

We implemented a customized hybrid symplectic integrator to perform our numerical integrations. Chambers (1999), hereby referred to as C99, introduced hybrid symplectic integration as a method for dealing with close encounters in an efficient n-body code. Symplectic integrators rely on splitting the Hamiltonian into two easily integrable portions—a dominant term, H_D, and a smaller perturbative term, H_P. However, in the n-body problem, H_P may exceed H_D during close encounters. Hybrid symplectic integrators overcome this problem by effectively switching from a symplectic integrator to an alternate integrator (e.g. Bulirsch-Stoer).

The hybrid method reduces the perturbative term of the Hamiltonian, H_P, by a factor $K(r_{ij})$, where r_{ij} is the distance between the two bodies in question, to ensure

that the perturbative term remains relatively small. The integrator includes the remaining portion of the perturbative term, $\sum_{i,j} H_{\mathrm{P},ij}[1 - K(r_{ij})]$, in the dominant term which is then integrated using a method of choice. The "changeover function," $K(r_{ij})$, is a smooth function that varies from 0 for $r_{ij} \lesssim r_{\mathrm{crit}}$ to unity for $r_{ij} \gtrsim r_{\mathrm{crit}}$.

Using a hybrid integrator requires choosing a changeover function and a value for r_{crit}. We use the same changeover function as C99. We assign a different value of $r_{\mathrm{crit},i}$ to each body, calculated as the larger of $3R_{\mathrm{H},i}$ and $v_i\,\Delta t$, where $R_{\mathrm{H},i}$ and v_i are the Hill radius and velocity of the i^{th} body, respectively, and Δt is the time step of the integrator. We then calculate the critical distance for a pair of bodies as $r_{\mathrm{crit},ij} = r_{\mathrm{crit},i} + r_{\mathrm{crit},j}$.

Our integrator also incorporates the effects of radiation pressure, PR drag, and solar wind drag. We implement radiation pressure as a correction to the effective stellar mass (cf. Eq. 3.1) and treat the drag effects as an additional term in H_{P}, in much the same way as Moro-Martín & Malhotra (2002), hereby referred to as MMM02. We also use democratic heliocentric (DH) coordinates, composed of the barycentric momenta and heliocentric positions, because of their relative ease of implementation. This choice introduces an additional perturbative term to the Hamiltonian due to the motion of the star with respect to the barycenter (Duncan et al., 1998).

3.2.2 Comparison of integrator with previous results

We checked our integrator using a variety of standard tests. We checked the energy and Jacobi constant conservation with the drag terms turned off and examined the evolution of dust particles' orbital elements under our implementation of drag effects. We also compared our hybrid integrator to a Bulirsch-Stoer integrator by examining the path of an individual test particle during a close encounter and by examining the statistics of a cloud of particles in a collisionless disk containing a planet.

We tested energy conservation in our integration code by integrating the orbits of the four outer planets and the Sun for 3×10^5 years using a time step of 0.15 years. The energy error was bounded with a mean value of $\Delta E/E \approx 3 \times 10^{-9}$.

Duncan et al. (1998), which we will refer to as DLL98, tested the relative conservation of energy in their symplectic integrator as a function of planet perihelion distance. We replicated their tests using our code. Figure 3.1 shows the relative energy error in an integration of the orbit of Jupiter for 3×10^5 years using a time step of 0.15 years. We initially placed Jupiter at aphelion. Figure 3.1 also shows the results of integrating the orbits of Jupiter and Saturn under the same conditions. With the DH method, the perturbative solar term increases as the perihelion distance of the planet decreases, causing the fractional energy error to increase similarly. The fractional energy errors shown in Figure 3.1 agree with those obtained by DLL98.

We checked the conservation of the Jacobi constant by integrating particles

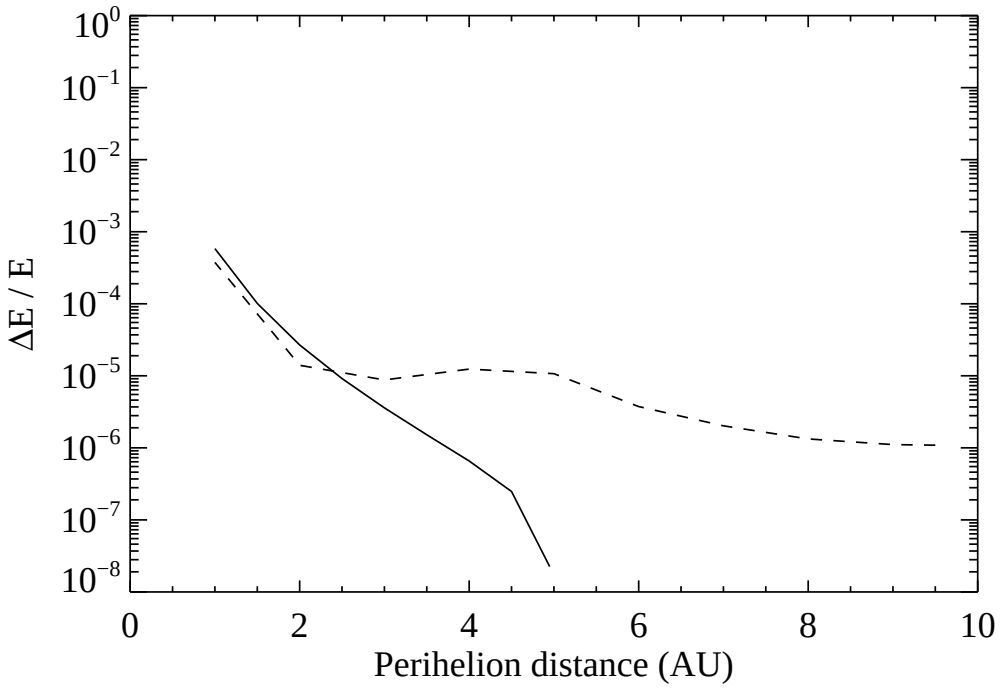

Figure 3.1: Maximum fractional error in energy during a 3,000-year integration as a function of perihelion distance for two scenarios: a two-body system of the Sun & Jupiter (solid line) and a three-body system of the Sun, Jupiter & Saturn (dashed line). For the two-body system, Jupiter's perihelion distance is plotted. For the three-body system, Saturn's perihelion distance was altered while Jupiter's remained fixed. The inclinations and eccentricities of both planets remained fixed. cf. DLL98 Fig. 4.3.

in the Sun-Neptune system. We found results consistent with those of MMM02. Particles that did not undergo close encounters conserved the Jacobi constant at the level of $\sim 10^{-8}$ to 10^{-7}.

To test our implementation of PR drag, we replicated a test performed by MMM02. We integrated the orbit of a particle with $\beta = 0.2$ and sw $= 0.35$ in the presence of the Sun. Figure 3.2 shows the semi-major axis and eccentricity as functions of time. These results match the results of MMM02 and agree with the analytic solution (Wyatt & Whipple, 1950).

We tested the performance of our hybrid scheme by integrating the orbit of comet P/Oterma in a close encounter with Jupiter, which has been done previously by Michel & Valsecchi (1996) and C99. The initial conditions for both bodies can be found in Table 3 of Michel & Valsecchi (1996). Figure 3.3 shows the path of comet P/Oterma for several values of integration time step Δt as seen in the frame co-rotating with Jupiter, which is located at the origin. These results are similar to those obtained by C99. Our code shows a minor improvement over the other codes, most noticeable in the $\Delta t = 100$ days case, that is likely only due to differences in the calculation of the changeover distance. C99 explicitly sets $r_{\rm crit} = 3R_{\rm H}$ for this test; we used our prescription for $r_{\rm crit}$ as described in Section 3.2.1.

3.2.3 Test simulations of a steady-state exozodiacal cloud

We directly compared simulations of resonant structures made with our hybrid integrator to simulations made with a Bulirsch-Stoer integrator. During the inte-

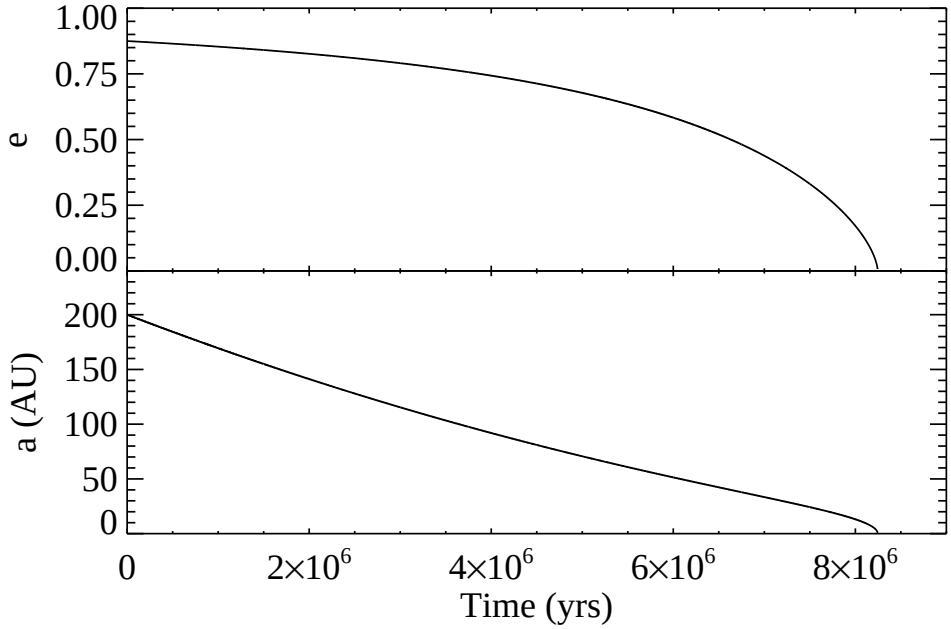

Figure 3.2: *Top:* eccentricity as a function of time for a dust particle with $\beta = 0.2$ and sw = 0.35. *Bottom:* semi-major axis as a function of time. Our results match those of MMM02 (cf. MMM02, Fig. 1) and agree with the analytic solution (Wyatt & Whipple, 1950).

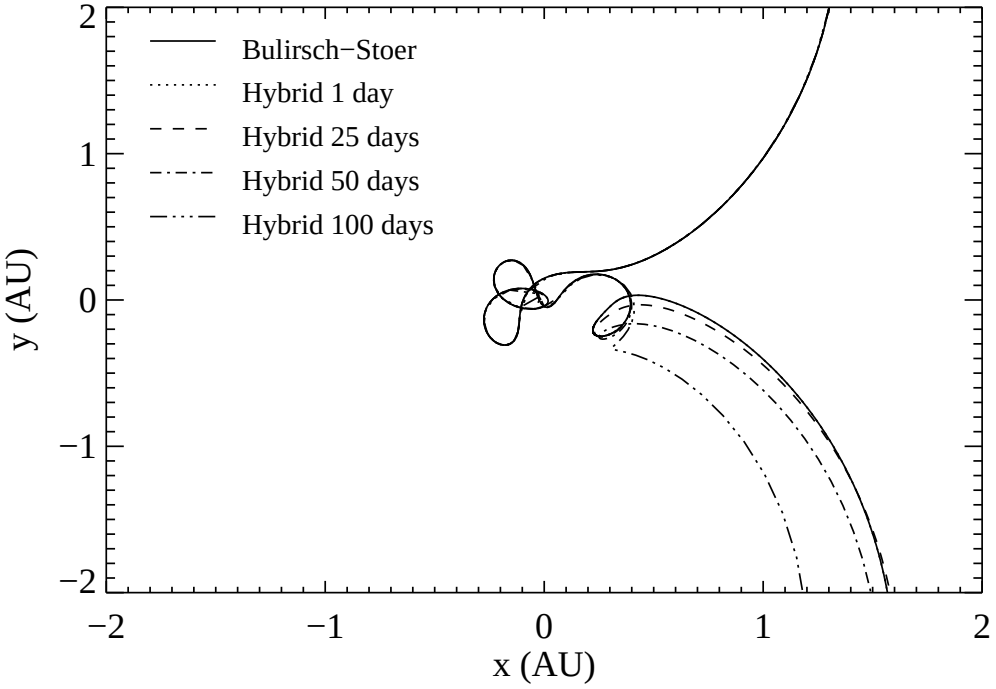

Figure 3.3: The integrated trajectory of comet P/Oterma during a close encounter with Jupiter as viewed in the frame centered on and rotating with Jupiter with the Sun on the negative x-axis. Shown are the results of a Bulirsch-Stoer integrator and our hybrid symplectic integrator for four values of integration time step. The hybrid symplectic results overlap the Bulirsch-Stoer results for a timestep of 1 day (cf. C99, Fig. 4).

grations we recorded the coordinates of each particle in a 2-D histogram at regular intervals. This histogram models the surface density distribution in a steady-state cloud. Since we only modeled planets on circular orbits, we simply recorded the coordinates in the frame co-rotating with the planet. This technique has been widely used by dust cloud modelers (Dermott et al., 1994; Liou & Zook, 1999; Moro-Martín & Malhotra, 2002; Wilner et al., 2002; Deller & Maddison, 2005).

Figure 3.4 shows two histograms, one for each integrator, for simulations of 1,000 particles each in the presence of the Sun/Earth system. We used a histogram bin width of 0.0175 AU. For these simulations we chose $\beta = 0.02$ and initially released the particles with semi-major axis, $a_{\rm dust}$, distributed uniformly between 3 and 5 AU, eccentricity, e, uniformly distributed from 0.0 to 0.1, and inclination, i, uniformly distributed between 0° and 6°. We used a symplectic time step of 0.02 years and recorded the particle locations every 250 years.

Except for a small number of pixels, the middle panel of the figure (simulation using the hybrid integrator) looks qualitatively very similar to the left-most panel (simulation using the Bulirsch-Stoer integrator). The right panel of Figure 3.4 shows the difference of these two images divided by the $\sqrt{n}$ Poisson noise expected for each pixel where n is the number of particles in the pixel. This figure demonstrates that the differences between the two models are nearly consistent with the Poisson noise of the histograms. The two integrators resulted in histograms with minor structural differences, but the hybrid symplectic integrator runs a few times faster.

Besides pixel-to-pixel Poisson noise in the histogram, this method is also sensitive to noise in the population of MMRs. MMM02 showed that the population of

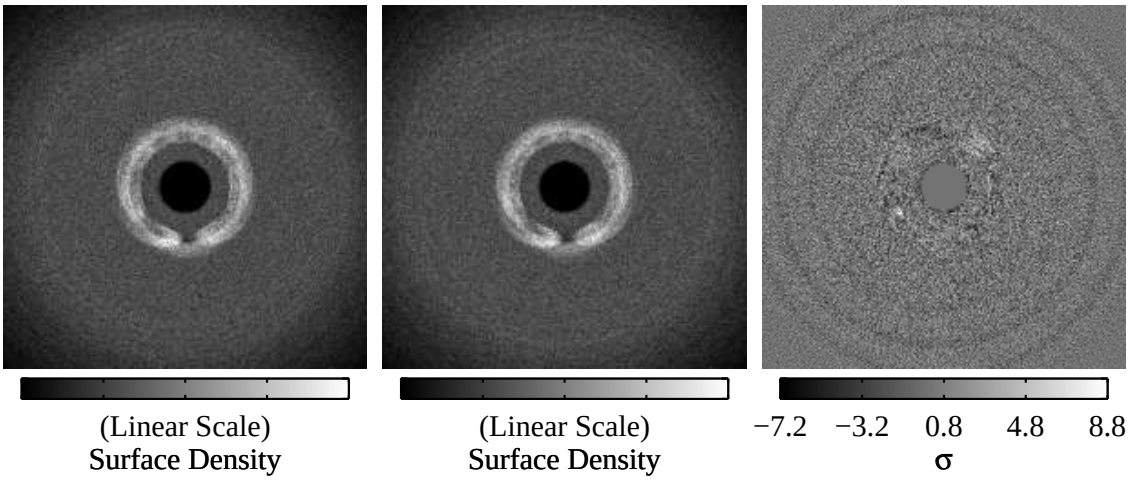

Figure 3.4: Comparison of our hybrid symplectic integrator with a Bulirsch-Stoer integrator. *Left:* surface density histogram for 1,000 particles in the Sun-Earth system using a Bulirsch-Stoer integrator. *Middle:* surface density histrogram for the same initial conditions using our hybrid symplectic integrator. *Right:* Bulirsch-Stoer histogram minus the hybrid symplectic histogram (image is in units of σ, the $\sqrt{n}$ Poisson noise associated with the histograms). Except in a handful of pixels, the difference is roughly consistent with Poisson noise.

the dominant resonances varied by a factor of ~ 3 among sets of 100-particle simulations of Kuiper Belt dust interacting with Neptune. This noise probably causes the differences between the two simulations shown in Figure 3.4 beyond those attributable to pixel-to-pixel Poisson noise. Although simulations of 100 particles may acquaint us with the generic geometry of debris disk structures, we cannot use them to predict ring contrasts; to model the contrast in a resonant cloud feature we must include enough particles to accurately populate the MMRs.

We solved this problem by using more particles. We used the 420-processor Thunderhead cluster at NASA Goddard Space Flight Center to perform simulations of 5,000 particles each. Figure 3.5 shows the population of MMRs for three independent 5,000-particle simulations of the Sun and four outer planets using the same initial conditions as MMM02. Simulating 5,000 particles reduced the difference between MMR populations for the three simulations to less than 7% for the dominant 2:1 and 3:2 MMRs, allowing us to synthesize high-fidelity images and quantitatively study the resonant ring structures.

3.3 Simulations & results

3.3.1 Cataloging debris disk structure

To explore the range of different types of structures formed by terrestrial-mass planets, we performed 120 simulations of dust interacting with single planets on circular orbits. The simulations used 5,000 particles each and covered six values of planet mass, $M_{\rm p}$ (0.1, 0.25, 0.5, 1.0, 2.0, and 5.0 $M_{\oplus}$), four values of planet

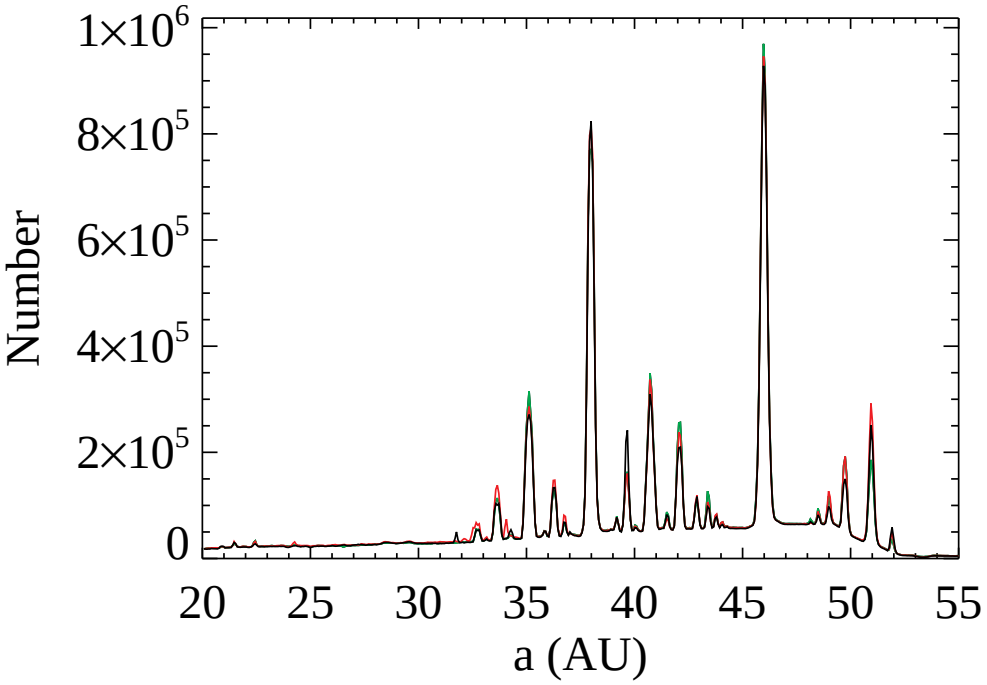

Figure 3.5: Population of Neptune's MMRs for three independent simulations of 5,000 particles each (shown in green, red, and black). Populations of the 2:1 and 3:2 resonances differ among the three simulations by 6.4% and 4.3%, respectively (c.f. Moro-Martín & Malhotra, 2002, Fig. 5).

semi-major axis, $a_{\rm p}$ (1, 3, 6, and 10 AU), and five values of β (0.0023, 0.0073, 0.023, 0.073, and 0.23) corresponding to spherical silicate particles ranging in radius from $\sim 1 - 120\mu$m. We released the particles on orbits with semi-major axes uniformly distributed between 3.5 and 4.5 times the semi-major axis of the planet's orbit—well outside of the strongest MMRs. We used initial eccentricities uniformly distributed between 0 and 0.2, initial inclinations uniformly distributed between 0 and 20°, and the longitude of the ascending node, Ω, and the argument of pericenter, ω, uniformly distributed between 0 and 2π. We considered planet semi-major axes of 1 to 10 AU because typical designs for TPF can detect an exozodiacal cloud with 10 times the optical depth of the solar zodiacal cloud over roughly that range of circumstellar radii (Levine et al., 2006).

We chose these initial conditions to model only dynamically-cold dust, i.e. $e_{\rm dust} \lesssim 0.2$ and $i_{\rm dust} \lesssim 20°$, since this component of a dust cloud is the dominant contributor to resonant ring structure. We neglect dynamically hot dust with the idea that it can always be added in later as a smooth background (Moran et al., 2004). The asteroid belt probably produces much of the Solar System's dynamically cold dust, while comets are thought to contribute a more dynamically hot cloud component (e.g. Liou et al., 1995; Ipatov et al., 2008). We treat only steady-state dust clouds, assuming dust is continually replenished, and ignore transient collisional events.

Figure 3.6 shows some examples of the histograms from our simulations, which reveal a wide range of trapping behavior. Some histograms show no azimuthal or radial structure, while others show high contrast rings. All of the patterns are Type

I structures as identified by Kuchner & Holman (2003).

Several general trends emerged. The ring contrast increased with increasing planet mass. Reducing β also enhanced trapping, as did increasing the planet's semi-major axis.

These last two trends can be explained by comparing the libration time of a given MMR to the PR time. The PR time scales as $a_{\rm dust}^2/\beta$, while the libration time for a given resonance scales as $a_{\rm dust}^{3/2}$, where $a_{\rm dust}$ is the semi-major axis of a dust grain's orbit. The ratio of these quantities yields $\sqrt{a_{\rm dust}}/\beta$, a parameter that measures the degree to which resonant trapping is adiabatic (e.g. Henrard, 1982); the trapping becomes more adiabatic and more efficient at greater distances from the star, and for larger particles. We discuss this phenomenon further in Section 3.3.3 below.

In addition to following these trends, all of the simulated ring structures, like those shown in Figure 3.6, share some salient features:

1. For cases in which even a modest amount of trapping occurs (azimuthally averaged contrasts $> 1.3:1$), the ring structures exhibit a sharp inner edge at $\approx 0.83 a_{\rm p}$. This feature probably appears because the eccentricities of particles trapped in exterior MMRs are typically pumped up to a limiting value before a close encounter with the planet ejects them from resonance. For a particular MMR, all particles, regardless of β, tend to approach the same limiting eccentricity and accordingly, a similar pericenter distance (Beaugé & Ferraz-Mello, 1994). The limiting eccentricities are such that the limiting

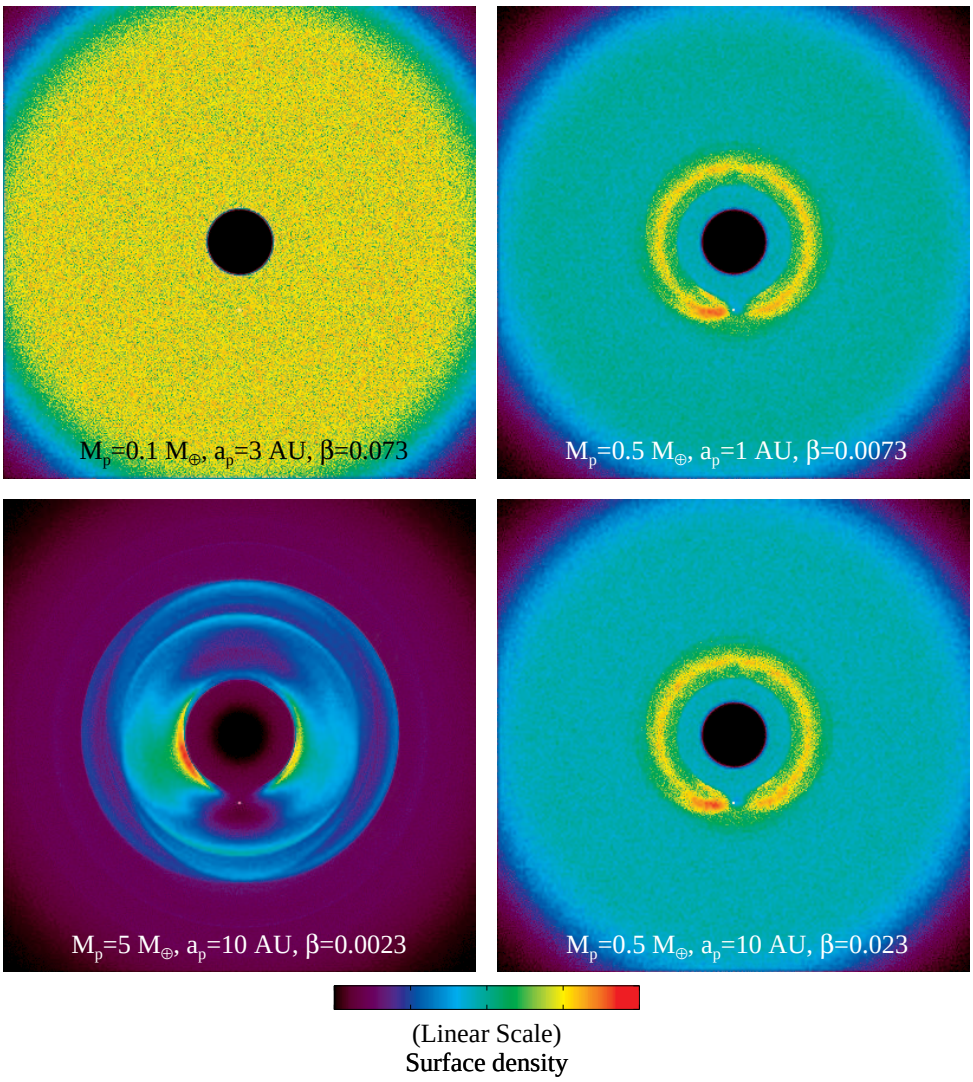

Figure 3.6: Surface density distributions for four of the 120 simulations (scale is relative). The star is located at the center of the image and the planet is marked with a white dot. The planet orbits counter-clockwise in these images. Integrations were truncated at half the planet's semi-major axis. The simulations shown on the right have different values of $a_{\rm p}$ and β, but the same value of $\sqrt{a_{\rm p}}/\beta$. Their surface density distributions are nearly identical; their difference is consistent with Poisson noise (see Section 3.3.2).

pericenter distances are nearly equal for the dominant resonances (e.g. the 2:1 and 3:2 resonances have limiting pericenter distances of $0.823a_{\rm p}$ and $0.827a_{\rm p}$, respectively), creating the ring structure's sharp inner edge.

2. A gap in the ring structure, a local minimum in the surface density, appears around the planet. If we define gap width as the FWHM of the minimum in the azimuthal surface density profile at $r = a_{\rm p}$, we find that the gap width is linearly proportional to the contrast of the ring, as shown in the left panel of Figure 3.7. A linear fit to the data shown in this figure gives $w_{\rm gap} \approx 10^{\circ} \times C_{\rm AA,IE}$ for $C_{\rm AA,IE} > 1.6$, where $w_{\rm gap}$ is the gap width in degrees and $C_{\rm AA,IE}$ is the azimuthally averaged inner-edge contrast (see Section 3.3.2).

3. The rings show a leading-trailing asymmetry. The trailing side of the ring structure is noticeably denser than the leading side, and the structure is rotationally shifted in the prograde direction causing the trailing side to be closer to the planet (Dermott et al., 1994). To examine the leading-trailing asymmetry caused by a prograde shift of the ring structure, we measured the azimuthal offset of the center of the gap described above from the planet. The right panel of Figure 3.7 shows these measured prograde shifts of our simulations. Kuchner & Holman (2003) showed for a particular first order exterior MMR,

$$\sin \phi_0 \propto \frac{\beta\,(1-\beta)}{M_{\rm p}\sqrt{a_{\rm p}}}, \tag{3.2}$$

where ϕ_0 is the prograde shift of the pericenter. Therefore, we plotted the sine of each measured prograde shift against $\beta(1-\beta)/(M_{\rm p}\sqrt{a_{\rm p}})$ in the right panel

of Figure 3.7. Our data reveal the approximate proportionality

$$\sin \phi_{\rm ring} \propto \left[\frac{\beta \left(1-\beta\right)}{M_{\rm p}\sqrt{a_{\rm p}}} \right]^{0.5}, \tag{3.3}$$

where $\phi_{\rm ring}$ is the measured prograde shift of the ring structure. While the relationship in Equation 3.2 holds for a single MMR, it does not strictly apply to a given ring structure which consists of several well-populated MMRs. The relative populations of these MMRs are also functions of $M_{\rm p}$, $a_{\rm p}$, and β. However, this situation seems to preserve a power-law relationship between $\sin \phi_{\rm ring}$ and $\beta \left(1-\beta\right) / \left(M_{\rm p}\sqrt{a_{\rm p}}\right)$, as shown in Equation 3.3.

4. The radial width of the ring increases with the contrast of the ring, ranging from a few percent of $a_{\rm p}$ to $\sim 1.6 a_{\rm p}$ in the highest contrast case. As the trapping probabilities of all the MMRs increase, MMRs farther from the planet's orbit become populated. For this reason, the outer-edge of the ring structure differs significantly among simulations. The outer-edge can be quite blurry or very well-defined, making the radial width of a ring structure difficult to quantify.

Our catalog of debris disk structures induced by terrestrial-mass planets is publicly available online at http://asd.gsfc.nasa.gov/Christopher.Stark/catalog.php. This online catalog also contains images synthesized from the density distributions in scattered light and 10 μm thermal emission assuming blackbody grains. Future studies of resonant ring structures with TPF or other experiments can use our catalog to interpret dust cloud patterns in terms of planet and dust parameters, assuming the observed image is dominated by a single grain size. We envision the

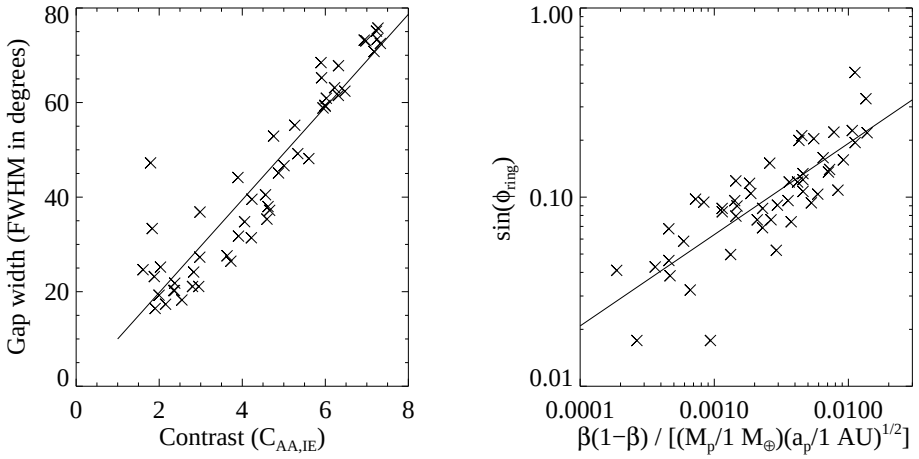

Figure 3.7: *Left:* the angular size of the "gap" in the ring structure around the location of the planet in our simulations versus the contrast of the ring structure. *Right:* the sine of the prograde shift plotted against the function $\beta(1-\beta)/(M_{\rm p}a_{\rm p}^{1/2})$. We removed all data with $C_{\rm AA,IE} < 1.6$ from these plots. Solid lines show linear fits to the data.

following process, inspired by recent papers on disks observed with the Hubble Space Telescope (e.g. Clampin et al., 2003; Kalas et al., 2005):

1. Deproject the image to remove inclination effects.

2. Remove any smooth backgrounds by a power law fit.

3. Estimate the dominant grain size in the resonant ring using infrared photometry or other methods.

4. Compare the image of the disk to the online catalog to constrain the planet's mass and location.

3.3.2 Ring contrast

We considered three different metrics for describing the ring contrast in our simulations:

C_{Max}: The surface density of the ring at its densest point divided by the surface density of the background cloud

$C_{\mathrm{AA,Max}}$: The maximum value of the azimuthally averaged surface density divided by the surface density of the background cloud

$C_{\mathrm{AA,IE}}$: The azimuthally averaged surface density at the inner edge of the ring divided by the surface density of the background cloud

We calculated the above contrast metrics for all 120 simulations. We measured the surface density of the background cloud at a circumstellar distance $r \approx 0.8 a_{\mathrm{p}}$. The surface density of the background cloud was nearly constant inside and outside

of the ring, but did exhibit a small local minimum near $r \approx 0.8a_{\rm p}$ in a few cases.

To calculate $C_{\rm Max}$, we must search for the densest pixel, which introduces a bias toward pixels that exhibit an extreme amount of Poisson noise. To reduce this noise we averaged the surface density over nine pixels centered on the densest point. Using $C_{\rm AA,Max}$ or $C_{\rm AA,IE}$, on the other hand, automatically averages over the effects of Poisson noise in our simulations.

Figure 3.8 shows two examples of how the contrast, $C_{\rm AA,IE}$, depends on planet mass and β. Both plots show a similar behavior with three distinct regions: a no-trapping regime (contrast $\sim$1), a transitional regime, and a saturation regime (maximum contrast). The saturation regime is of particular significance. Our results suggest that within the range of parameters investigated, for a given value of β, all contrasts converge to the same value for large planet masses independent of planet semi-major axis, i.e. the contrast becomes "saturated" and increasing the planet's semi-major axis has little effect on the contrast. The right panel in Figure 3.8 illustrates this behavior; all four contrast curves, each of which corresponds to a different planet semi-major axis, approach the same value of ~ 7 near $M_{\rm p} = 5\ M_{\oplus}$. Similarly, for a given planet mass, contrasts converge to the same value for small β independent of $a_{\rm p}$, as shown in the left panel in Figure 3.8. The morphology of the structure can vary, but the contrast of the ring structure is roughly constant in these saturation regimes.

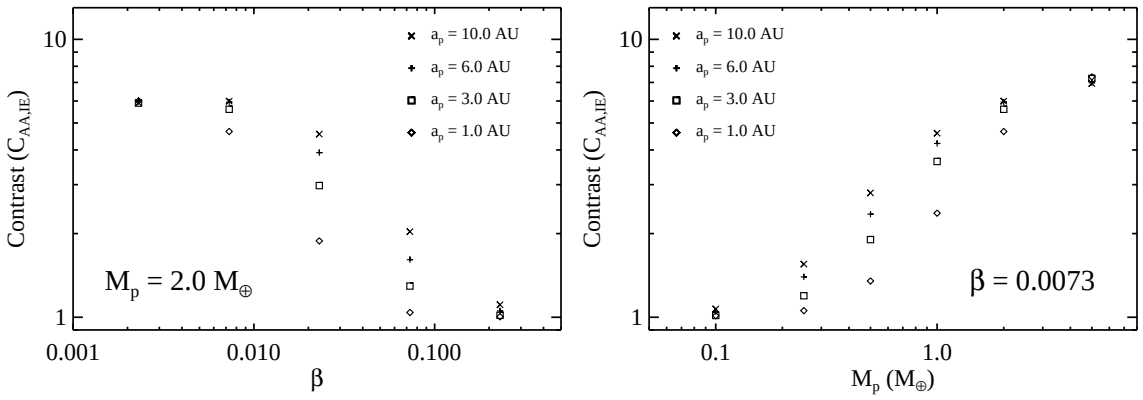

Figure 3.8: The azimuthally-averaged contrast measured at the inner edge of the ring structure (see Section 3.3.2 for definition of contrast) as a function of β (left panel) and planet mass (right panel). Both figures show a transition from a no-trapping regime to a saturation regime where contrast is independent of semi-major axis.

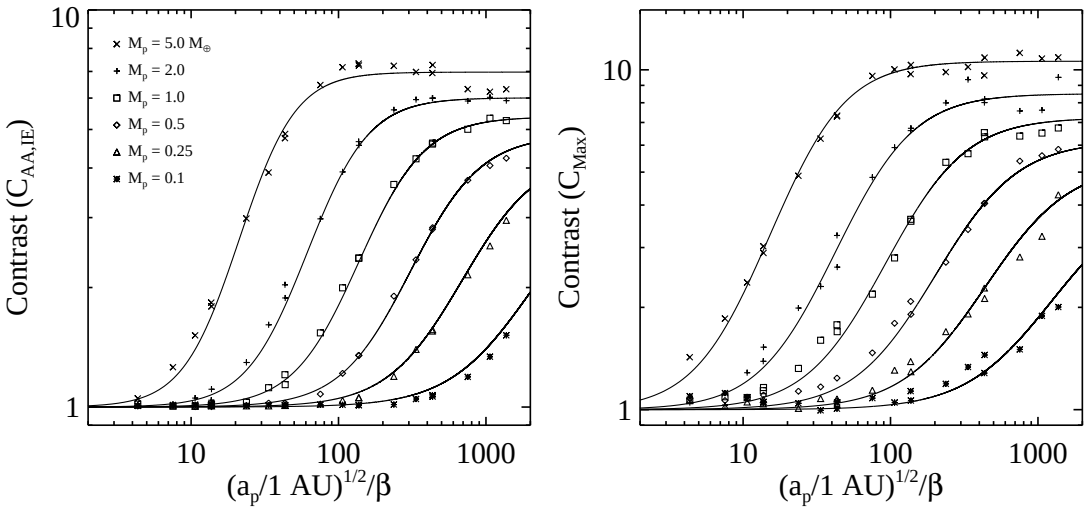

Figure 3.9: The contrast in surface density of the ring structure compared to the background cloud for all combinations of $M_{\rm p}$, $a_{\rm p}$, and β (see Section 3.3.2 for definitions of contrast). The contrast is only a function of two parameters: planet mass and $\sqrt{a_{\rm p}}/\beta$. The solid lines are fits to the data (see Equation 3.4).

3.3.3 Adiabaticity

As we mentioned above, dividing the PR time by the libration time of a given MMR yields a parameter, $\sqrt{a_{\rm p}}/\beta$, that indicates the degree to which the resonant trapping is adiabatic. We plot the contrast in our simulations as a function of this parameter in Figure 3.9. This figure demonstrates that for $M_{\rm p} \lesssim 5\ M_\oplus$ and for a given distribution of parent body orbital elements, the ring contrast is a function of only two parameters: planet mass and $\sqrt{a_{\rm p}}/\beta$.

The morphology of the resonant rings is also, to good approximation, a function of only the planet mass and $\sqrt{a_{\rm p}}/\beta$. The models shown in the two right panels of Figure 3.6 illustrate this phenomenon; for both models $\sqrt{a_{\rm p}}/\beta \approx 137$ AU$^{1/2}$. These two models have the same morphology to a level consistent with pixel-to-pixel Poisson noise. Note that for small β in Equation 3.3, the prograde shift is approximately a function of $\left(\sqrt{a_{\rm p}}/\beta\right)^{-1}$ for a given planet mass.

For large values of β and $M_{\rm p}$, the morphology and contrast of the ring structures are not simple functions of $\sqrt{a_{\rm p}}/\beta$. Simulations with large values of β, but equal values of $\sqrt{a_{\rm p}}/\beta$ (e.g. $\sqrt{1\ \rm AU}/0.073$ and $\sqrt{10\ \rm AU}/0.23$) show morphological differences, including differences in prograde shift. Our simulations with $M_{\rm p} = 5\ M_{\oplus}$ also show contrast differences among rings with equal values of $\sqrt{a_{\rm p}}/\beta$.

Wyatt (2003) investigated resonant trapping in MMRs for a system of planetesimals exterior to an outward migrating planet on a circular orbit. Wyatt (2003) plotted the trapping probability for a single MMR in his model as a function of migration rate and planet mass and found it could be well approximated by a function of the form $P = [1 + (\dot{a}_{\rm p}/p_1)^{p_2}]^{-1}$, where $\dot{a}_{\rm p}$ is the migration rate and the parameters p_1 and p_2 are power laws in planet mass. Our trapping scenario assumes dust migrating inward toward the planet, but the concept is similar. Since contrast is closely related to trapping probability, we decided to fit the data shown in Figure 3.9 with a function of the form

$$C = 1 + p_1 \left(1 + \left(\frac{p_2}{\sqrt{a_{\rm p}}/\beta}\right)^{p_3}\right)^{-1}, \tag{3.4}$$

inspired by Wyatt (2003). Each of the three parameters, p_i, is a power law in planet

mass of the form $p_i = p_{i,1} M_{\rm p}^{p_{i,2}}$. We fit all 120 contrast measurements with this six-parameter function for each of the three contrast metrics. The best fits, two of which are shown in Figure 3.9, are listed in table 3.1.

Equation 3.4, combined with the above values, summarizes our results for all combinations of planet mass, planet semi-major axis and β we simulated. Figure 3.9 shows the inner-edge contrast, $C_{\rm AA,IE}$, deviates significantly from the fits for large $M_{\rm p}$ and large $\sqrt{a_{\rm p}}/\beta$. The increased trapping efficiency for MMRs with these massive planets likely enhances the population of MMRs farther from the planet's orbit and depletes the inner MMRs that cause the sharp inner edge.

Table 3.1: Best fit parameters to Equation 3.4

	$C_{\rm AA,IE}$	$C_{\rm AA,Max}$	$C_{\rm Max}$
p_1	$4.38\,(M_{\rm p}/M_{\oplus}\,)^{0.19}$	$4.54\,(M_{\rm p}/M_{\oplus}\,)^{0.17}$	$6.23\,(M_{\rm p}/M_{\oplus}\,)^{0.27}$
p_2	$207\,(M_{\rm p}/M_{\oplus}\,)^{-1.17}$	$205\,(M_{\rm p}/M_{\oplus}\,)^{-1.17}$	$164\,(M_{\rm p}/M_{\oplus}\,)^{-1.09}$
p_3	$2.05\,(M_{\rm p}/M_{\oplus}\,)^{0.11}$	$1.63\,(M_{\rm p}/M_{\oplus}\,)^{0.19}$	$1.72\,(M_{\rm p}/M_{\oplus}\,)^{0.05}$

3.4 Multi-particle-size models

3.4.1 Composite simulations

We used our 120 simulations to produce 20 multiple-particle-size dust cloud models by forming weighted sums of the histograms assuming a Dohnanyi distribution of particle sizes (Dohnanyi, 1969). Each of these composite models effectively utilizes 25,000 particles. Exactly how we apply the ideas in Dohnanyi (1969) has

profound effects on our composite models, so we present here two different kinds of models.

First, we assembled a composite model in which the particles are initially released from their parent bodies according to a crushing law, and do not undergo any further collisional processing as they spiral inward. This scenario models a sparse disk with a belt of dust-producing material, like our own zodiacal cloud. The crushing law for asteroid material at micron sizes is unknown, so we choose the crushing law used by Dohnanyi (1969):

$$\frac{dN}{ds} \propto s^{-\alpha}, \tag{3.5}$$

where dN is the number of particles with radius s in a bin of width ds, and $\alpha = 3.4$.

We calculate the optical depth, τ, for our composite models from $\tau = \sum_i w_i A_i \sigma_i$, where w_i, A_i, and σ_i are the weighting factor, particle cross-section, and surface number density of the i^{th} single-particle simulation, respectively. We assume that the cross-section of each particle is $A_i \propto \beta^{-2}$. The crushing law in Equation 3.5 implies a weighting factor for the i^{th} histogram of $w_i = \beta_i^{\alpha-2}\Delta\beta_i$, where $\Delta\beta_i$ is the width of the β_i bin. For a constant logarithmic spacing in β, like the spacing we used in our simulations, and the Dohnanyi crushing law, $w_i = \beta_i^{2.4}$.

Larger particles have longer PR times, so in the absence of collisional processing, their density is enhanced by a factor of β^{-1} under our assumption of a steady-state cloud model. One might expect that this effect must be included in the weighting factor. However, our simulations include this effect automatically as long as we keep the frequency with which particle locations are recorded constant among

all of our simulations. We did, in fact, vary the recording frequency with the PR time, but we corrected for the differences in recording frequency before summing the histograms.

Figure 3.10 shows the optical depth of one of our 20 composite models ($M_{\rm p} = 2.0\ M_{\oplus}$, $a_{\rm p} = 6.0$ AU), together with the optical depths of single-particle-size models using only the smallest and largest particle sizes included in the composite model. Although the crushing law used by Dohnanyi (1969) favors smaller particles by number, even more than some empirical crushing laws (Durda et al., 2007), the optical depth in the composite models is dominated by the largest particles. This situation occurs because the larger particles are both longer lived ($t_{\rm PR} \propto \beta^{-1}$) and more likely to be trapped in MMRs. Hence, the upper left panel of the figure closely resembles the lower right panel.

Next, for the purpose of illustration, we ignored the initial size distribution of dust particles and forced the disk to obey a size distribution of

$$\frac{dN}{ds} \propto s^{-3.5} \tag{3.6}$$

at a radius of $\sim 3a_{\rm p}$ from the star. This scenario probably doesn't have a physical interpretation, but it illustrates an interesting phenomenon: how resonant trapping tends to sort particles by size. We enforce the size distribution at one location within the disk, but the size distribution will not follow a Dohnanyi distribution elsewhere in the disk.

The top right panel in Figure 3.10 shows the optical depth of an example of this kind of composite cloud, normalized to a Dohnanyi distribution at ~ 18 AU.

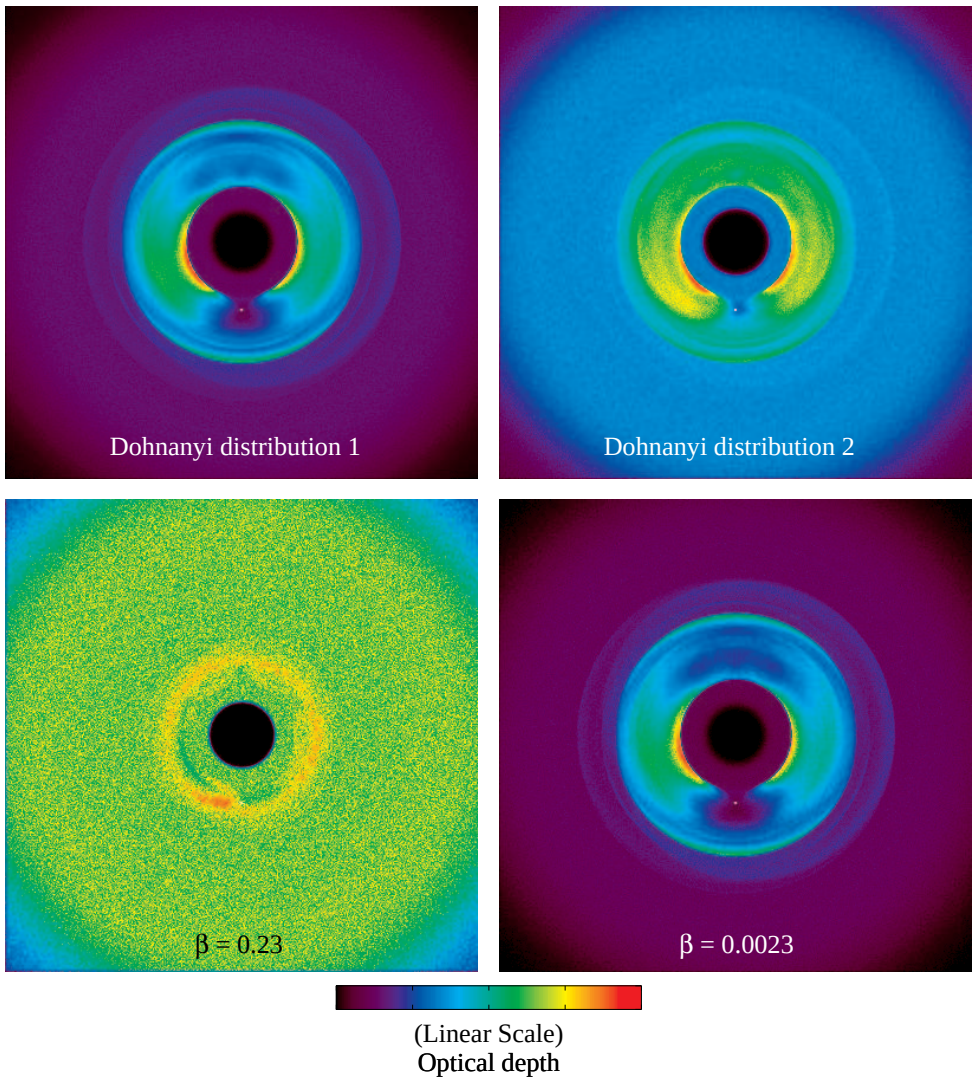

Figure 3.10: Comparison of the optical depths for a composite cloud formed by two different methods for $M_{\rm p} = 2.0\ M_{\oplus}$ and $a_{\rm p} = 6.0$ AU. *Top row:* A composite collisionless cloud formed by releasing grains with a Dohnanyi size distribution (Dohnanyi, 1969) (left) vs. forcing the background surface density to obey a Dohnanyi distribution. *Bottom:* The optical depth of the smallest grains (left) and largest grains (right) included in the composite clouds. The largest grains dominate the optical depth in a cloud of particles released with a Dohnanyi crushing law.

Models constructed in this fashion are more greatly affected by the smallest grains. Hence, the top right panel does not greatly resemble the lower right panel in Figure 3.10.

3.4.2 Semi-analytic treatment

We can further develop these ideas with a simple semi-analytic treatment. For a given planet mass and semi-major axis, the contrast function (see Equation 3.4) becomes $C(s)$, where s is the particle size. We approximate the contrast function in Equation 3.4 with the piecewise function

$$C(s) = \begin{cases} 1 & \text{for } s < s_1 \\ \left(\frac{s}{s_1}\right)^m & \text{for } s_1 < s < s_2 \\ C_{\text{large}} & \text{for } s > s_2, \end{cases} \tag{3.7}$$

where $C_{\text{large}} = 1 + p_1$ is the contrast for the largest particles, m is the logarithmic slope of the contrast in the transition regime, and s_1 and s_2 are the particle sizes that mark the beginning and end of the transition regime, respectively. We fit our contrast data with this piecewise function and obtained the following power law estimates assuming silicate grains ($\rho \sim 2$ g cm^{-3}):

$$C_{\text{large;AA,IE}} \approx 1 + 4.38 \left(\frac{M_{\text{p}}}{M_{\oplus}}\right)^{0.19} \tag{3.8}$$

$$m \approx 0.6 \left(\frac{M_{\text{p}}}{M_{\oplus}}\right)^{0.18} \tag{3.9}$$

$$\left(\frac{s_1}{1\ \mu\text{m}}\right) \approx 10 \left(\frac{M_{\text{p}}}{M_{\oplus}}\right)^{-1.12} \left(\frac{a_{\text{p}}}{1\ \text{AU}}\right)^{-0.5} \tag{3.10}$$

$$\left(\frac{s_2}{1\ \mu\text{m}}\right) \approx 150 \left(\frac{M_{\text{p}}}{M_{\oplus}}\right)^{-1.35} \left(\frac{a_{\text{p}}}{1\ \text{AU}}\right)^{-0.5} \tag{3.11}$$

In the same manner as Section 3.3.2, we defined the contrast of any ring structure as the surface density within the ring, $\sigma_{\rm ring}$, divided by the background surface density, $\sigma_{\rm BG}$. The contrast in optical depth of a cloud containing several components of various sized particles, labeled with the index i, is

$$\langle C_\tau \rangle = \frac{\sum_i C_i \sigma_{{\rm BG},i} A_i}{\sum_i \sigma_{{\rm BG},i} A_i}, \tag{3.12}$$

For a collisionless cloud with a continuous distribution of grain sizes, the contrast in optical depth of the composite cloud is given by

$$\langle C_\tau \rangle = \frac{\int_{s_{\rm min}}^{s_{\rm max}} s^{3-\alpha} C(s)\, ds}{\int_{s_{\rm min}}^{s_{\rm max}} s^{3-\alpha}\, ds}, \tag{3.13}$$

where we have explicitly included the particle cross section ($A(s) \propto s^2$) and background surface density ($\sigma_{\rm BG}(s) \propto s^{1-\alpha}$). For a collisionless cloud, the background surface density is enhanced by a factor of s due to the PR time scaling as s (see Section 3.4.1), and a factor of $s^{-\alpha}$, which describes the assumed crushing law.

Using Equations 3.7, we can now integrate Equation 3.13 directly. Assuming

$s_{\min} < s_1 < s_2 < s_{\max}$ and $(s_{\min}/s_{\max})^{|4-\alpha|} \ll 1$ when $\alpha \neq 4$, we find

$$\langle C_\tau \rangle = \begin{cases} C_{\text{large}} - \left(\frac{s_2}{s_{\max}}\right)^{4-\alpha} \left[C_{\text{large}} - \frac{4-\alpha}{4-\alpha+m}\left(\frac{s_2}{s_1}\right)^m\right] + \frac{m}{4-\alpha+m}\left(\frac{s_1}{s_{\max}}\right)^{4-\alpha} & \text{for } \alpha < 4 \\ \left(\ln\left(\frac{s_1}{s_{\min}}\right) + C_{\text{large}} \ln\left(\frac{s_{\max}}{s_2}\right) + m^{-1}\left[\left(\frac{s_2}{s_1}\right)^m - 1\right]\right) / \ln\left(\frac{s_{\max}}{s_{\min}}\right) & \text{for } \alpha = 4 \\ 1 + \left(\frac{s_2}{s_{\min}}\right)^{4-\alpha} \left[C_{\text{large}} - \frac{4-\alpha}{4-\alpha+m}\left(\frac{s_2}{s_1}\right)^m\right] - \frac{m}{4-\alpha+m}\left(\frac{s_1}{s_{\min}}\right)^{4-\alpha} & \text{for } \alpha > 4, \\ & \alpha \neq 4+m \\ 1 + C_{\text{large}}\left(\frac{s_2}{s_{\min}}\right)^{4-\alpha} - \left(\frac{s_1}{s_{\min}}\right)^{4-\alpha}\left(1 + \ln\left(\frac{s_2}{s_1}\right)\right) & \text{for } \alpha > 4, \\ & \alpha = 4+m. \end{cases} \tag{3.14}$$

For cases in which the maximum particle size in a disk is less than s_2 (see Equation 3.11), simply replace all instances of s_2 in Equations 3.14 with $s_{\max}$. Similarly, for cases in which the minimum particle size in a disk is greater than s_1 (see Equation 3.10), replace all instances of s_1 with $s_{\min}$.

Equations 3.14, together with Equations 3.8–3.11, give analytic expressions for optical depth contrast in terms of M_{p}, a_{p}, $s_{\min}$, and $s_{\max}$. Although Equations 3.14 address all possible scenarios, the most plausible scenarios have crushing laws with $\alpha < 4$ (e.g. Durda et al., 2007). With this assumption, Equations 3.14 combined

with Equations 3.8–3.11 gives

$$\langle C_{\tau;\mathrm{AA,IE}} \rangle \approx \begin{cases} 1 + 4.4 M_{\mathrm{p}}'^{0.19} + s_{\max}'^{\alpha-4} X \left[\left(10 M_{\mathrm{p}}'^{-1.12} a_{\mathrm{p}}'^{-0.5} \right)^{4-\alpha} \right. \\ \qquad \left. - \left(1 + 4.4 M_{\mathrm{p}}'^{0.19} \right) \left(150 M_{\mathrm{p}}'^{-1.35} a_{\mathrm{p}}^{-0.5} \right)^{4-\alpha} \right] & \text{for } s_{\max} > s_2 \\ \\ X s_{\max}'^{\alpha-4} \left(10 M_{\mathrm{p}}'^{-1.12} a_{\mathrm{p}}'^{-0.5} \right)^{4-\alpha} \\ \qquad + (1 - X) \, s_{\max}'^{0.6 M_{\mathrm{p}}'^{0.18}} \left(10 M_{\mathrm{p}}'^{-1.12} a_{\mathrm{p}}'^{-0.5} \right)^{-0.6 M_{\mathrm{p}}^{0.18}}, & \text{for } s_{\max} < s_2 \end{cases} \tag{3.15}$$

where $M_{\mathrm{p}}' = \left(\frac{M_{\mathrm{p}}}{M_{\oplus}} \right)$, $a_{\mathrm{p}}' = \left(\frac{a_{\mathrm{p}}}{1 \text{ AU}} \right)$, $s_{\max}' = \left(\frac{s_{\max}}{1 \ \mu\mathrm{m}} \right)$, and $X = \frac{0.6 M_{\mathrm{p}}'^{0.18}}{4 - \alpha + 0.6 M_{\mathrm{p}}'^{0.18}}$.

If, as in our first composite model in Section 3.4.1, we assume that the particles are released from their parent bodies in accordance with the Dohnanyi (1969) crushing law and then spiral inward without colliding, $\alpha = 3.4$. In this case, Equations 3.14 give a contrast in optical depth of $\langle C_\tau \rangle \approx C_{\mathrm{large}}$ in the limit $s_{\max} \gg s_2$. This result confirms our numerical results for our first composite model, shown in the upper left panel of Figure 3.10; the contrast in optical depth is dominated by the large particles.

For our second composite model, we forced the background density to obey a Dohnanyi distribution at $\sim 3a_{\mathrm{p}}$, i.e. $\sigma_{\mathrm{BG}}(s) \propto s^{-3.5}$, so that $\alpha = 4.5$. This technique essentially removes the factor of s in the background surface density that results from the PR time scaling as s. For the composite cloud shown in Figure 3.10, $M_{\mathrm{p}} = 2.0 \ M_{\oplus}$, and $a_{\mathrm{p}} = 6.0$ AU, for which $m \approx 0.68$, $s_1 \approx 1.9 \ \mu$m, $s_2 \approx 24 \ \mu$m, and $C_{\mathrm{large,AA,IE}} \approx 6$. We let each simulated particle size represent a range of particle sizes using the midpoint method, which gives $s_{\min} \approx 0.7 \ \mu$m. With these values, Equations 3.14 give a contrast in optical depth of $\langle C_{\tau,\mathrm{AA,IE}} \rangle \approx 2.4$, in agreement

with the measured contrast of ≈ 2.5 in the top right panel of Figure 3.10.

Figure 3.11 illustrates in general how a distribution of particle sizes affects the contrast of a ring structure. This figure compares the contrast of a collisionless multi-particle-size cloud (Equations 3.14) to that of a single-particle-size cloud as a function of $\sqrt{a_{\rm p}}/\beta_{\rm min}$ assuming a Dohnanyi (1969) crushing law. Both kinds of clouds have the same contrast in the adiabatic limit (large $\sqrt{a_{\rm p}}/\beta_{\rm min}$), but the contribution of the smaller grains reduces the contrast elsewhere, effectively broadening the transition between the no-trapping regime and saturation regime. Crushing laws with $\alpha < 3.4$ result in contrast curves that more closely resemble the single-particle-size contrast curves shown in Figure 3.11.

In a real zodiacal cloud, collisions affect the distribution of grains, even far from the source of the grains. Our composite dust cloud models do not include collisions and become unreliable for particles with collisional times less than their PR times. Our composite models also lack the structural results of collisional effects, such as the loss of particles as a function of circumstellar distance (Wyatt, 2005) and any potential morphological effects in the ring structure.

More sophisticated models may be required to investigate these phenomena. However, since dust produced according to a Dohnanyi (1969) crushing law or a Durda et al. (2007) crushing law yields a cloud dominated by the largest grains, as we showed above, we hypothesize that resonant rings in exozodiacal clouds may often be dominated by a single particle size whose PR time is roughly equal to the its collisional time.

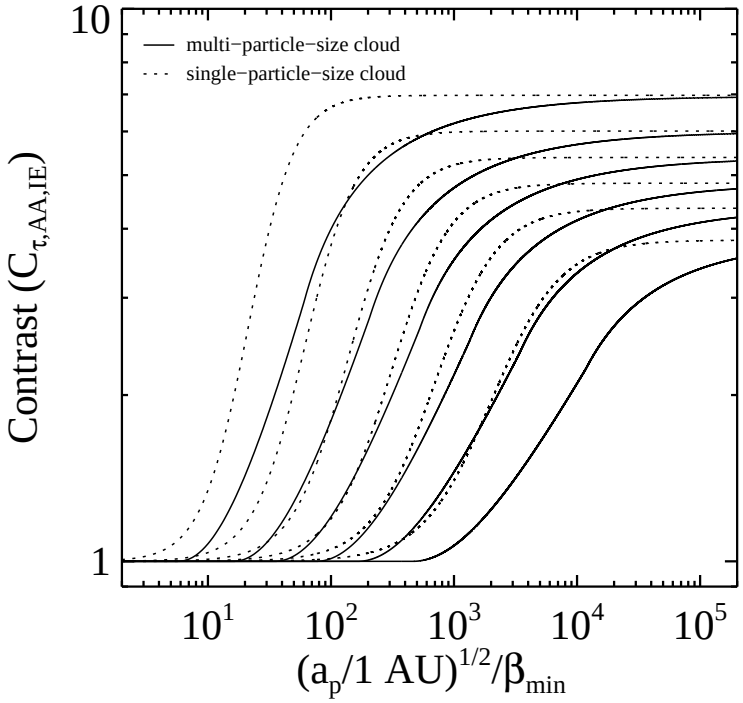

Figure 3.11: Contrast in optical depth for multi-particle-size clouds (solid lines) compared to single-particle-size clouds (dashed lines) assuming a Dohnanyi (1969) crushing law ($\alpha = 3.4$; see Equations 3.16). From top to bottom, the six solid lines and six dashed lines correspond to six values of planet mass: 5, 2, 1, 0.5, 0.25, and 0.1 $M_\oplus$. The contributions of the small grains reduce the contrasts of the multi-particle-size clouds compared to single-particle-size clouds with the same minimum value of β.

3.4.3 Ring detectability

The detectability of a resonant ring structure depends on many factors specific to the telescope being used and the observing conditions. We address this complicated issue by imposing one simplifying assumption: a minimum detectable optical depth ring contrast of 1.5. This assumption likely underestimates the sensitivity of a TPF-like mission to rings in exozodiacal clouds analogous to the solar zodiacal cloud. In such a cloud, a ring 0.4 AU wide located at 1 AU from the star has ~ 15 times the total flux of an Earth-like planet at 1 AU, even for a contrast of unity. Our assumption, conservative on the basis of photon noise alone, allows for the possibility of unknown systematic noise that could hinder the detection of extended structures.

Figure 3.12 shows the minimum detectable planet mass as a function of semi-major axis and maximum dust particle size based on Equations 3.15 and a Dohnanyi (1969) crushing law. The masses and semi-major axes of Earth, Mars, and the planet OGLE-2005-BLG-390Lb, detected by the microlensing technique (Beaulieu et al., 2006), are marked for reference. This plot shows that an Earth-mass planet at 1 AU might be detectable if the ring contains grains more than a few tens of microns in size and a planet with mass equal to a few times that of Mars might be detectable near 10 AU if the ring contains grains more than one hundred microns in size.

The detectability of a ring structure depends upon the size distribution of dust within the ring structure. Dust produced according to a crushing law less steep than the Dohnanyi (1969) crushing law ($\alpha < 3.4$) will result in more highly contrasted

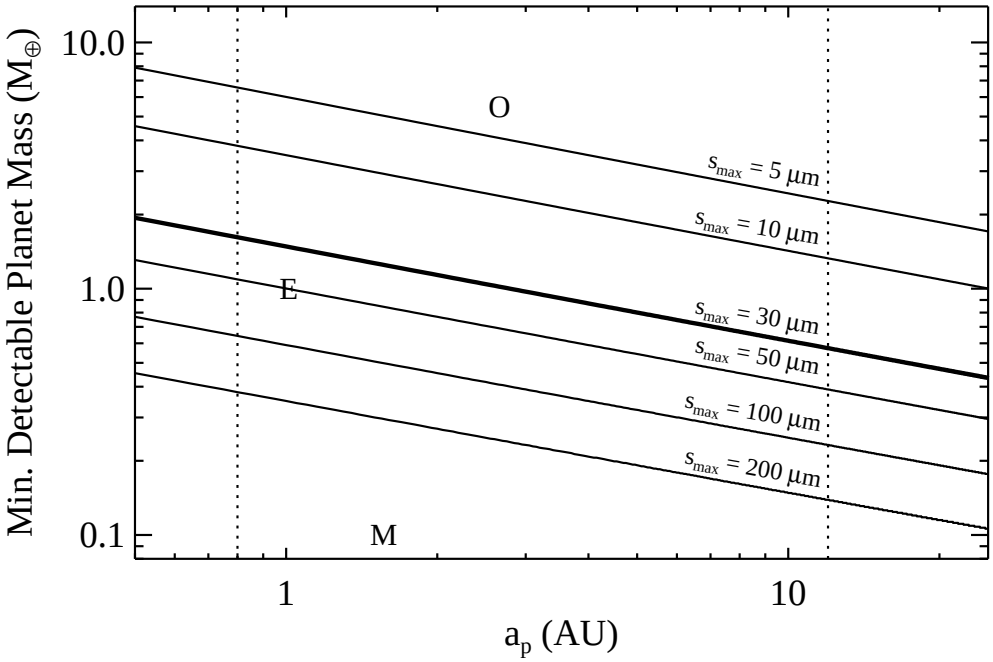

Figure 3.12: Minimum detectable planet mass in a multi-particle-size collisionless cloud as a function of semi-major axis and maximum grain size, assuming a Sun-like star, a minimum detectable ring contrast of $C_{\tau,\mathrm{AA,IE}} = 1.5$, and dust produced according to a Dohnanyi (1969) crushing law ($\alpha = 3.4$). Earth-like and Mars-like planets are denoted with an E and M, respectively. The $5.5\,M_\oplus$ exoplanet OGLE-2005-BLG-390Lb is denoted with an O (Beaulieu et al., 2006). Listed values for maximum dust size in the ring structure assume perfectly absorbing spherical grains with mean density $\rho = 2.0$ gm cm^{-3} and radius $s_{\max}$. The bold line shows the case of the solar zodiacal cloud, for which the observed emission is dominated by 30 μm grains (Fixsen & Dwek, 2002). The dashed lines show typical inner and outer detection limits for a mission similar to TPF.

ring structures because of the increased relative contribution of the large grains. For crushing laws with $\alpha = 3$ and $\alpha = 2$, the curves of constant maximum particle size shown in Figure 3.12 shift downward by a factor of approximately 1.25 and 1.55, respectively.

These values are subject to the assumptions of our simulations, which do not include a dynamically hot component in the dust cloud. This component would reduce the contrast in the ring, making planets harder to detect for a given cloud mass. So the detection limits shown in Figure 3.12 should be thought of as best-case scenarios.

3.5 Caveats

Our simulations include a number of simplifying assumptions, which we summarize here. We ignored the effects of dynamically hot dust, like dust that might come from comets. Trapping probability decreases dramatically for particles on highly eccentric and inclined orbits, so we expect dynamically cold dust to dominate any resonant debris disk structure. As a first approximation, we can treat the contribution from the dynamically hot dust as a constant surface density cloud component, which reduces the contrast of any structure formed from the dynamically cold component. Estimates of the ratio of asteroidal dust to cometary dust in the Solar System range from 1:10 to 7:10 (Ipatov et al., 2008). For other systems, this ratio is also unknown.

Our simulations also assumed a single planet on a circular orbit around a

Sun-like star. We have performed trial simulations of the Solar System and demonstrated that the presence of Jupiter may reduce the Earth's ring contrast. Other multiple-planet systems may also exhibit a similar effect. Additionally, planets on eccentric orbits give rise to additional MMRs with different capture probabilities and geometries (Kuchner & Holman, 2003).

The ring contrasts of inclined systems can vary significantly depending on the inclination and radial extent of the dust cloud. In edge-on systems, resonant features can overlap as seen from the Earth, complicating their interpretation. The contrasts we provide are useful only to systems for which projection effects can be taken into account.

Finally, our multi-particle-size models demonstrate the subtlety of collisional effects in dust clouds. Collisional effects can determine the relative populations of large and small grains and potentially alter the morphology of the ring structures. Our simulations can not yet handle these effects in detail.

3.6 Conclusions

We have implemented our own hybrid symplectic integrator for the n-body problem and used it to simulate collisionless debris disks, taking into account solar wind and drag effects. Each simulation contained 5,000 particles. We found that this number of particles suffices to populate the dominant MMRs of a low-mass planet with an accuracy at the few percent level, yielding for the first time models of the surface brightness distributions of exozodiacal clouds that we can use to

quantitatively study the contrasts of resonant features—not just their geometries.

We generated a catalog of resonant structures induced by a single planet on a circular orbit around a Sun-like star, available online at http://asd.gsfc.nasa.gov/Christopher.Stark/catalog.php. We investigated 120 sets of model parameters, spanning a range of planet masses, planet semi-major axes, and values for β, assuming dust grains launched from orbits with low $e_{\rm dust}$ and $i_{\rm dust}$. The resulting ring structures exhibited leading-trailing asymmetries, gaps near the locations of the planets, and sharp inner edges at $\approx 0.83 a_{\rm p}$.

We performed a detailed analysis of the surface density contrasts of the rings (Figure 3.9). We showed that for a planet on a circular orbit, the contrast and morphology of the rings are to good approximation functions of only two parameters, $M_{\rm p}$ and $\sqrt{a_{\rm p}}/\beta$, for a given stellar mass and distribution of dust sources for $M_{\rm p} \lesssim 5\ M_{\oplus}$ and $\beta \lesssim 0.25$. Equation 3.4 summarizes the contrasts of our single-particle-size models as a function of these parameters. Considering only the dynamically cold particles analogous to particles released by asteroids in the Solar System, we find that terrestrial-mass planets are capable of producing resonant ring structures with azimuthally averaged contrasts up to $\sim 7:1$.

By combining our simulations of grains with particular β values, we assembled multi-particle-size models of 25,000 particles each. Releasing the particles according to a Dohnanyi (1969) crushing law without any subsequent collisional processing results in composite clouds whose optical depths are dominated by large particles; large particles will dominate images of these clouds in visible light and throughout the IR. Based on these composite models, we suggested that the best current models

for exozodiacal clouds are those with a narrow range of grain sizes corresponding to grains whose collision time roughly equals their PR time. Future models should account for processes like grain-grain collisions that destroy large grains.

Equations 3.14 and 3.15 provide semi-analytic predictions for the contrast in optical depth of a multi-particle-size cloud of dynamically cold grains. For ring structures composed of silicate grains released according to a Dohnanyi crushing law ($\alpha = 3.4$), Equation 3.15 gives an approximate contrast of

$$\langle C_{\tau;\mathrm{AA,IE}} \rangle \approx \begin{cases} 1 + 4.4 \left(\frac{M_\mathrm{p}}{M_\oplus}\right)^{0.19} - 52 \left(\frac{s_\mathrm{max}}{1\ \mu\mathrm{m}}\right)^{-0.6} \left(\frac{a_\mathrm{p}}{1\ \mathrm{AU}}\right)^{-0.3} \left(\frac{M_\mathrm{p}}{M_\oplus}\right)^{-0.57} & \\ & \text{for } s_\mathrm{max} > s_2 \\ \frac{1}{1+\left(\frac{M_\mathrm{p}}{M_\oplus}\right)^{0.18}} \left[4 \left(\frac{s_\mathrm{max}}{1\ \mu\mathrm{m}}\right)^{-0.6} \left(\frac{M_\mathrm{p}}{M_\oplus}\right)^{-0.49} \left(\frac{a_\mathrm{p}}{1\ \mathrm{AU}}\right)^{-0.3} \right. & \\ \left. \quad + \left(4 \left(\frac{s_\mathrm{max}}{1\ \mu\mathrm{m}}\right)^{-0.6} \left(\frac{M_\mathrm{p}}{M_\oplus}\right)^{-0.67} \left(\frac{a_\mathrm{p}}{1\ \mathrm{AU}}\right)^{-0.3} \right)^{-\left(\frac{M_\mathrm{p}}{M_\oplus}\right)^{0.18}} \right] & \\ & \text{for } s_\mathrm{max} < s_2 \end{cases} \tag{3.16}$$

where $\langle C_{\tau;\mathrm{AA,IE}} \rangle$ is the ratio of the azimuthally averaged optical depth in the ring structure to the azimuthally averaged background optical depth, s_max is the maximum grain size in the ring structure, and s_2 is given by Equation 3.11. For the case $s_\mathrm{max} > s_2$, the first two terms in Equation 3.16 represent the contrast in the adiabatic limit. The remaining term (and the terms in the $s_\mathrm{max} < s_2$ case) represents deviations from this limit for smaller particles or smaller semi-major axes.

We plotted the mass of the smallest planet that could be detected through observation of a resonant ring structure as a function of planet semi-major axis and

particle size in Figure 3.12. We assumed a cloud composed of a range of particle sizes adhering to a Dohnanyi (1969) crushing law and a minimum detectable optical depth contrast of 1.5:1. We found that planets with masses just a fraction of the Earth's may form detectable ring structures if the rings harbor grains more than several tens of microns in size.

Chapter 4

Incorporating collisions into dynamical models of debris disks

4.1 Introduction

Recent resolved images of several debris disks reveal complex structures in the form of rings, gaps, and warps carved in the circumstellar dust (e.g. Greaves et al., 1998; Wilner et al., 2002; Kalas et al., 2005; Golimowski et al., 2006; Schneider et al., 2009). Some of these structures are likely the result of planetary companions that gravitationally perturb the disk (e.g. Quillen, 2006; Chiang et al., 2009). Modeling these structures can potentially reveal the physical and orbital parameters of the planets, dust grains, and sources of dust in these systems, helping us better understand the late stages of planet formation that debris disks represent (e.g. Zuckerman, 2001; Wilner et al., 2002; Moran et al., 2004; Deller & Maddison, 2005; Wyatt et al., 2007; Stark & Kuchner, 2008).

So far all resolved debris disks are collisionally-dominated systems, meaning the collision time, $t_{\rm coll}$, is much shorter than the PR time, $t_{\rm PR}$, in these disks (Wyatt,

2005). For example, $t_{\rm PR}/t_{\rm coll}$ is $\sim$300 for 10 μm grains in the resolved circumstellar dust rings of Fomalhaut (Chiang et al., 2009) and HR 4796A (Debes et al., 2008; Schneider et al., 2009). Many different modeling techniques have been applied to these disks. However, no model has yet been able to accurately treat gravitational dynamics and collisions simultaneously in a self-consistent fashion.

Some models of dust in debris disks ignore collisions altogether (e.g. Moran et al., 2004; Deller & Maddison, 2005). Some variations on collisionless disk models simply stop the integration of the particle orbits once dust grains have lived as long as their collisional time (e.g. Chiang et al., 2009). The collision time is typically estimated via Equation 1.5. These models do not include the influence of disk asymmetries and orbital resonances on collision rates.

Other models of dusty disks avoid treating the resonant dynamics of the grains altogether, opting instead to investigate the long-term collisional evolution of debris disks with simple geometries. Analytic models of azimuthally symmetric steady-state collisional disks with a single belt of parent bodies help us develop our intuition about these systems (e.g. Wyatt, 1999; Wyatt et al., 2007). Numerical kinetic models, which treat collisions with great detail by including processes such as grain fragmentation and cratering (e.g. Thébault et al., 2003; Löhne et al., 2008), specialize in the long-term behavior of the radial and grain size distributions of dust in disks, and do not include planets. The hybrid model of Bromely & Kenyon (2006) merges kinetic models with n-body models by combining a multi-annulus kinetic model which treats small dust grains with an n-body model to treat large planetesimals. However, this code is tailored for grain growth simulations and not resonant

structures in debris disks; it does not model the resonant dynamics of the dust grain population.

Still other models look at only the transient effects of collisions. The collisional code of Grigorieva et al. (2007) is designed for modeling collisional avalanche events in debris disks, but does not have the spatial resolution necessary to model structures caused by gravitational resonant dynamics. Robust many-particle simulations that model individual collisional events and follow the orbits of any fragments produced are currently limited by computer processing power to $\sim 10^4$ particles for long-term integrations (e.g. Leinhardt et al., 2009), restricting their debris disk application to short-term integrations or integrations sampling limited phase space.

Here we present a novel "collisional grooming" algorithm for treating collisions and resonant dynamics self-consistently in an optically thin disk. The algorithm produces a dust distribution for each grain size that simultaneously solves the equation of motion for small dust grains,

$$\frac{d^2\mathbf{r}}{dt^2} = -\frac{GM_\star}{r^2}(1-\beta)\hat{\mathbf{r}} - \frac{(1+\mathrm{sw})\beta}{c}\frac{GM_\star}{r^2}[\dot{r}\hat{\mathbf{r}} + \mathbf{v}] + \sum_i \frac{Gm_i}{|\mathbf{r}_i - \mathbf{r}|^3}(\mathbf{r}_i - \mathbf{r}) \ , \quad (4.1)$$

and the particle number flux equation in 3D,

$$\nabla \cdot (n\overline{\mathbf{v}}) - \frac{\partial n}{\partial t} = \frac{\partial n}{\partial t}\Big|_{\mathrm{coll}} \ . \quad (4.2)$$

Here G is the gravitational constant, $M_\star$ is the stellar mass, c is the speed of light, $\mathbf{r}$ and $\mathbf{v}$ are the heliocentric position and velocity of the grain, β is the ratio of radiation pressure force to gravitational force on a grain, sw is the ratio of solar wind drag to PR drag, and m_i and $\mathbf{r}_i$ are the mass and heliocentric position of the i^{th} planet. The particle number density, n, the mean flow velocity, $\overline{\mathbf{v}}$, and the

particle number density removed or added by collisions per unit time, $\partial n/\partial t|_{\rm coll}$, may be functions of position and grain size.

Our algorithm uses a collisionless disk simulation (a "seed model") as input to calculate initial collision rates, similar to the method developed by Charnoz & Morbidelli (2003). However, our algorithm differs from that of Charnoz & Morbidelli (2003) in several ways. Our algorithm includes Poynting-Robertson drag and is therefore applicable to systems with small dust grains. Our algorithm also allows for the possibility that collisions can affect the dynamics of the system, and it uses an iterative scheme to find the correct density distribution for a steady-state disk. After the integration of the seed model, the algorithm can be run on a single processor in $\sim$1 hour. This algorithm can generate new models that should allow us to interpret images of collision-dominated disks like those orbiting Fomalhaut, Vega, Epsilon Eridani, and HR 4796A quantitatively for the first time.

4.2 Numerical method

4.2.1 Collisionless seed models

We first run a seed model, a model of a steady-state collisionless debris disk. We numerically integrate Equation 4.1 for a collection of particles launched from parent bodies orbiting a star. This equation includes the dynamical effects of gravity, radiation pressure, corpuscular drag, and PR drag (see Stark & Kuchner, 2008, for details). The drag forces cause the particles to slowly lose angular momentum and spiral inward from the parent bodies from which they were launched.

During their journey inward toward the star, the particles can become temporarily trapped in the external mean motion resonances (MMRs) of any planets present, creating an overdense circumstellar ring structure near the planet's orbit. We use enough particles, typically on the order of a few thousand, to accurately populate the external MMRs of the planets (Stark & Kuchner, 2008). During the integration, we record the barycentric coordinates of each particle at a regular interval, $t_{\rm record}$. This commonly-used technique extrapolates the results of a few thousand particles to millions of particles (e.g. Dermott et al., 1994; Liou & Zook, 1999; Moro-Martín & Malhotra, 2002; Moran et al., 2004). Our algorithm requires the local velocity distribution to calculate the local collision rate, so we also record the barycentric velocities of each particle at the same interval, $t_{\rm record}$.

We then place all of the records of the barycentric coordinates and velocities into a 3D spatial grid of bins, forming a 3D histogram that represents the distribution function for the collisionless system. Panel *b* in Figure 4.1 shows the histogram of the particle density viewed face-on for a collisionless disk model with a resonant ring created by an Earth-mass planet on a circular orbit at 1 AU around the Sun, using a grid bin size of 0.05 AU. Panel *a* shows the velocity records from three of these bins located in the midplane of the disk, pointed to in panel *b*.

Exterior to the resonant ring structure in Figure 4.1, the velocity distribution is approximately Gaussian and the dispersion in the radial direction is approximately twice the dispersion in the azimuthal direction, as expected for a Keplerian disk (e.g. Binney & Tremaine, 1987). However, within the resonant ring structure the velocity distribution is highly non-Gaussian and the velocity dispersion varies greatly from

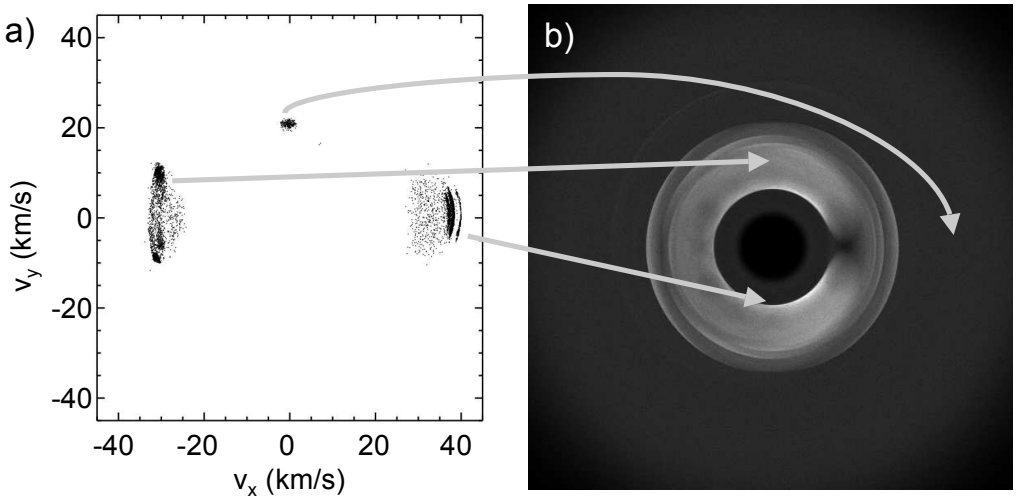

Figure 4.1: Velocity distributions (a) at three locations (b) in a collisionless dust disk with a resonant ring structure caused by an Earth-mass planet at 1 AU. The velocity distributions in the resonant ring structure vary greatly and are non-Gaussian.

one location to another. This illustration shows that to calculate the collision rates in a resonant ring we must explicitly calculate the local velocity distribution.

4.2.2 The collisional grooming algorithm

Besides the distribution function, recording the barycentric coordinates and velocities of all particles at regular intervals during the integration of the seed model yields a second important ingredient for our algorithm—a chronological record of each particle's trajectory, which we refer to as a "stream." We let each stream from our seed model represent a large number of particles, which varies from record to record, i.e. the i^{th} record is scaled to N_i particles. We adjust the scaling factor to control the mean collision time of the particles.

We initially assume collisions only serve to remove material from a stream. As they progress through the cloud, the streams become attenuated by collisions with other streams as

$$N_i = N_{i-1}\, e^{-\tau_{\text{coll},i}}, \tag{4.3}$$

where N_i is the number of particles in the i^{th} record of a given stream and $\tau_{\text{coll},i}$ is the collision depth for the i^{th} record. Equation 4.3 is analogous to the solution to the radiative transfer equation for photons passing through an absorptive medium. We approximate the collisional depth as

$$\tau_{\text{coll},i} \approx \sum_k n_k \sigma_k |\mathbf{v}_i - \mathbf{v}_k| t_{\text{record}}, \tag{4.4}$$

where $\mathbf{v}_i$ is the velocity associated with the i^{th} record of the given stream, n_k, σ_k, and $\mathbf{v}_k$ are the particle number density, collisional cross-section, and velocity of the

other records in the same bin as the i^{th} record, and n_k is equal to N_k divided by the bin volume. This approximation works as long as $t_{\text{record}} \ll t_{\text{coll}}$. We perform this calculation for all records in all particle streams, one at a time, from the first record to the last record in each stream.

After only one pass through all of the records for all streams, i.e., one iteration, the particle streams will be attenuated incorrectly; the streams will be attenuated based on the density distribution of the collisionless seed model, which overestimates the particle density and therefore the collision rate. To remedy this problem, we iterate the attenuation process of all records until no record changes by more than a set tolerance of a few percent. By doing so, we ensure that the final number density histogram approximately satisfies Equation 4.2 in the steady state.

Figure 4.2 shows an example of the grooming algorithm at work. The top-left panel shows the surface density of a collisionless disk scaled by $1/r^2$, where r is circumstellar distance. The disk of 120 μm grains features a ring structure caused by an Earth-mass planet on a circular orbit at 1 AU around a Sun-like star. We applied our collisional grooming algorithm to the disk and scaled the number of particles per stream equally among all streams such that $\eta_0 \approx 3.7$, where $\eta_0 = t_{\text{PR}}(r_0)/t_{\text{coll}}(r_0)$ and r_0 is the mean circumstellar distance at which grains are launched.

After the first iteration, shown in the top-middle panel, the collision rates are overestimated so that the surface density in the inner disk is too low. During the second iteration, shown in the top-right, the algorithm underestimates the collision rates. The algorithm alternates between over- and underestimating the collision rates while converging on the correct solution.

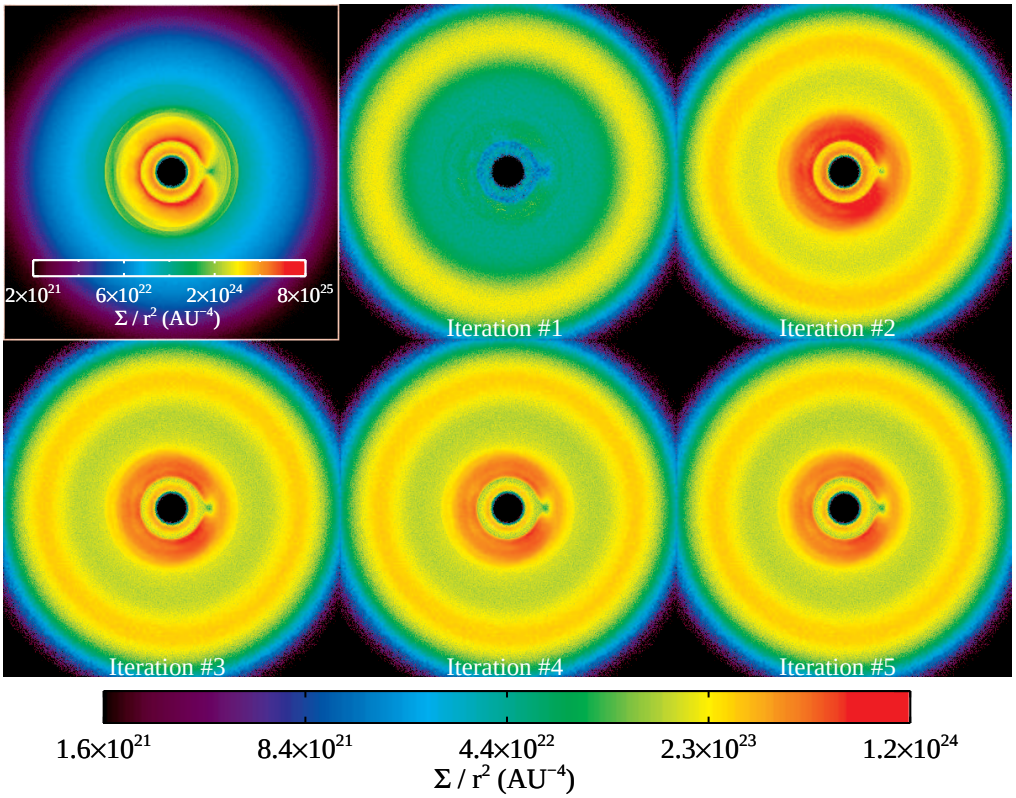

Figure 4.2: Surface density scaled by $1/r^2$ of a collisional model as a function of iteration number. The upper-left panel shows the surface density of the seed model, a collisionless disk with a resonant ring structure (see Section 4.2.3 for simulation details). The iterations alternate between over- and underestimating the amount of collisions while converging on the correct solution.

Our algorithm uses a finite grid of bins to approximate the local density and velocity structure, so Poisson noise can become an issue in bins with few records. To help mitigate this Poisson noise, we use a nearest-neighbor averaging routine. For bins with fewer than 10 records, we include the records from the six nearest-neighbor bins in the calculation of $\tau_{\rm coll}$. We weight the records in each nearest-neighbor bin at 50% of the weight of the central bin.

Our calculation of the collisional depth (Equation 4.4) trivially handles seed models with multiple grain sizes. Given an initial distribution of grain sizes, the algorithm can simultaneously solve for the collisional interactions among all grains of all sizes included in the seed model. The algorithm can model complex phenomena that depend on grain size, such as size-dependent collision rates, radial transport rates, and resonant structure morphologies.

Equation 4.3 ignores any fragments that may be produced by collisions. Treating collisions as non-productive is not valid for all collisions in all debris disks, but it is likely acceptable in a wide range of cases. Backman & Paresce (1993) argued that in the inner Solar System, grain-grain collision velocities are high enough (on the order of a few kilometers per second) that grains fragment catastrophically during any collision, and any fragmentation products are either gas or small enough to be removed immediately by radiation pressure. In resonant ring structures, like the circumsolar ring created by Earth, the collision velocities can be even higher, on the order of tens of kilometers per second (c.f. Figure 4.1). In the outer Solar System, where collision velocities are lower, grains probably resemble cometary grains. Samples of cometary interplanetary dust particles directly returned from the Stardust

mission and observations of cometary ejecta during the Deep Impact mission reveal that the majority of observed cometary particles are loosely bound aggregates of submicron-sized grains, which can easily be shattered into unbound β-meteoroids (A'Hearn et al., 2005; Brownlee et al., 2006; Zolensky et al., 2006).

Our algorithm can also be adapted to handle particle fragmentation. We discuss this feature in Section 4.4.

4.2.3 Tests

We developed a collisional disk modeling code based upon the algorithm described above. We subjected our code to a battery of tests to confirm its operation and identify its limits. Here we demonstrate the algorithm's performance, show that it converges on a unique and correct solution, and place limits on the conditions under which it is valid. For now, we neglect fragmentation; we assume non-productive collisions.

Below, we will refer to an analytic solution for the surface density as a function of circumstellar distance for a planet-less disk. Wyatt (1999) showed that Equation 4.2 has the following steady-state solution for an azimuthally-symmetric disk with a single grain size and grain mass under the assumption that collisions create no daughter particles:

$$\Sigma(r) = \frac{\Sigma(r_0)}{1 + 4\eta_0(1 - \sqrt{r/r_0})}, \tag{4.5}$$

where Σ is the surface density and r_0 is the circumstellar distance of the dust source. If we do not add a perturbing planet, we can directly compare the results of our

algorithm to this expression.

4.2.3.1 Seed models

Throughout this paper, we will refer to two collisionless disk simulations which we use as seed models: a planet-less disk simulation and a simulation of a disk with a resonant ring structure. For both simulations, we integrated the orbits of 20,000 particles. Particle integrations were terminated when their semi-major axes were less than 0.5 AU, so many images will show no data interior to this radius. In many instances throughout this paper we will only examine a subset of the total number of integrated particles, and will state the number used when appropriate. All simulations were performed using a hybrid symplectic integrator (see Stark & Kuchner, 2008).

Our planet-less disk seed model contains particles with $\beta = 0.0023$, where β is the ratio of the force on the grain from radiation pressure to the gravitational force (e.g. Burns et al., 1979). For a spherical blackbody grain with a density of 2 gm cm^{-3}, $\beta = 0.0023$ corresponds to a grain radius of 120 μm around a Sun-like star. We initially placed the grains at 10 AU on circular orbits with inclinations uniformly distributed between 0 and 14°. We distributed all other initial orbital parameters (longitude of ascending node, mean anomaly, argument of pericenter) uniformly between 0 and 2π. We recorded particle positions and velocities every 6956 years.

For the second seed model, we integrated the orbits of particles with $\beta = 0.0023$

as they spiraled inward and interacted with an Earth-mass planet on a circular orbit at 1 AU around a Sun-like star. We launched grains from parent bodies with semi-major axes uniformly distributed between 3.5 and 4.5 AU, eccentricities uniformly distributed between 0 and 0.2, and inclinations uniformly distributed between 0 and 20°. We distributed all other initial orbital parameters uniformly between 0 and 2π. We recorded the particle positions and velocities once every 426 years.

4.2.3.2 Bin size test

The finite size of the bins used to approximate the local density and velocity distributions is a natural source of error for our algorithm. We need to ensure that the bins are small enough to resolve any structure within the disk. To help us decide on the appropriate bin size, we performed the following test.

We applied our collisional grooming algorithm to our seed model of a disk with a resonant ring structure. We used 15,000 simulated particles to ensure that Poisson noise was not an issue for this test. For the collisional algorithm, we scaled the number of particles per stream such that $\eta_0 \sim 1$, and used four different cubic bin sizes of 0.02, 0.05, 0.1, and 0.2 AU. For each of the largest three cases, we calculated the differences in the collision rates compared to the smallest case.

Figure 4.3 shows these relative differences in the collision rates. The left panel shows that differences in the collision rates between the 0.05 and 0.02 AU bin sizes are on the order of a few percent or less, and show no signs of structural differences. The right panel shows that using a bin size of 0.2 AU results in obvious structural

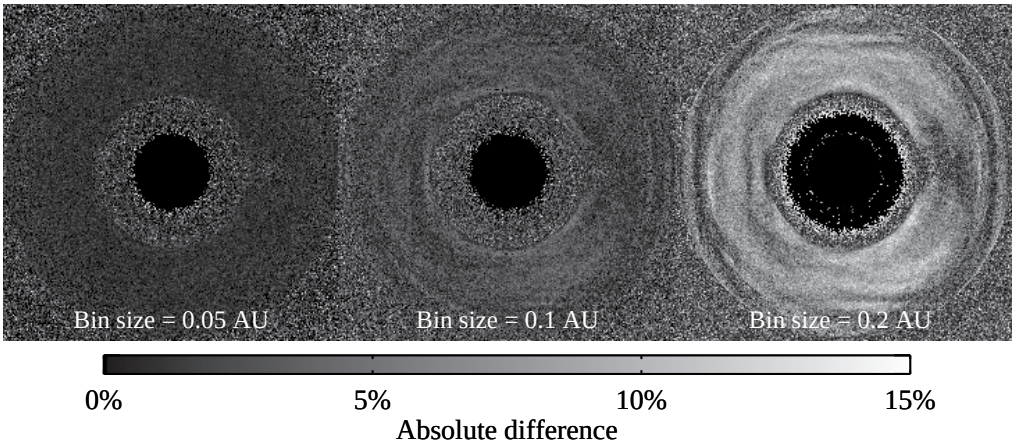

Figure 4.3: Errors in the collision rate in a model with an Earth-mass planet at 1 AU. Errors are relative to the collision rates calculated using a bin size of 0.02 AU.

differences (greater than 10%) compared to a model with a 0.02 AU bin size. The right panel also shows a subtle imprint of the grid itself, which appears as straight horizontal and vertical features in the collision rates.

In light of these results, we recommend that the bin size for collisional calculations in a debris disk with a resonant ring structure should be ~ 0.05 AU for a planet at 1 AU. The size of structural features in a resonant ring scale linearly with planet semi-major axis, $a_{\rm p}$ (Stark & Kuchner, 2008), so we suggest that in general, the optimal bin size for disks with resonant ring structures is $\sim 0.05\, a_{\rm p}$. Bins larger than this size fail to resolve the ring structure while bins smaller than this size become more susceptible to Poisson noise in the distribution function.

For collision times that are short compared to the PR time ($\eta_0 \gg 1$), grains

launched from circumstellar distance r_0 have little time to move radially inward before colliding. This process can result in a very narrow ring structure at $r = r_0$. If the bin size is larger than the width of the ring, our collisional algorithm will fail to resolve the ring. So we must also choose a bin size small enough such that the crossing time of a bin caused by PR drag at $r = r_0$ is shorter than the collision time. The bin crossing time is given by

$$t_{\rm cross}(r_0) = t_{\rm PR}(r_0) - t_{\rm PR}(r_0 - b) \ , \tag{4.6}$$

where b is the bin size and the PR time is given by Equation 1.4. With the requirement $t_{\rm cross}(r_0) \lesssim t_{\rm coll}(r_0)$ we find to first order in η_0^{-1} that the bin size must satisfy

$$b \lesssim \frac{r_0}{2\eta_0} \ . \tag{4.7}$$

4.2.3.3 Poisson noise test

If there are too few records in a given bin, Poisson noise can dominate the calculation of the collisional depth, even with our nearest-neighbor averaging routine. However, we are not specifically concerned with whether a single collisional depth calculation suffers from Poisson noise, but whether Poisson noise affects the final outcome of the simulation. To examine the effects of Poisson noise, we applied our collisional algorithm to our planet-less seed model three times, first using 15,000 simulated particles, then using 5,000 simulated particles, and then using only 1,500 simulated particles. For each application of the collisional algorithm, we used a cubic bin size of 0.05 AU. We scaled the disk such that $\eta_0 \approx 223$ for all three cases.

After processing the three disks with our collisional grooming algorithm, we azimuthally averaged each of the three resulting surface densities. Figure 4.4 shows the normalized surface density as a function of circumstellar distance for all three cases compared to the analytic solution (Equation 4.5). The 15,000-particle case follows the analytic solution well, while the 1,500-particle case deviates by a factor of ~ 2 and contains strong fluctuations caused by Poisson noise. From these simulations we estimate that the average number of records per bin near the circumstellar distance at which grains are launched should be at least on the order of a few to avoid the effects of Poisson noise.

4.2.3.4 Uniqueness of solution

Figure 4.2 shows that our algorithm does indeed converge, but does not indicate whether the algorithm converges on a unique solution. To test for uniqueness, we applied the collisional grooming algorithm to three independent seed simulations of disks with ring structures, using 5,000 particles for each simulation and a value of $\eta_0 \sim 4$. The range of initial conditions were the same for all three simulations, but individual values were generated using a different random number seed.

We compared the resulting surface densities of all three collisional disks. Except for the outer and inner extremities of the disk where the statistics were poor, none of the final disk surface densities differ by more than a few percent and none show significant structural differences. All three independent simulations converged to the same surface density solution to within the limits of Poisson noise.

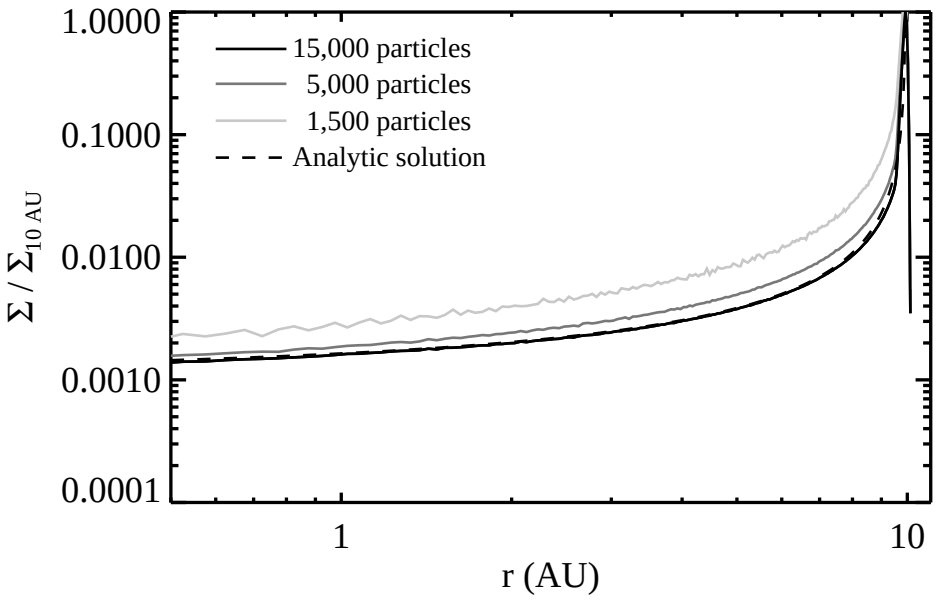

Figure 4.4: Azimuthally averaged surface density as a function of circumstellar distance in a planet-less collisional disk for three simulations with different numbers of particles (see Section 4.2.3). The 15,000-particle simulation follows the analytic solution well, but the 1,500-particle simulation deviates significantly and shows signs of Poisson noise.

4.2.3.5 Correctness of solution

To test the correctness of our algorithm's solution, we directly compared the results of our algorithm to the analytic solution for a planet-less disk of a single grain size (Equation 4.5). We applied our collisional grooming algorithm to our planet-less-disk seed model of 20,000 particles using six different values of η_0. Figure 4.5 shows the azimuthally-averaged surface densities as a function of circumstellar distance for all six cases. The calculated surface densities (solid lines) match the analytic solutions (dashed lines) well for all values of η_0 except $\eta_0 = 763$. In this case, collisions happen so quickly that the disk forms a narrow ring at 10 AU whose width is smaller than the bin size used in our algorithm (0.05 AU); this case does not meet the bin size criteria in Equation 4.7. If we used a smaller bin size, we could resolve the ring structure and investigate even larger values of η_0.

For all cases shown in Figure 4.5, $t_{\rm record} \ll t_{\rm coll}$; none of the deviations from the analytic values are caused by insufficient time sampling. We tested the algorithm's behavior when $t_{\rm record} \gtrsim t_{\rm coll}$, and confirmed that our algorithm fails under these circumstances. For $t_{\rm record} \gtrsim t_{\rm coll}$, our algorithm typically overestimates the collision rate and the result looks qualitatively similar to the $\eta_0 = 763$ case shown in Figure 4.5.

For the case of a disk with a resonant ring structure, there exists no analytic solution for the surface density with which we can compare the results of our simulations. However, we can probably assume that our collisional algorithm arrives at the correct solution if the amount of collisions is very small, i.e., $\eta_0 \ll 1$, since such

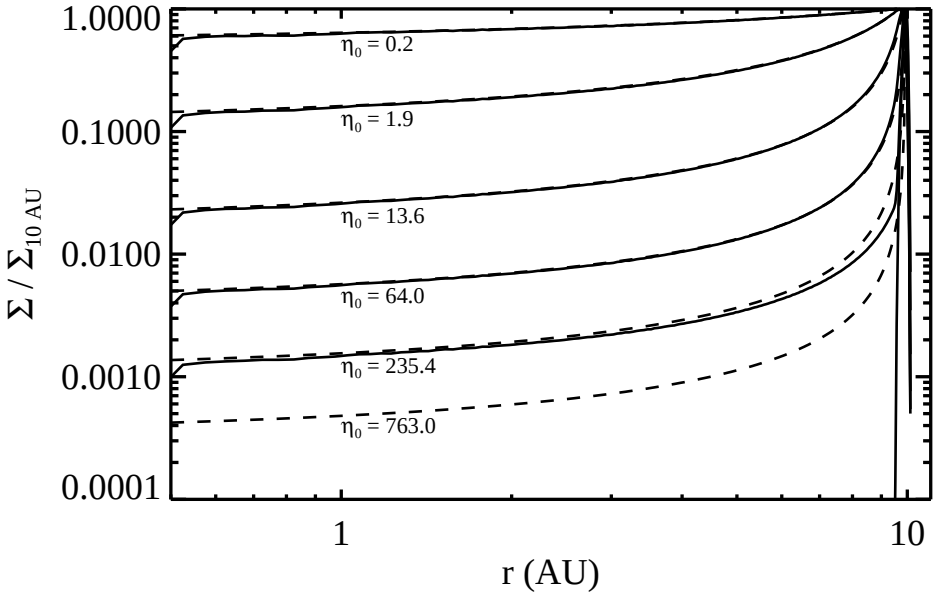

Figure 4.5: Azimuthally averaged steady-state surface density as a function of circumstellar distance for a planet-less disk undergoing PR drag and non-productive collisions. Analytic solutions are shown with dashed lines and the results of our collisional algorithm are shown with solid lines. Our algorithm gives the correct solution for all values of η_0 except the largest, at which point the collisions yield a narrow ring near 10 AU that is no longer resolved by the grid.

a disk should deviate from the collisionless case by very little. Under this assumption, we propose the following test to investigate the correctness of our algorithm's solution for a disk with a ring structure:

1. Apply our algorithm to the collisionless seed model using $\eta_0 \ll 1$.
2. Store the output of the algorithm, call it Model C.
3. Increase η_0 by a small amount $\delta\eta_0$.
4. Apply our algorithm to Model C disk using the new value of η_0.
5. Repeat steps 2 through 4 until η_0 is equal to the desired value of η_0.
6. Compare the results to a model with the same value of η_0 calculated in only one step.

We performed this test using a 5,000-particle seed model of a disk with a ring structure. We used a cubic bin size of 0.05 AU and scaled the disk density so that the final $\eta_0 \approx 3.7$. We applied the collisional grooming algorithm using 19 logarithmically-spaced steps in η_0. We compared the surface density of this disk to the surface density calculated by applying the algorithm in the usual single-step fashion. The disks differed by less than one part in $\sim 10^5$; both methods arrived at the same solution to within the limits of Poisson noise. A similar test performed in the opposite direction, i.e., slowly reducing the η_0 to the desired value, gave similar results. This test supports both the uniqueness and correctness of the solution that our algorithm finds for a collisional disk with a resonant ring structure.

4.2.3.6 Benchmark tests

We benchmarked our collisional grooming algorithm code by applying it to our seed model of a disk with a ring structure. We recorded the run time of our code using 1,250, 2,500, 3,750, and 5,000 simulated particles and cubic bin sizes of 0.05 and 0.1 AU. Table 4.1 shows the run time for a single iteration of our algorithm on a single 2.2 GHz CPU.

For each bin, the algorithm performs of order $n_{\rm b}^2$ calculations, where $n_{\rm b}$ is the number of records in that bin. So we would expect that our run time per iteration scales as $B\langle n_{\rm b}\rangle^2$, where B is the number of bins containing records, or as $\langle n_{\rm b}\rangle^2$ for a given bin size. Table 4.1 shows that the run time scales as $\langle n_{\rm b}\rangle^2$ for a bin size of 0.1 AU, but not for a bin size of 0.05 AU. In the latter case, our algorithm is working with many bins that have relatively few entries and is switching on our nearest-neighbor approximation described in Section 4.2.2, which can cause the run time to deviate from the $\langle n_{\rm b}\rangle^2$ scaling relationship.

The number of iterations required to converge on the correct solution depends on many factors, such as η_0, the number of records, the bin size, the structure of the disk, and the tolerance set for convergence. For a disk with a resonant ring structure composed of 5,000 particles, typically 5 – 10 iterations are required for better than 5% convergence with $\eta_0 \sim 1$. The total run time for such a disk typically ranges from 20 minutes to 2 hours.

Table 4.1: Bench mark tests

Number of particles	**Bin size** (AU)	**Run time per iteration**[†] (min)
1,250	0.05	0.3
2,500	0.05	0.8
3,750	0.05	1.6
5,000	0.05	2.7
1,250	0.1	1.1
2,500	0.1	4.2
3,750	0.1	9.4
5,000	0.1	16.7

[†]For a single 2.2 GHz CPU

4.2.4 Limitations

Here we summarize the current limitations of our algorithm. We have already shown that the bin size must be small enough to resolve any structural features in the disk, and the collision time must be longer than the time between records for our algorithm to converge. We also showed that the number of records per bin must be large enough to avoid the effects of Poisson noise.

The algorithm presently has another, more subtle limitation, which it shares with many collisionless steady-state disk simulations (e.g. Dermott et al., 1994; Liou & Zook, 1999; Moran et al., 2004; Deller & Maddison, 2005). As stated in Section 4.2.2, we record the coordinates and velocities of each integrated particle at regular time intervals, $t_{\rm record}$, to extrapolate the results of a few thousand integrated grains to millions of grains or more and to obtain a chronological record of each particle's trajectory. This technique implies that a new parent body launches grains every $t_{\rm record}$ with the exact same orbital parameters as the first parent body. Because our

algorithm requires the use of this technique, our algorithm implicitly assumes that each parent body's orbit is populated by many parent bodies uniformly distributed in mean anomaly and that the orbits of parent bodies do not change over the course of a collisional time.

4.3 Non-productive collisions in resonant ring structures

We can use our algorithm to investigate the effects of collisions on steady-state resonant ring structures. To this end, we ran some models of familiar kinds of disk structures. Here we discuss some of the new physical effects we have observed in our models.

The top-left panel of Figure 4.6 shows the collision rate per particle in a 0.4 AU-thick cross-section through the mid-plane of a disk. The disk has a resonant ring structure caused by an Earth-mass planet whose location is marked with a white dot. We scaled the disk density so that $\eta_0 \approx 3.7$. The top-right panel shows the surface density of the same cross-section for comparison.

The collision rate is high in a circumstellar ring near the location of the parent bodies ($\sim$3 AU), i.e., the birth ring. Grains in this region of the disk are too young to have been destroyed by collisions, so the local density is relatively high, as seen in the top-right panel. The collision rate drops just interior to this ring, at a circumstellar distance of $\sim$2 AU.

As you might expect, the top-left panel of Figure 4.6 shows that the collision rate reaches its highest point in the resonant ring structure, where the density is

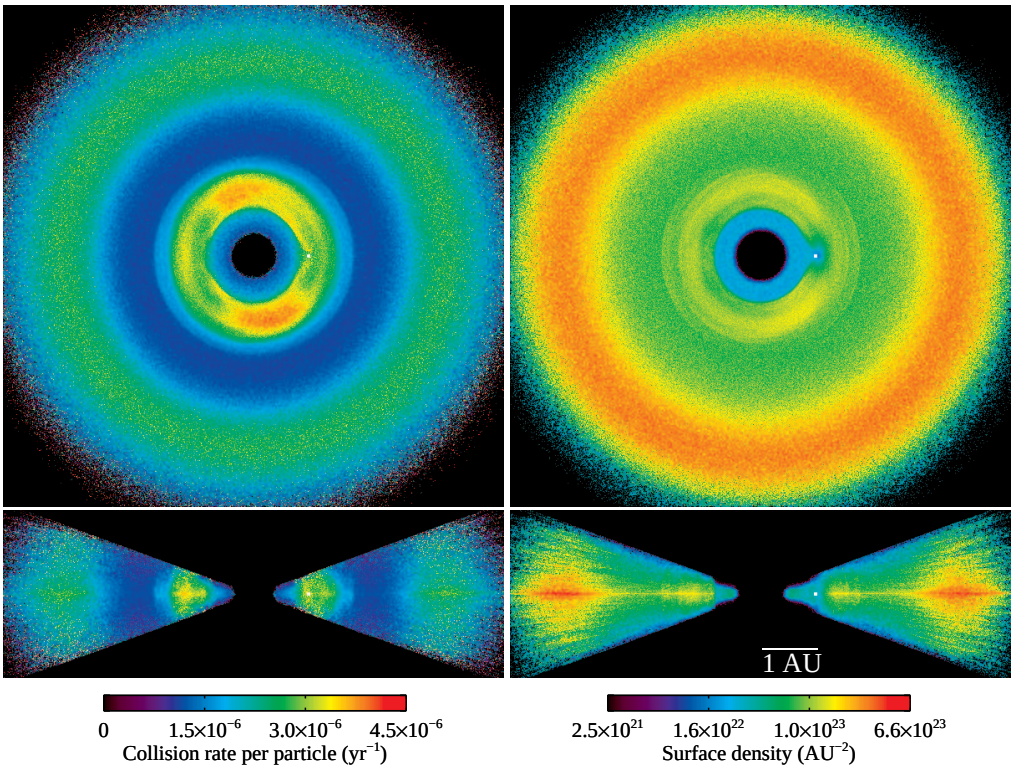

Figure 4.6: *Top-left:* Collision rate per particle ($|dN/Ndt|$) in a 0.4 AU-thick cross-section through the midplane of a disk with a resonant ring structure. A white dot marks the location of an Earth-mass planet orbiting at 1 AU. *Top-right:* Surface density of the midplane cross-section shown in the upper-left panel. *Bottom-left:* Collision rate per particle in a 0.4 AU-thick edge-on cross-section of the same disk. *Bottom-right:* Surface density of the edge-on cross-section shown in the bottom-left panel. The collision rate is affected by both the local density structure and the local velocity distribution; the collision rate is highest in the resonant ring structure, a region of enhanced density and relative particle velocities.

enhanced by resonant trapping and relative velocities are higher because of resonant pumping of the grains' eccentricities. The average collision rate in the resonant ring structure is higher by a factor of a few when compared to the collision rate exterior to the resonant ring structure, consistent with analytic estimates (Queck et al., 2007). Figure 4.6 also shows that the collision rate exhibits azimuthal and radial structure in the resonant ring. This structure reflects both localized density enhancements and regions of higher velocity dispersion. For example, the region of enhanced collision rate located $\sim 90^{\circ}$ clockwise from the planet generally corresponds to a region of higher density. But the region of enhanced collision rate located $\sim 90^{\circ}$ counterclockwise from the planet does not. This second region of enhanced collision rate is primarily caused by an increase in the local velocity dispersion, as shown in Figure 4.1.

We show the collision rate and surface density for an edge-on cross-section of the same disk in the bottom two panels of Figure 4.6. The bottom-left panel reveals a trend toward higher collision rates in the disk mid-plane, which is denser than the rest of the disk, as shown in the bottom-right panel. The bottom-left panel of Figure 4.6 also shows that the collision rate at a circumstellar distance of ~ 0.7 AU is higher than the collision rate at ~ 2 AU by a factor of ~ 2, even though the density is higher near ~ 2 AU. This increase in the collision rate occurs because grains that survive and spiral inward past the resonant ring structure have typically had their eccentricities pumped up by passage through the resonance, so the velocity dispersion interior to the resonant ring structure is higher than the velocity dispersion exterior to the resonant ring structure.

The top panel in Figure 4.7 shows the collision rate per particle as a function of semi-major axis in the region of the resonant ring, a kind of continuum with spikes. The continuum of the collision rate is higher for semi-major axis values close to 1 AU than for larger semi-major axis values because the resonant ring enhances the local collision rate by a factor of ~ 2, as shown in Figure 4.6. The spikes in the collision rate correspond to MMRs: the 2:1, 5:3, 3:2, 7:5, 4:3, 9:7, 5:4, etc., from right to left. Most of the first order resonances (p+1:p) show a split peak, with higher collision rates at the edges of the resonance than at the center. The split peaks may be caused by collisions between the grains just outside of the MMRs with the grains in the MMRs.

The dashed line in the top panel of Figure 4.7 shows the classically-calculated collision rate, $1/t_{\rm coll} = \alpha\tau/t_{\rm orbit}$. We set $\alpha = 15.8$ so that the median collision rates were equal. This value of α is larger than the estimate $\alpha \approx 4\pi$ by Wyatt et al. (1999), and hence our collision rate is higher, likely because Wyatt et al. (1999) assumes the mean relative velocity is determined solely by the range of orbital inclinations, whereas in a resonant ring the large range of orbital eccentricities will also contribute to the relative velocities.

Our algorithm shows how the classically-calculated collision rate fails for disks with planets, since this approximation neglects collisional enhancement of particles in resonance. It also cannot correctly reproduce the vertical structure of the collision rate, like that shown in the bottom-left panel of Figure 4.6. The failure of this approximation is even more dramatic than these figures show because the particles spend most of their time in the MMRs.

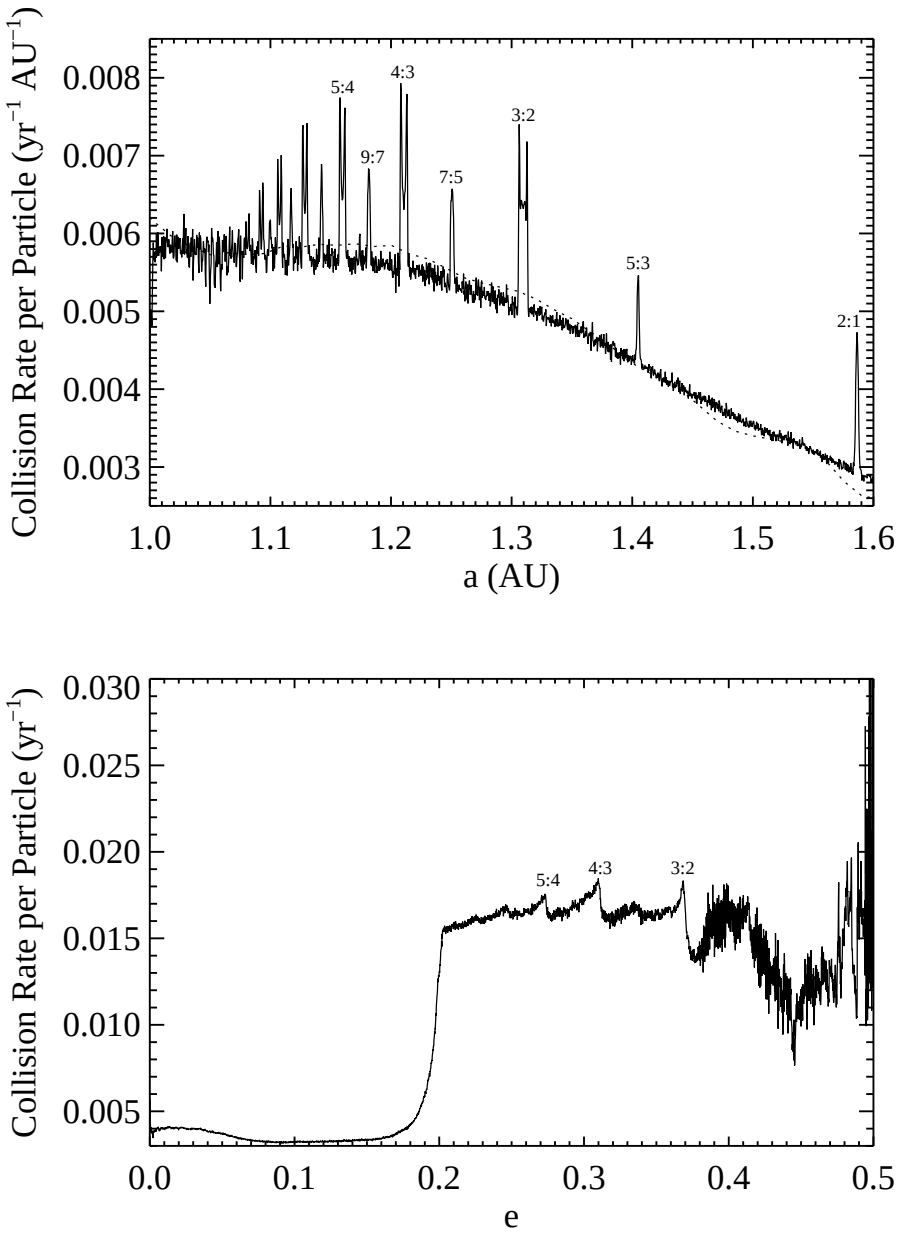

Figure 4.7: Collision rate per particle ($|dN/Ndt|$) as a function of semi-major axis and eccentricity for a disk with a resonant ring structure. The spikes in the collision rate vs semi-major axis and eccentricity show that the collision rate is enhanced for particles in resonance, and also adjacent to the first order MMRs.

The bottom panel of Figure 4.7 shows the collision rate per particle as a function of eccentricity. The particles attain an eccentricity of no more than $e \approx 0.2$ when they are launched. So any particles with $e > 0.2$ in this plot must have had their eccentricities increased by resonant pumping or close encounters with the planet. These particles have higher collision rates because they are typically located in the resonant ring, a region of higher density and larger velocity dispersion. The small peaks in the collision rate at $e = 0.27$, $e = 0.31$, and $e = 0.37$ correspond to the maximum eccentricities that particles can obtain in the 5:4, 4:3, and 3:2 exterior MMRs (Beaugé & Ferraz-Mello, 1994), and also correspond to localized regions of higher density within the resonant ring structure. The data become noisy for $e > 0.38$ because relatively few particles end up with such large eccentricities, except in close encounters with the planet.

Figure 4.8 illustrates some of the morphological effects collisions can have on resonant ring structures. The top row shows surface density histograms of a disk with a resonant ring structure for three different values of η_0, increasing from left to right. The bottom row shows zoomed-in views of the resonant ring structures from each of the disks in the top row. Each of the six histogram images was scaled independently to highlight differences in geometry.

Collisions de-emphasize the resonant ring and emphasize the birth ring. They also change the morphology of the resonant ring. In the collisionless case on the left, the resonant ring structure has a sharp inner edge with well-defined azimuthal and radial structure. For the slightly collisional system ($\eta_0 \sim 0.09$), shown in the middle, the density at the resonant ring's inner edge is significantly reduced relative

to the rest of the ring structure. As we further increase the overall collision rate in the disk, the density of the inner edge of the resonant ring continues to drop relative to the rest of the ring, while azimuthal structures in the ring become smeared out.

Collisions reduce the density of the inner edge of the resonant ring for two reasons. First, as previously shown, collision rates are higher in regions of higher density. Second, grains that contribute to the inner edge of the resonant ring are typically older, having had their eccentricities pumped up while in resonance. These older grains have had more time to collide with other grains.

4.4 Particle fragmentation

Our algorithm, as described above, can handle seed models with multiple grain sizes with no modifications. With a small modification the algorithm can also model fragmentation, i.e., collisions that produce daughter particles. Here we describe a method for including particle fragmentation and present some preliminary results.

When two particles collide and produce fragments, the fragments are launched into new orbits such that the fragment velocity vectors are distributed around the center of momentum velocity vector of the colliding particles (e.g. Krivov et al., 2005). Integrating the orbits of all of these fragments would be computationally prohibitive, so we make a numerical approximation: we limit the trajectories of the fragments we model to the recorded trajectories that already exist in the seed model. To make this approximation work, our seed model must include a sufficiently wide range of initial conditions to ensure that trajectories are available that closely match

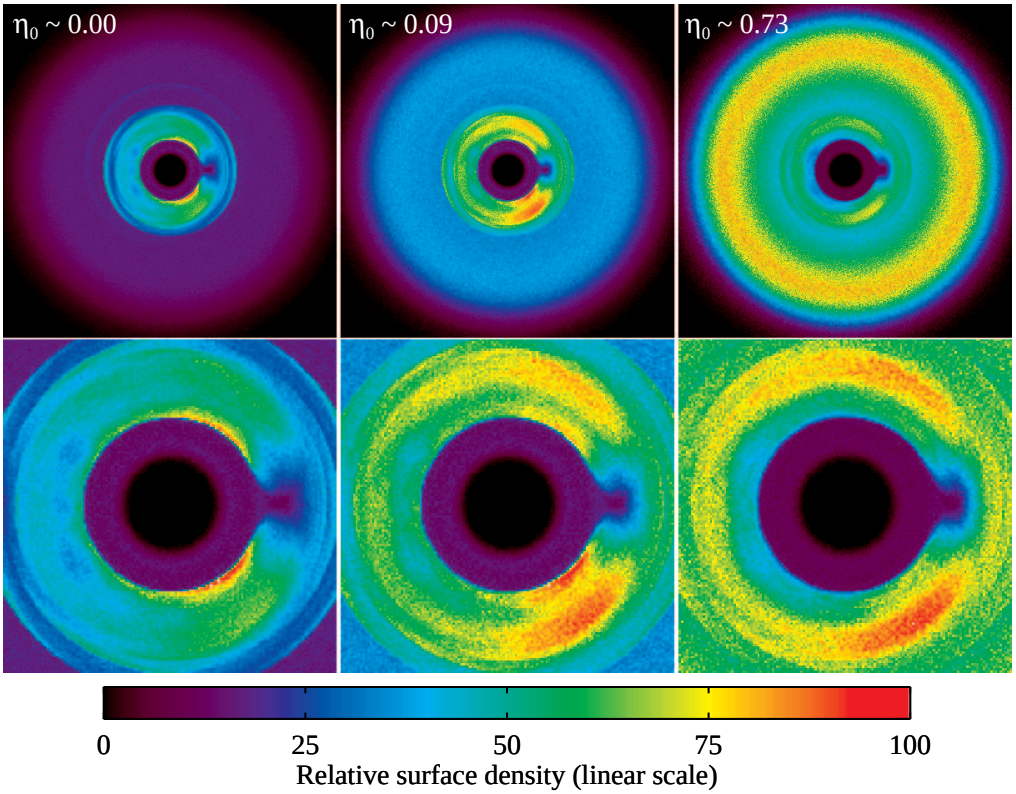

Figure 4.8: Surface density as a function of η_0 for a disk with a ring structure caused by an Earth-mass planet at 1 AU viewed face-on. The top row shows the entire disk, which extends out to 4.25 AU. The bottom row shows zoomed-in views of the resonant ring structure. Collisions reduce the sharp inner-edge feature of the resonant ring structure, smear out azimuthal structure, and de-emphasize the resonant ring while emphasizing the birth ring. Even a low collision rate ($\eta_0 \ll 1$) can significantly alter resonant ring structures.

the desired distribution of fragment trajectories.

To include particle fragmentation in our algorithm, we first run a seed model with several discrete particle sizes, each of which represents a range of sizes, and initially populate each size bin according to a mass distribution function (e.g. Dohnanyi, 1969). Then we apply our collision algorithm with the following additional subroutine, implemented during the calculation of the collision depth (Equation 4.4) for every record of each stream:

1. Calculate the k^{th} record's contribution to the collision depth of the i^{th} record (c.f. Equation 4.4), call it

$$\tau_{\text{coll},i,k} = n_k \sigma_k |\mathbf{v}_i - \mathbf{v}_k| t_{\text{record}}. \tag{4.8}$$

   Remember that the index i refers to records in a stream while the index k refers to records in a bin.

2. Calculate the mass of particles removed from the i^{th} record by collisions with the k^{th} record, given by

$$\Delta M_{i,k} = m_i N_{i-1} \left(1 - e^{-\tau_{\text{coll},i,k}}\right), \tag{4.9}$$

   where m_i is the mass of a single particle in the i^{th} record.

3. Record the center of momentum velocity vector of the colliding particles, given by

$$\mathbf{v}_{\text{COM},i,k} = \frac{m_i \mathbf{v}_i + m_k \mathbf{v}_k}{m_i + m_k}. \tag{4.10}$$

   We assume the difference between the fragment velocities and $\mathbf{v}_{\text{COM},i,k}$ is small and use $\mathbf{v}_{\text{COM},i,k}$ as the desired fragment velocity.

4. Distribute the fragments by size according to a crushing law.

5. Search within the local spatial bin for streams that closely match the grain size, s, and center of momentum velocity vector, $\mathbf{v}_{\mathrm{COM},i,k}$, of the fragments. Once the appropriate streams are found, increase the numbers of particles in those streams to account for the fragments.

The subroutine described above must be executed for every pair of records in every bin. In practice, searching for an appropriate stream in which to put fragments during every interaction is computationally expensive; the algorithm run time scales as $\langle n_{\mathrm{b}} \rangle^3$ instead of $\langle n_{\mathrm{b}} \rangle^2$. One could imagine many possible approximations that would reduce the amount of computer time spent searching for fragment streams. For our preliminary models, we chose to place all of the fragments from the i^{th} record into a single mean center of momentum stream, with velocity

$$\langle \mathbf{v}_{\mathrm{COM,i}} \rangle = \frac{\sum_k \Delta M_{i,k} \mathbf{v}_{\mathrm{COM},i,k}}{\sum_k \Delta M_{i,k}}. \tag{4.11}$$

We leave a detailed investigation into the accuracy and efficiency of this approximation for future work.

We have implemented this particle fragmentation subroutine in our code and produced a simple model of a fragmenting disk with a resonant ring structure to illustrate the procedure at work. For our seed model, we integrated the orbits of 2,500 120 μm grains ($\beta = 0.0023$) and 2,500 12 μm grains ($\beta = 0.023$) and recorded the particle positions and velocities every 426 and 42 years, respectively, as they orbited a Sun-like star (sw = 0.35) in the presence of an Earth-mass planet on

a circular orbit at 1 AU. We launched the grains from parent bodies with initial conditions identical to the second seed model described in Section 4.2.3.1. For the purposes of illustration, we initially populated only the 120 μm grain streams and implemented a simple fragmentation scenario in which 120 μm grains shatter completely into 12 μm grains, conserving mass. Fragments from 12 μm grains were deleted from the model. We assumed all colliding grains were shattered completely, regardless of the mass or velocity of the target or projectile. We scaled the number of 120 μm particles per stream such that $\eta_0 \sim 0.04$.

Figure 4.9 shows the results of our fragmenting disk model. The inset two-color image shows the face-on surface density of the disk. The 120 μm (large) grains, shown in red, dominate the surface density exterior to the resonant ring structure. The 12 μm (small) grains, shown in blue, dominate the surface density near the center of the disk.

The plot in Figure 4.9 shows the disk mass distribution as a function of semi-major axis for each of the grain sizes in our simple model. At the outer edge of the disk, near the birth ring of large grains at $\sim$4 AU, the large grains dominate the mass of the disk. As the large grains spiral inward, collisional fragmentation reduces the disk mass in large grains and transfers that mass to the small grains.

Near 1.5 AU, the resonant ring structure enhances the collision rates of the large grains and therefore also the disk mass in small grains. The spikes in the mass distribution function near 1 AU show that the two grain sizes populate different sets of MMRs. The combined effects of collisional fragmentation and PR drag would cause the resonant ring structure, and the disk as a whole, to look different

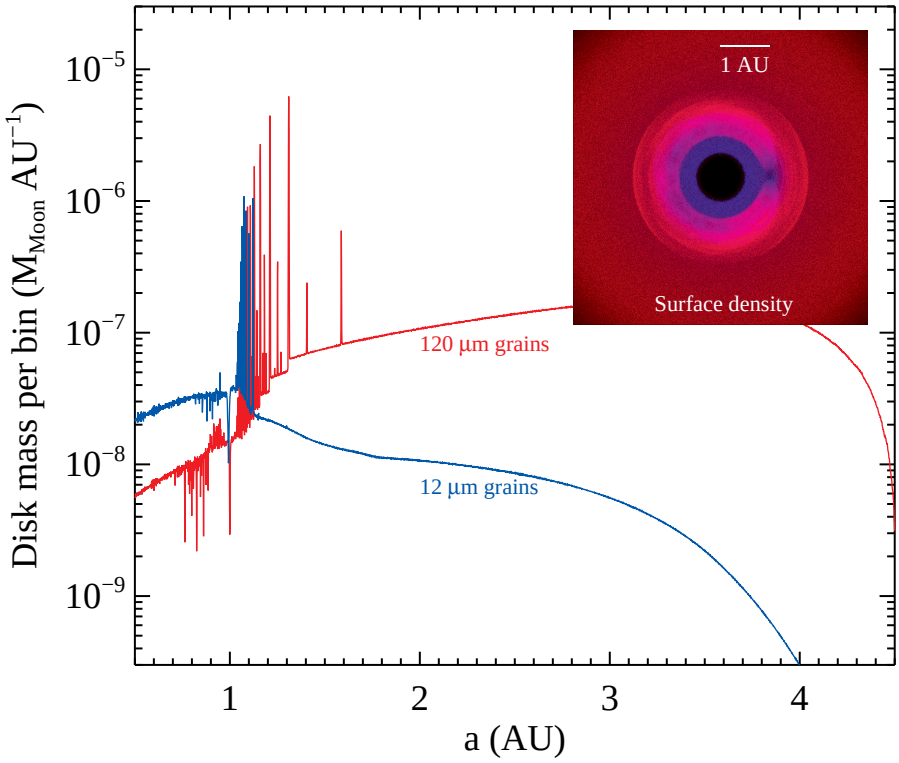

Figure 4.9: Disk mass (in Lunar masses) as a function of semi-major axis for a disk of fragmenting grains in the presence of an Earth-mass planet at 1 AU orbiting the Sun. The inset false-color image shows the face-on surface density of the disk. MMRs near 1 AU trigger fragmentation, a process which may explain the population of small warm dust interior to Fomalhaut's resolved ring structure (Stapelfeldt et al., 2004).

at different wavelengths, because grains of different sizes emit differently. Figure 4.9 shows that PR drag and resonant interactions can sort collisionally fragmenting grains by size, allowing smaller grains to spiral in to smaller circumstellar distances.

The radial distribution of dust grains produced by our model is analogous to that observed in the Fomalhaut disk. Stapelfeldt et al. (2004) resolved the Fomalhaut disk at 24, 70, and 160 μm using the Multiband Imaging Photometer for *Spitzer* (MIPS) and obtained a 17.5–34 μm spectrum with the Infrared Spectrograph (IRS). Both the IRS spectrum and the 24 μm MIPS image reveal a compact source of dust likely interior to 20 AU, well inside of Fomalhaut's outer ring structure near 140 AU. This compact source of dust, responsible for $\sim$0.7 Jy of flux at 24 μm, is not seen in the 70 or 160 μm MIPS images, suggesting that the warm dust grains are inefficient at radiating at these wavelengths; the compact warm dust grains may be smaller in size than the grains near the outer ring. Our preliminary fragmentation model shown in Figure 4.9 suggests that collisional fragmentation of large grains triggered by MMRs may be the source of small dust grains.

4.5 Summary

We have developed a new algorithm to self-consistently treat collisions and resonant gravitational dynamics in dusty disks. Our algorithm handles disks with multiple grain sizes and can be adapted to model particle fragmentation. The algorithm uses the density and velocity distributions of a collisionless disk simulation to iteratively solve for the density distribution of a steady-state collisional disk. The

algorithm is applied after the simulation of the collisionless system, removing the need to re-integrate the equations of motion for disks with different collision rates, and can run on a single processor in ~ 1 hour.

We performed several tests to show that our algorithm arrives at a unique and correct solution for collisional disks with and without a resonant ring structure. We showed that collisions can reduce the contrast of resonant ring structures, especially at the inner edge of the ring structure, and smear out azimuthal asymmetries. We also showed that particle fragmentation triggered by resonant interactions can radially sort particles by size, producing smaller particles at smaller circumstellar distances. This process may explain the population of warm dust found interior to Fomalhaut's ring (Stapelfeldt et al., 2004).

Our collisional grooming algorithm should allow us to accurately model and synthesize multi-wavelength images of observed debris disks, like Fomalhaut, Vega, and HR 4796A. The algorithm enables us to investigate the effects that collisions have on dust disk morphology, such as asymmetries from clumping of parent bodies, resonant trapping of dust grains, and the radial sorting of grain sizes illustrated in Figure 4.9. It should be useful for modeling long-lived grains in the solar zodiacal cloud and it should help us predict the morphology of ring structures in disks yet to be observed.

Chapter 5

Collisional models of the Kuiper Belt dust cloud

Submitted for publication in *The Astronomical Journal*.

5.1 Introduction

Debris disks around other stars are often described as more massive versions of the Solar System's Kuiper Belt (KB) (e.g. Greaves et al., 2004; Bryden et al., 2006; Jewitt et al., 2009; Booth et al., 2009). Debris disks, like the disks around Fomalhaut, Vega, ϵ Eridani, etc. can only be imaged if they have optical depths of $\sim 10^{-4}$ or higher with existing techniques. Models of KB dust production informed by dust detectors in the outer Solar System suggest a face-on optical depth of more like 10^{-7} for the Kuiper Belt (Backman et al., 1995; Stern, 1996; Yamamoto & Mukai, 1998). But perhaps when the Kuiper Belt was younger and more massive, it closely resembled the debris disks we have seen so far around other stars.

This analogy has many ramifications. For example, images of debris disks around nearby stars show rings, clumps, warps and other asymmetries; these asymmetries have often been compared to the asymmetries in the Kuiper Belt, caused by dynamical perturbations from Neptune and other planets. When we see these patterns in debris disks, can we recognize the planets that are sculpting them? Can we use the patterns to find hidden planets that we couldn't otherwise detect, or

measure the orbital parameters of planets orbiting too slowly to track? The Kuiper Belt, because of its proximity to the Earth, is potentially an important laboratory for testing our dynamical models of debris disks and our ideas about debris disk morphologies.

Several authors have made dynamical models of the distribution of dust in the Kuiper Belt for comparison with images of other debris disks. Liou & Zook (1999) showed that Neptune may temporarily trap dust in MMRs, forming a wide circumsolar ring, from 35–50 AU, with a gap in the ring at the location of Neptune. This model has often been compared to the wide, clumpy rings seen around Epsilon Eridani and Vega. Moro-Martín & Malhotra (2002) explored how grains of various sizes behave in the outer Solar System, and predicted the spectral energy distribution of the Kuiper Belt dust (see also Moro-Martin & Malhotra, 2003). Holmes et al. (2003) explored how a particular family of Kuiper Belt Objects (KBOs), the plutinos, could contribute to the resonant Kuiper Belt dust population.

But these models contain an important limitation: they largely neglect grain-grain collisions. In some debris disks the typical collision time can become shorter than the typical PR time, affecting the disk morphology (e.g. Wyatt, 2005); we find that this effect sets in at even lower optical depths than previously anticipated. Moreover, as we mentioned above, the debris disks we see around other stars are much more massive than the KB, making collisions even more important.

In this paper, we take a step toward a better understanding of the analogy between the KB and extrasolar debris disks. We use our new "collisional groming" algorithm (Stark & Kuchner, 2009) to explore the effects of grain-grain collisions on

the distribution of Kuiper Belt dust. We break the KB source population into three populations: hot, cold and plutinos. We model the effects of grain-grain collisions in today's KB, and we model how the KB dust morphology would change as the amount of dust is increased from a face-on optical depth of $\sim 10^{-7}$ to $\sim 10^{-4}$.

5.2 Numerical techniques: collisional grooming

Here is a brief summary of the collision grooming algorithm; Stark & Kuchner (2009) described the algorithm in depth and various numerical tests it has passed. First the orbits of a set of dust grains are numerically integrated using an n-body integrator, and the positions and velocities of the particles are recorded periodically in a histogram. We call this histogram the "seed" model. Then the trajectories of each particle are re-interpreted as steady state streams of particles, with weights that define the number of particles in each stream at any given point along the trajectory. The weights are then iteratively manipulated so that they describe a self-consistent cloud of interacting particles. The result is a 3-D grid that contains the number density of the cloud, a self-consistent solution to both the dynamical equations that govern the particle trajectories and the number flux equation that accounts for the creation and destruction of particles in every histogram bin.

There have been several recent papers on kinetic treatments of collisions in debris disks (e.g. Krivov et al., 2006; Wyatt et al., 2007) including the Kuiper Belt (Krivov et al., 2005). Some of these models involve more detailed collision physics than our simulations, e.g., time evolution and fragmentation. But our simulations

have the unique capability to explore the interaction between the dynamical effects of planets, e.g. resonances, secular forcing, etc., and grain-grain collisions. These pheneomena turn out out be crucial for understanding the distribution of dust in debris disks, even in the presence of collisions, as we will show.

To create the seed model for our study, we integrated the equations of motion for a particle subject to gravity from the Sun, Jupiter, Saturn, Uranus, and Neptune plus radiation pressure, Poynting-Robertson (PR) drag and solar wind drag (see Stark & Kuchner, 2008). We used a customized hybrid symplectic integrator, described in Stark & Kuchner (2008), modified to include drag forces. The integrations all used a symplectic time step of 0.1747 years, equal to $\sim 1/20$th of the orbital period at 2.5 AU. We ran the integrations on NASA's Discover cluster (http://www.nccs.nasa.gov/discover_front.html). We recorded the seed model in the frame rotating with the mean motion of Neptune, to capture any resonant structures associated with that frame (see Kuchner & Holman, 2003, for a discussion of which structures are associated with which frame).

We integrated the orbits of all particles for 5×10^8 years, a few times the maximum collision time for the simulation with lowest optical depth we considered. We removed particles once they reached a semi-major axis $a < 2.5$ AU, or $a > 300$ AU, or suffered a collision with a planet, assuming realistic planet radii. The time between records was chosen individually for each particle size bin, such that each size bin contributed roughly 4×10^6 records for each of the three source populations (see below). We accumulated the particle records in a histogram of $512 \times 512 \times 128$ bins, each with size $0.5 \times 0.5 \times 0.3$ AU. We ran the collisional grooming algorithm

for as many iterations as it took until none of the weighting factors varied by more than 10% from one iteration to the next. This part of the simulation took only a couple of hours on a single processor, but required 20 gigabytes of of RAM.

Moro-Martín & Malhotra (2002) pointed out that with too few particles, it is possible that 1) the MMRs may not be populated accurately, and that 2) a few unusually long-lived grains can dominate the simulations. We overcome these sources of noise as we did in Stark & Kuchner (2008) and Stark & Kuchner (2009). We ensure the MMRs are populated accurately by using a total of 75,000 particles; Moro-Martín & Malhotra (2002) had called for $\sim 10^5$. We handle long-lived particles using the collisional grooming algorithm, which includes the effects of collisions in removing these particles.

We added a new piece of physics to our simulations since Stark & Kuchner (2009). In our new models, when two dust grains collide, they only destroy each other when the energy of the collision measured in the center of mass frame exceeds the estimated binding energy of the particles, Qm_t, where m_t is the mass of the target grain. Otherwise, the particles continue unaltered. We use an estimate for the specific binding energy described in Krivov et al. (2006), the "strength" regime of Equation 22 in that paper:

$$Q = A_s \left(\frac{s}{1 \text{ m}} \right)^{b_s} \tag{5.1}$$

The radius of the dust grain is s. We take $A_s = 2 \times 10^5$ erg g^{-1} and $b_s = -0.24$, the values Krivov et al. (2006) used for "icy" grains. Throughout this paper, we assume spherical particles with a density of $\rho = 1$ g cm^{-3}.

For the sake of numerical simplicity in this first generation of 3-D multi-grain-size collisional models, we do not explicitly follow any fragments produced in the collisions; we assume that all dust production arises in the source populations, described below. In any case, samples of cometary particles directly returned from the Stardust mission (Brownlee et al., 2006; Zolensky et al., 2006) and observations of cometary ejecta during the Deep Impact mission (A'Hearn et al., 2005) reveal that the majority of observed cometary particles are loosely bound aggregates of submicron-sized grains, which can easily be shattered into unbound β-meteoroids. These samples seem likely to represent KB particles too.

5.3 Source populations

In the models described here, there are two kinds of bodies: the dust grains, and the source bodies. The dust grains have orbits that evolve via drag and radiation pressure; they can be destroyed in collisions with each other. The source bodies have fixed orbits, and steadily produce the dust grains; they model bodies too large to be destroyed in collisions, but which nonetheless release dust, e.g., via collisions that are not part of the bookkeeping.

The dust grains contribute most of the optical depth, so we focus mostly on their dynamics. The large bodies are incorporated into the simulations as the initial conditions of the grains in the seed model. The models ultimately depict a steady-state flow of grains; "initial" here refers only to where the individual grains are launched in the seed model.

The size of a grain is approximately parametrized by β, the force on the grain from radiation pressure divided by the force from stellar gravity, given by Equation 1.3. Liou & Zook (1999) used four different β values and a total of 350 particles. Moro-Martín & Malhotra (2002) used five different β values and a total of 500–700 particles, for each of four different models. We used 25 different β values and a total of 75,000 particles. The 25 β values range from 0.00046 to 0.43355; the spacing between them is logarithmic. Since we assume perfectly absorbing spherical particles with a density of $\rho = 1$ g cm^{-3}, $\beta = 0.57$ μm$/s$, whre s is the dust grain radius. With this assumption, the range of sizes in our initial conditions corresponds to 1239 to 1.3 μm.

The grains were launched with a size distribution $dN/ds = s^{-3.5}$, where s is the radius of the grain. This distribution is the "crushing law" telling us the relative production rate of grains of various sizes. We discuss how collisional processing alters this size distribution below.

Our study benefits from the recent explosion in KBO surveys. Our simulations incorporated three different populations of source bodies, representing three different populations of KBOs. We relied on the models of Kavelaars et al. (2008) and Kavelaars et al. (2009) to disentangle these populations in the face of the many observational biases that affect measurements of KBO populations (see also Brown, 2001; Trujillo & Brown, 2001). The source populations we assume are as follows:

- **Cold.** This source population represents the cold classical Kuiper Belt (Brown, 2001). The semi-major axes, a, for this population were distributed uniformly

between 42.5 and 45 AU. The eccentricities, e, were distributed uniformly between 0 and 0.1. The inclinations, i, were distributed with distribution $P(i) \propto \exp(-0.5(i/\sigma_C)^2)$ where $\sigma_C = 1.5°$. The longitudes of ascending nodes and arguments of perihelia were distributed uniformly over $[0, 2\pi)$. This component makes up 16.3 % of the total source population.

- **Hot.** This population represents both the hot population of the classical KBOs and the scattered/detatched Kuiper Belt. The semi-major axes are distributed uniformly between 35 and 50 AU, and the eccentricities are distributed such that $P(e) \propto e$, subject to the additional criterion that $a(1-e) > 35$ AU. Because of this additional criterion, the semi-major axis distribution ends up weighted toward 50 AU. The inclinations are distributed with $P(i) \propto \exp(-0.5(i/\sigma_H)^2)$ where $\sigma_H = 13°$. The longitudes of ascending nodes and arguments of perihelia were distributed uniformly over $[0, 2\pi)$. The dominance of this category of object in the KB has only recently become apparent; we assume it makes up 79.7 % of the total source population.

- **Plutinos.** To represent these bodies, we chose the orbits for the source bodies from a list of orbits for actual KBOs on the Minor Planet Center's web site with $39.1 < a < 39.7$ AU. We assume that this population makes up 4% of the total source population.

Figure 5.1 illustrates these three assumed source populations. We assigned 25,000 particles to each of them. For comparison, Liou & Zook (1999) assumed that all of their source bodies were in orbits with semi-major axes 45 or 50 AU. Moro-

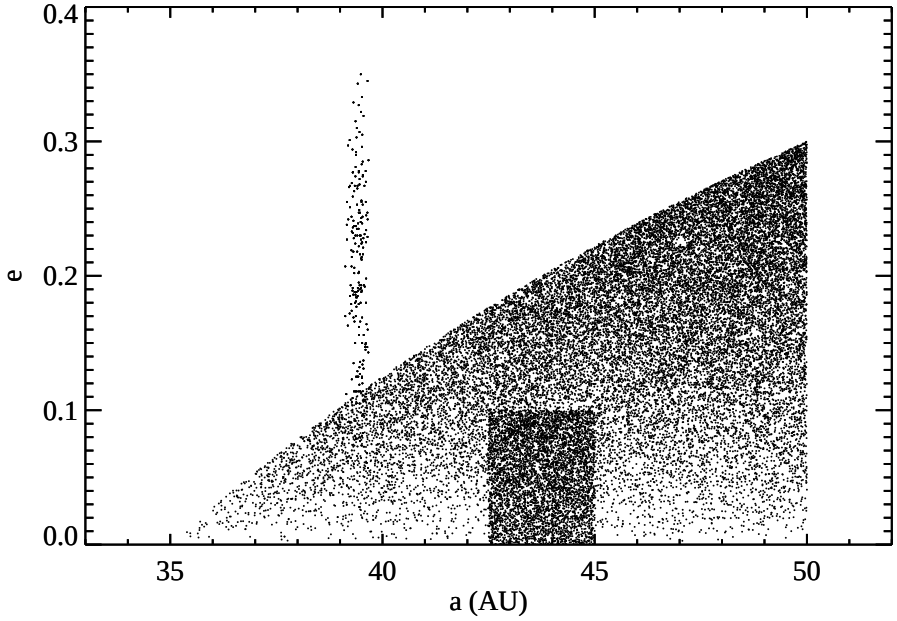

Figure 5.1: Semi-major axis and eccentricity distributions for the assumed source particles.

Martín & Malhotra (2002) assumed all source bodies had orbits with semi-major axes equal to 45 AU, or that the source body semi-major axes were distributed uniformly from 35–50 AU. Holmes et al. (2003) assumed all their source bodies had approximately Pluto-like orbits.

When the grains in our models are released, they instantly jump to new orbits because of radiation pressure, conserving their velocity at release (see Moro-Martín & Malhotra, 2002; Holmes et al., 2003). Moreover creation of particles through collisions generates some velocity dispersion (e.g. Cellino et al, 1999), though we do not attempt to explicitly model this effect. Many of the source particles have

resonant orbits, by happenstance, but except for the plutinos, we do not go out of our way to capture the detailed resonant dynamics of the KB in our source bodies (see Chiang et al., 2003). The two effects described above that instantly change the orbits of the particles on release will often wash out the resonant behavior of the source particles anyway; see Holmes et al. (2003). The KB's detailed resonant structure might serve to enhance the resonant populations of dust beyond what our models show; we leave an investigation of this effect for a future date when we understand this phenomenon better observationally.

For our basic KB model, we chose a total dust production rate of 3.6×10^6 g s^{-1} to make the face-on geometrical optical depth in the ring $\sim 10^{-7}$. This rate is consistent with estimates based on the dust fluxes measured by *Pioneer 10* and *11* beyond 10 AU from the Sun (Landgraf et al., 2002; Moro-Martin & Malhotra, 2003). We refer to this model as "KB×1". When we scale the KB up for our models referred to as KB×10, KB×100, and KB×1000, we scale the dust production rate so it increases the average optical depth in the cold component ring by 10, 100 and 1000 times.

Table 5.1 lists the typical optical depths and dust production rates, summed over all grain sizes in the model, corresponding to each of the three dust levels. The dust production rate depends on the size range of grains considered—especially the size of the largest grains considered. So the table quotes both the total dust production rate and the rate of production of grains with $s < 10$ μm, for ease of comparison with other calculations. For example, Yamamoto & Mukai (1998) estimated that the total dust production rate for particles smaller than 10 μm is

(0.37-2.4) $\times 10^6$ g s^{-1} if the objects have hard icy surfaces, or (0.85-3.1) $\times 10^7$ g s^{-1} if the objects are covered with icy particles smaller than interstellar grains. The hard icy surfaces case would correspond roughly to our KB×10 model, while the small icy particles case would be somewhere between that and our KB×100 model.

Table 5.1: Optical Depth

Model	Optical Depth	Total Dust Production Rate (g s^{-1})	Dust < 10 μm Production Rate (g s^{-1})	Critical Grain Size, s_c, (μm)[a]
1×	$\sim 10^{-7}$	3.6×10^6	2.2×10^5	17
10×	$\sim 10^{-6}$	7.5×10^7	4.6×10^6	6
100×	$\sim 10^{-5}$	2.4×10^9	1.5×10^8	3
1000×	$\sim 10^{-4}$	1.2×10^{11}	7.3×10^9	~ 1

[a]Grain size where $\langle t_{\rm coll} \rangle = \langle t_{\rm PR} \rangle$.

5.4 Results

5.4.1 Collisionless simulations

Figure 5.2 illustrates the seed model we used: a histogram representing the steady-state distribution of KB dust grains in the absence of collisions. It also shows the contributions to this seed model from each of the three source populations described above. The figure shows only a 2-D projection of the cloud density; the full seed model is a 3-D histogram, which also contains the 3-D velocity distribution at each point in the histogram. The grains of different sizes were combined together weighted to simulate a dust production rate of $dN/dsdt \propto s^{-3.5}$.

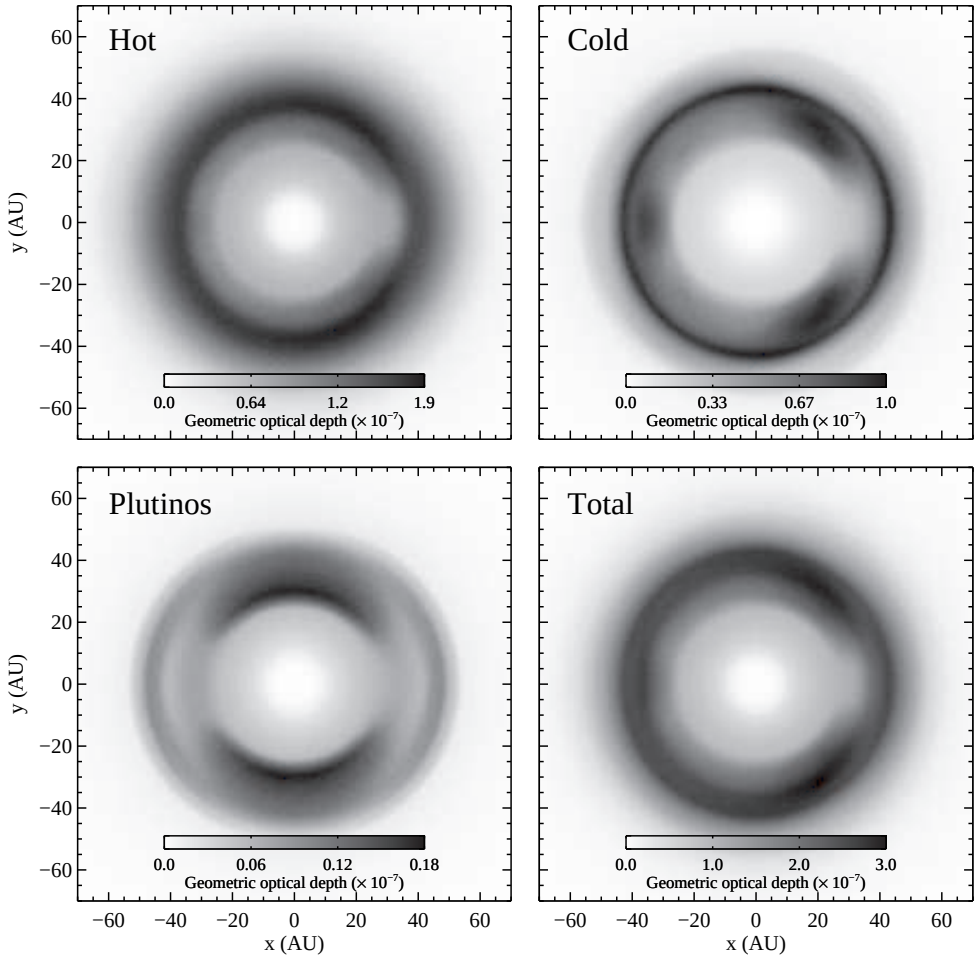

Figure 5.2: Collisionless simulations of the Kuiper Belt dust: the geometrical optical depth for each source population and for the total. Neptune is located at x=30.0696, y=0 AU.

This figure can be compared to other collisionless models of the KB dust, like those described in Liou & Zook (1999) and Moro-Martín & Malhotra (2002). Overall, the seed model morphology is a wide circumsolar ring with a gap at the location of Neptune, not dissimilar from that predicted by those authors. It also resembles the Type I resonant ring described by Kuchner & Holman (2003), the case of the low-mass planet on a circular orbit.

In this collisionless stage of the simulation, particles of all sizes participate strongly in resonant trapping, especially in the lowest-order resonances. The signature of the plutino dust is a ring of dust trapped in the 3:2 MMR with Neptune—like the plutinos themselves. Dust produced by the cold population of source bodies shows heavy signatures of several MMRs with Neptune: 3:2, 7:4, 8:5, etc., but not the 2:1, because it is released substantially interior to the 2:1. Dust produced by the hot population also participates in the MMRs, though less than the other populations because of the reduced trapping probabilities associated with higher e and i.

5.4.2 Simulations with collisions

Figure 5.3 shows the geometrical optical depth of the total KB dust population after the full collisional grooming algorithm has been applied, as described above, at four different dust levels. As the optical depth increases, collisions remove grains from the center of the disk. As Stark & Kuchner (2009) showed, the highest grain-grain collision rates occur in MMRs, so the collisions also tend to reshape and erase

the resonant structure. At the highest optical depth, the pattern mostly resembles a narrow ring, coincident with the cold classical Kuiper Belt.

The hot population still always dominates the total optical depth and semi-major axis distribution—except that the birth ring of the cold population begins to poke through at 40-45 AU as the total optical depth of the simulation is increased. The plutinos make a negligible contribution, except to the distribution of large grains.

Figures 5.4 and 5.5 show the semi-major axis distributions of the grains in the three collisional simulations, broken down into three size bins (it would be impractical to show all 25 size bins). It also shows the distributions summed over all grain sizes. To calculate the "optical depth" shown in in these figures, we took the number of grains within a certain range of semi-major axis, Δa, multiplied by the grain cross section, and divided by $2\pi a \Delta a$. The grey lines show how the distributions break down by source population. The black lines show the total in each size bin.

One phenomenon that these figures show is that small grains penetrate interior to Neptune's orbit more frequently than large grains. The result is a disk with large grains on the outside and small grains on the inside, like the disk around Fomalhaut, according to data from *Spitzer* (Stapelfeldt et al., 2004) and VLTI/VINCI (Absil et al., 2009). This phenomenon occurs even for a disk with optical depth $\sim 10^{-7}$.

Next, let us look at which grain sizes dominate the optical depth throughout the disk. At low collision rates (KB×1) the 4.7–19.7 μm particles dominate the semi-major axis distribution interior to about 50 AU. At KB×10, it's a tie between

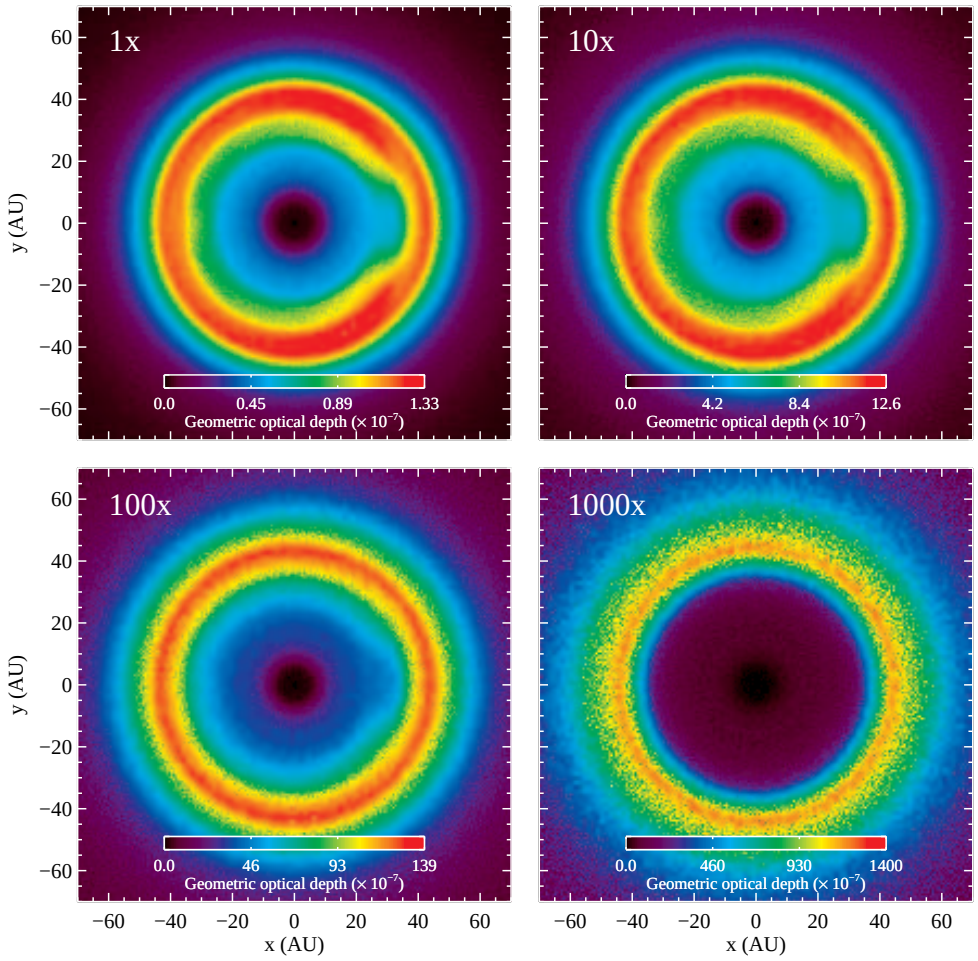

Figure 5.3: The total optical depth in our simulations of the KB dust, with grain-grain collisions. Neptune is located at x=30.0696, y=0 AU.

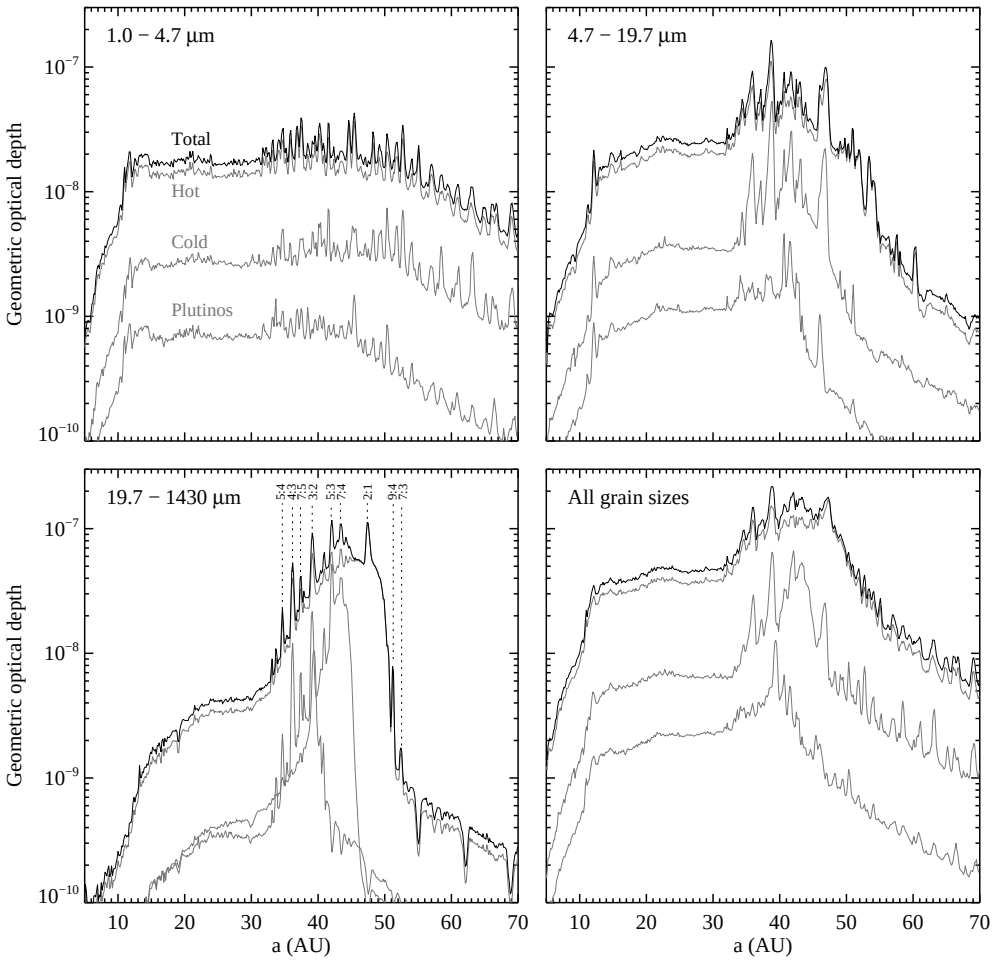

Figure 5.4: Semi-major axis distribution of particles in the KB×1 collisional simulations. Dashed lines label some mean motion resonances with Neptune in the bottom left panel.

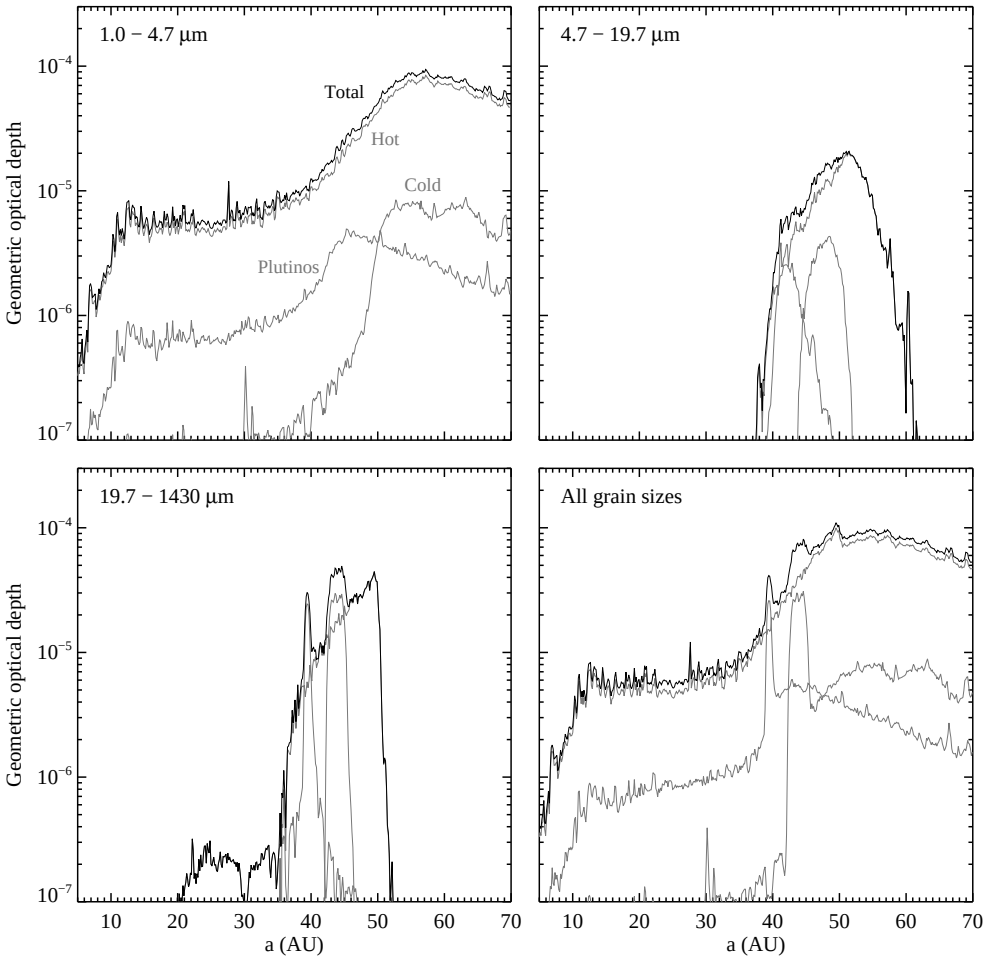

Figure 5.5: Semi-major axis distribution of particles in the KB×1000.

that bin and the smallest grains (1–4.7 μm) at $a < 50$ AU. At KB×1000, the smallest grains dominate everywhere but 35–50 AU, where the largest grains make a comparable contribution (Figure 5.5). At this high optical depth, the 4.7-19.7 μm grains make a negligible contribution.

The many fine peaks in the semi-major axis distributions of the dust grains arise mainly from dust trapped in MMRs. To read these peaks, it is helpful to remember that the mean semi-major axis in a MMR is shifted inward for dust grains by a factor of $(1 - \beta)^{1/3}$ because radiation pressure counteracts stellar gravity. For the 5 μm grains in our simulations, the inward shift amounts to about 1 AU in the KB. Over the range of 1–5 μm, the shift ranges over a factor of several AU; this probably accounts for the many fine peaks in the semi-major axis distribution of the 1–4.7 μm grains. Duplicate or split peaks in the 1–4.7 μm grain semi-major axis distributions are an artifact of the quantized grain size distribution used in the simulations.

Nonetheless, notice how the texture of the curves changes at about 30 AU. Interior to $\sim$ 30 AU, the curves in Figure 5.4 are relatively smooth. Exterior to this semi-major axis, the curves become ragged and bumpy. This texture reveals the presence and population of many Neptune MMRs, both low order (like 3:2 and 4:5) and higher order (like 8:5, 7:5, and 7:4). The opposite effect occurs in Figure 5.5. In this figure, the ragged texture, indicating MMRs, exists only interior to about 30 AU. The typical uncertainty associated with Poisson noise in these figures is less than the thickness of the line.

In the low-optical depth simulations, several MMRs stand out as having par-

ticularly strong peaks. On the left side of Figure 5.4, the small grains show a strong peak near the 3:2 MMRs with Saturn ($\sim$ 12 AU) and a secondary peak near the 2:1 (16 AU). Very few grains of any size make it interior to 10 AU; they are scattered out of the Solar System by Saturn.

A series of exterior MMRs with Neptune shows strong peaks at all grain sizes in the KB×1 model: 4:3, 3:2, 7:4, 2:1, etc. ($\sim$36, 39, 44, and 48 AU). Dashed lines show these and a few other MMRs in Figure 5.4. Some of these peaks also survive in the total semi-major axis distribution. They appear in all three source populations, though they are strongest in the cold classical population. Figure 5.3 shows that at this dust level (KB×1), the resonant structure looks like a ring at Neptune's orbit with a gap, not too dissimilar from that found by Liou & Zook (1999) and Moro-Martín & Malhotra (2002).

In the semi-major axis distribution for the KB×10 simulation (not shown), the 2:1, 3:2, 7:4, and 4:3 peaks clearly stand out in the 4.7-19.7 μm population. But those peaks become hard to pick out in the total distribution, except for 2:1 and maybe the 3:2. However, despite the fact that the first order MMRs show little contribution to the semi-major-axis distribution, the map of the optical depth at this dust level (Figure 5.3) looks again like a ring with a gap, but narrower. This pattern indicates that there still are MMRs near Neptune populated with dust. This trend continues in the KB×100 simulation; the MMR peaks become still weaker, and the ring becomes more azimuthally-symmetric.

Figure 5.5 shows that the peaks in the MMRs vanish beyond $\sim$ 30 AU; grain-grain collisions have removed almost all of the grains from Neptune's resonances.

The resonant signatures that persist in the Kuiper Belt region are only the initial conditions of the plutinos. The small grains in the interior of the disk also appear to be trapped in MMRs with Saturn.

5.4.3 Grain size distributions

Figure 5.6 shows the steady-state size distributions of particles, dN/ds, in our Kuiper Belt simulations, integrated over the whole cloud. Black curves show the size distributions for simulations of 1×, 10×, 100×, and 1000× the Kuiper Belt. A grey line shows a power law of $s^{-3.5}$, representing both the crushing law we used, and the Dohnanyi (1969) collisional equilibrium power law. Another grey line shows a simulation with no collisions, scaled to yield an optical depth in the Kuiper Belt similar to that of the KB×1000 collisional simulation.

Moro-Martín & Malhotra (2002) and Stark & Kuchner (2008) weighted the contributions from grains of different sizes to match prescribed power law distributions in their models. The collisional grooming algorithm does not require any such tuning. The grains are released according to a crushing law, mentioned above, and the collisional grooming algorithm calculates, self-consistently, the size distribution of the particles in every histogram bin. The only free parameter is the relative number of grains of each size that is released by the particle sources.

Figure 5.6 shows that in the absence of collisional processing, the slope of the steady-state size distribution becomes shallower than the $s^{-3.5}$ crushing law we assumed. This shallower slope represents two effects, described in Stark & Kuchner

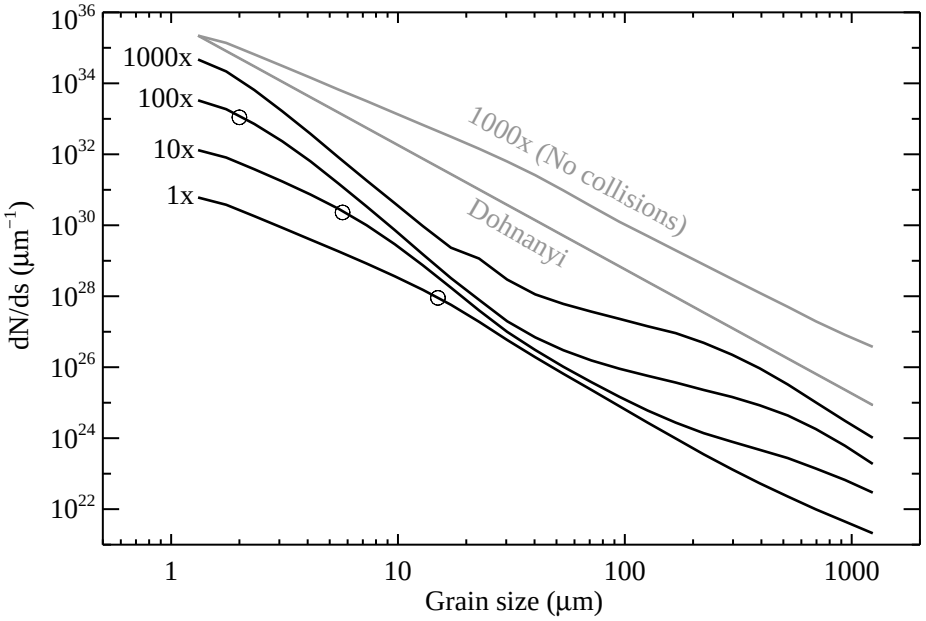

Figure 5.6: The number of grains per size interval as a function of grain size in our simulations. Black lines show collisional simulations with 1×, 10×, 100×, and 1000× the optical depth of the Kuiper Belt. Grey lines show the collisionless simulation (×1000) and a power law of $s^{-3.5}$ (Dohnanyi, 1969) for comparison. Circles indicate the critical grain size, s_c, for each simulation, as listed in Table 5.1.

(2008). First of all, the PR time is proportional to s, so in the absence of planets or collisions, the size distribution would become $s^{-2.5}$. Second, larger grains are more likely to be trapped in MMRs with planets, which prolong their lifetimes.

When the collisions are turned on, however, the size distribution relaxes to something closer to $s^{-3.5}$. The average slope of the size distributions for the collisional models is -3.5, as you can tell from looking at the endpoints of the black curves. The curves for the collisional models also contain dips in the mid-sized grain populations. The dips become deeper as the optical depth increases.

5.4.4 A critical grain size and a crossover optical depth

Stark & Kuchner (2008) hypothesized that in the absence of a resonant source population, grains with a PR time, $t_{\rm PR}$, equal to their collision time, $t_{\rm coll}$, would dominate the optical depth of a resonant ring. Our new simulations seem to roughly confirm this hypothesis. We let s_c identify the critical grain size at which $t_{\rm PR} = t_{\rm coll}$. Table 5.1 shows s_c in each simulation, averaged over the KB.

We can estimate s_c if we approximate the collision time using Equation 1.5 and the PR time using Equation 1.4. Setting $t_{\rm PR} = t_{\rm coll}$, we find that

$$s_c \approx 3L_\star Q_{\rm PR}/(8\pi c^2 \rho \tau G^{1/2} M_\star^{1/2} a^{1/2}) \tag{5.2}$$

$$= 1145\ \mu\text{m}\ \mathrm{Q_{PR}} \left(\frac{\rho}{1\ \mathrm{g\ cm^{-1}}}\right)^{-1} \left(\frac{\mathrm{L_\star}}{\mathrm{L_\odot}}\right) \left(\frac{\mathrm{M_\star}}{\mathrm{M_\odot}}\right)^{-1/2} \left(\frac{\mathrm{a}}{1\ \mathrm{AU}}\right)^{-1/2} \left(\frac{\tau}{10^{-7}}\right)^{-1} \tag{5.3}$$

In our simulations of the KB, this expression seems to overestimate s_c by a factor of 1–10, as you can tell from Table 5.1, mostly because the collision time is shorter for grains in MMRs. The degree of overestimation is highest at low optical depths,

where resonant trapping is the strongest.

Overall, the semi-major axis distributions of the grains reveal three kinds of behavior among the various grain sizes. The smallest grains participate relatively little in the resonant trapping; their radial distribution tends to resemble the solutions to the one-dimensional mass flux equation in Wyatt (2005). The largest grains have such large PR times that they tend to be destroyed by collisions before they evolve far from the source particle orbits where they are released. Grains of intermediate sizes, where the PR time, $t_{\rm PR}$, is comparable to the collision time, $t_{\rm coll}$, dominate the resonant peaks in Figure 5.4.

In our collisional grooming calculations we tend to find two different extremes of disk structure: disks dominated by rings of dust transported by PR drag and temporarily trapped in resonances (e.g. KB×1), and disks whose appearance is dominated by the distribution of source particles (e.g. KB×1000). In our simulations using a single particle size (Stark & Kuchner, 2009), we found that the transition between these regimes occurred when the collision time became roughly equal to the PR time, i.e. $s \sim s_c$. In these new simulations where the particles span a wide range of sizes, we find that the PR-drag dominated regime persists at some level as long as there are *any* particles in the size spectrum with $s \sim s_c$.

So our new simulations prompt us to write down a new criterion for when the resonant rings start to dominate: a crossover optical depth. For $\tau \lesssim \tau_r$, PR-drag and resonant trapping of small grains dominates the geometrical optical depth of the disk; for $\tau \gtrsim \tau_r$, the source population dominates. The source population may be resonant as well—but it is not trapped into resonances by PR drag. The crossover

optical depth, τ_r, is set by the criterion that all particles must survive both collisions and radiation pressure blowout.

To find τ_r, we can set $\beta = 1/2$ in Equation 1.3 to find the blowout size, $s_{\rm blowout}$:

$$s_{\rm blowout} = \frac{3L_\star Q_{\rm PR}}{8\pi G M_\star c \rho}. \tag{5.4}$$

Then, we set $s_c = s_{\rm blowout}$, when $\tau = \tau_r$. We find that τ_r is simply the orbital velocity divided by the speed of light:

$$\tau_r \approx v/c. \tag{5.5}$$

This result suggests that in a given disk, the birth ring will dominate the optical depth in the outskirts of the disk. E.g., the Kuiper Belt $\tau_r \sim 10^{-6}$. Resonant structures are apt to dominate the optical depth in the center of a disk, e.g., the habitable zone, where $\tau_r \sim 10^{-4}$.

For the simulations described in this paper, we chose τ in the KB region, and allowed the simulation to determine how the dust flowed elsewhere. The result is that the birth ring dominates the KB region for the KB×100 and KB×1000 simulations. In these regions, $\tau \gtrsim \tau_r$. But the region near Saturn remains at $\tau < 10^{-5}$ even as we turn up the dust production rate. The critical optical depth near Saturn is $\tau_r \sim 3 \times 10^{-5}$, so near Saturn, the resonant structure dominates.

5.4.5 Observable phenomena

We synthesized images from our multi-grain size collisional models at various wavelengths to illustrate what they would look like to various telescopes. To create these images, we illuminated the grains with solar flux appropriate to their

distance from the star, and calculated the scattered light and thermal emission. We assumed isotropic scattering, an albedo of unity, and simple generic emissivity laws to account for the poor ability of grains to radiate and absorb photons with wavelengths larger than the grain size: emissivity $\epsilon = 1$ for wavelengths $\lambda \leq 2\pi s$ and $\epsilon = (2\pi s/\lambda)^2$ for $\lambda > 2\pi s$ (Backman & Paresce, 1993). We used the tools in ZODIPIC (Moran et al., 2004) to self-consistently calculate the temperatures of the grains, given solar radiation and the emissivities above. For the KB×1000 images, and also for KB×100 scattered light image, we rebinned the simulations by a factor of two in each direction, to average down the Poission noise in the histograms, which increases for short collision times, as collisions remove the small grains. We did not model the point spread function of any telescope.

Figure 5.7 shows images of the four collisional models in scattered light (0.6 μm). Figure 5.8 shows the KB×1 and KB×1000 simulations as they would appear in the submillimeter (800 μm). The optical images emphasize the center of the cloud, which is better illuminated by sunlight. They also emphasize the small particles, particularly those with $t_{\rm PR} \sim t_{\rm coll}$, which tend to participate most strongly in resonances with planets.

The submillimeter images tell a different story. The submillimeter radiation comes mostly from the large grains ($\gtrsim$ 100 μm in size), which do not venture far from their initial conditions, even in the model with optical depth 10^{-7}. The submillimeter images mostly trace the distribution of source particles. Figure 5.8 shows that an observer looking at the KB dust ×1000 from a nearby star at submillimeter wavelengths would probably see a narrow ring of large grains at 42-45 AU. This ring

consists of large grains > 100 μm in size associated mostly with the cold classical Kuiper Belt.

An observer looking at the KB dust $\times 1000$ in visible light would mostly see a wide ring at 7-13 AU. We can see from Figure 5.5 that this ring consists mostly of grains with $s \leq s_c$, trapped in the 2:1, 3:2, and other MMRs with Saturn, with an optical depth of $\sim 10^{-6}$. There may be azimuthal structure associated with Saturn, but since we recorded the data in the frame rotating with Neptune's mean motion, any such structure has been smeared into a ring.

Figure 5.7 shows that at lower dust production rates, the above features persist, and a new component appears at optical wavelengths: a ring of dust in Neptune's orbit. This ring corresponds to the ring modeled by Liou & Zook (1999); it has a gap at Neptune's location—indicating the current position of the planet. We know from Figures 5.4 and 5.5 that this dust consists of two size ranges: large grains originating from plutino parent bodies in Neptune's 3:2 MMR, and smaller grains with $s \sim s_c$, released outside resonance, and then trapped in MMRs. The KB$\times$100 and KB$\times$1000 panels in Figure 5.7 illustrate the kind of morphological transformation that occurs when $\tau \sim \tau_r$ (roughly at an optical depth of 10^{-6} in the Kuiper Belt).

Neptune's azimuthally-asymmetric resonant ring never becomes visible at sub-millimeter wavelengths, however, at any dust level. Except for the increased numerical noise in the KB$\times$1000 simulations, the two images in Figure 5.8 are identical. The stark azimuthal symmetry of our KB shown in our simulations contradicts suggestions by previous authors. Indeed, Figure 5.8 suggests that it would be impossible to recognize evidence of a Neptune-like planet in a dust cloud similar to

the KB dust at submillimeter wavelengths.

Though the geometrical optical depth of the KB×1 ring may look similar to the collisionless simulations, the submillimeter image of the KB×1 does not. The new simulations show how collisions play an important role in determining the structure of the dust in today's Kuiper Belt; they determine the size range of particles that will dominate the images.

5.5 Discussion

5.5.1 Resonant rings and clumps

Several authors have tried to understand exactly how important MMRs can be in sculpting the shapes of disks. E.g., how clumpy can exozodiacal clouds be, and how will this clumpiness impact searches for extrasolar Earth-like planets (e.g. Roberge et al., 2009)? Do the clumps we see in millimeter and sumillimeter images of debris disks necessarily point to planets (e.g. Wilner et al., 2002)? Our simulations shine some light on this problem.

For example, Krivov et al. (2007) divided resonant effects in debris disk dust into two categories: large grains released from source populations that are in MMRs, and small grains that become trapped in MMRs. Our simulations reveal both of these effects. Krivov et al. (2007) estimated that clumps created by small bodies in resonance would persist only at optical depths $\lesssim 10^{-4}$; at higher optical depths, they would be replaced by a narrow symmetric ring. Our simulations roughly confirm this prediction; the clumps created by small dust grains in our simulation fade into

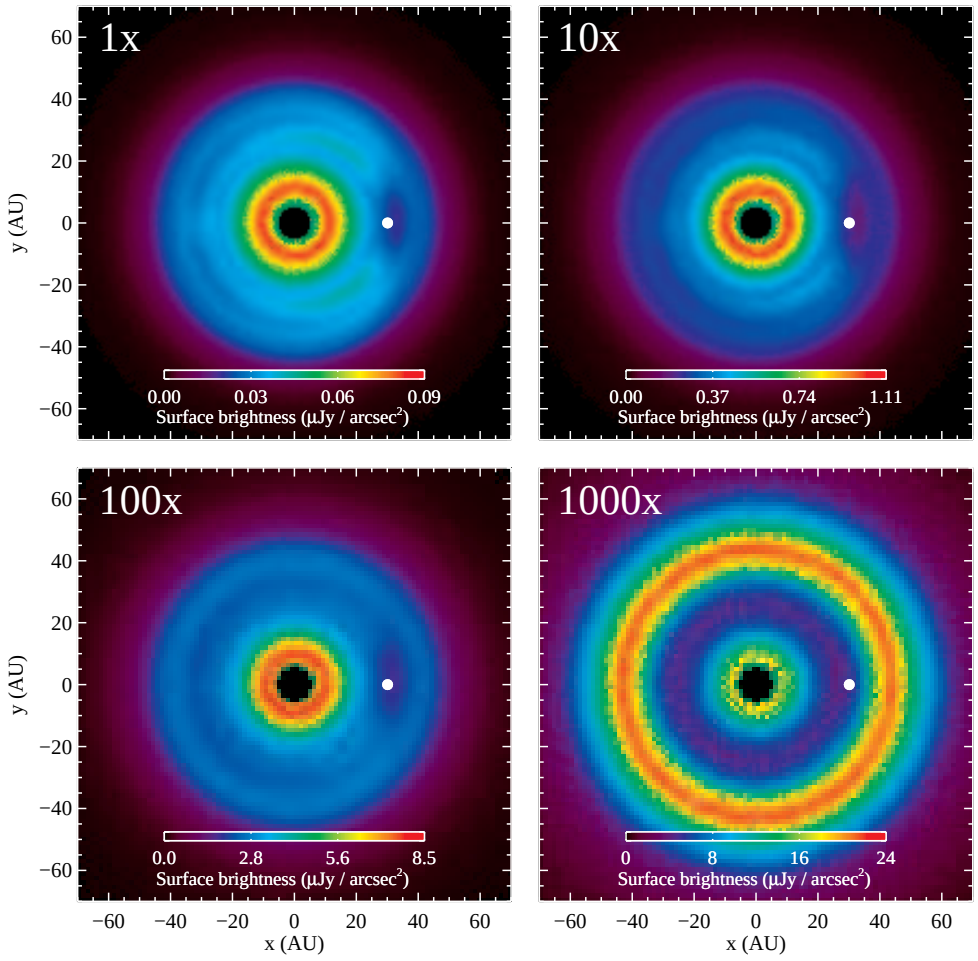

Figure 5.7: Images of the collisional dust models in optical wavelengths. The dot indicates the location of Neptune. The four models show the appearance of the Solar System assuming Kuiper Belt dust clouds with optical depths of roughly 1×, 10×, 100×, and 1000× that of today's Kuiper Belt dust cloud. A transition occurs at the 100× model, where $\tau \approx v/c$ in the Kuiper Belt.

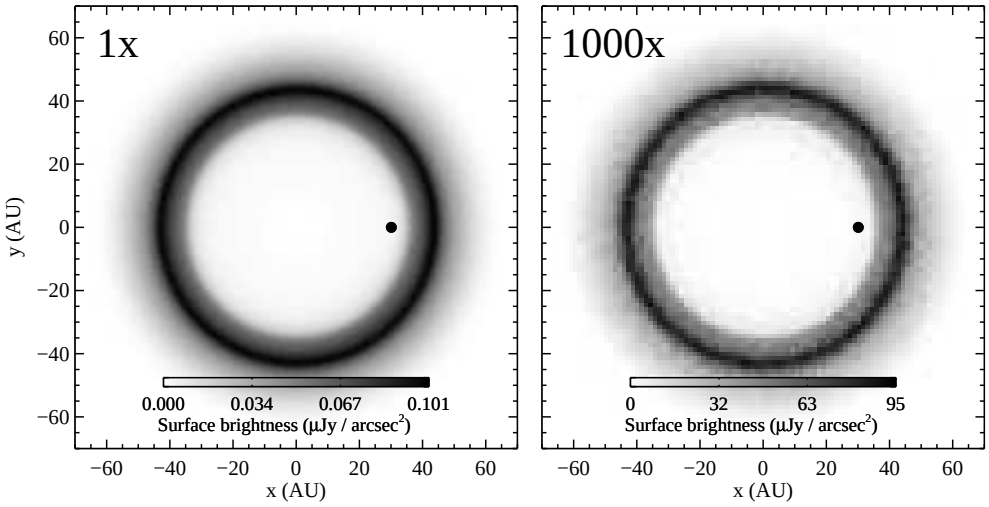

Figure 5.8: Images of the collisional KB dust models, KB×1 and KB×1000, at submillimeter wavelengths. The dot indicates the location of Neptune.

azimuthally-symmetric rings at an optical depth of τ_r (i.e., 10^{-4}–10^{-6}).

Our simulations also reveal a phenomenon relatively unanticipated by previous authors: the importance of higher-order resonances ($n : n-2$, $n : n-3$, etc.) in sculpting a dusty disk. We find that even at low dust levels, the first order resonances can become saturated, because, as Stark & Kuchner (2009) demonstrated, grain-grain collision rates are higher both in and near MMRs. Also, the sources of the grains in our simulations are located near the planet in our simulations, where the MMRs are strong and dense; in many previous simulations, the grains were launched from two or three times the planet's semi-major axis. Having the sources located near the planet as we do might promote trapping in higher order MMRs.

The higher-order resonances in the forest of MMRs near a planet are associated with many different geometries. But all the geometries have a common feature: they protect a particle from very close encounters with the planet. The result is that when these resonances are populated, the ring they yield may extend inside and outside the planet's orbit, but the location of the planet is always some kind of relatively dust-free gap.

As we mentioned above, the actual dust level in the KB has never been directly measured. But our models suggest one way to measure the dust level: take images of the KB dust, e.g., from a probe in the outer Solar System, and match them to the morphology of our models. Use that data to search for a ring with the gap located at Neptune; its presence and strength would indicate the degree to which collisions remove small particles from resonances with Neptune. Looking for an azimuthal asymmetry like this one might be easier than measuring the uniform dust

background.

5.5.2 Limitations of the simulations

We have done our best to emphasize interpretations of our models that we think will be robust. However, our models represent only one step toward understanding the effect of collisions on the morphology of the Kuiper Belt dust cloud. In the next two subsections, we will discuss some of the limitations of our simulations that should be kept in mind.

Though our simulations cover three orders of magnitude in grain size, they neglect grains smaller than 1 μm. Most grains smaller than this size are ejected by radiation pressure in one dynamical timescale. However, Strubbe & Chiang (2006) showed that populations of these so-called β-meteoroids can contribute substantially to the optical depth of a debris disk, especially the region exterior to the birth ring, because they are generated in such large numbers. The absence of these small grains is probably especially important for the KB$\times$1000 model.

Some small grains ($\lesssim 1$ μm) in the Solar System originate in the interstellar medium, and fly rapidly through the Solar System on hyperbolic orbits (Yamamoto & Mukai, 1998). Collisions between KBOs and these interstellar grains can be an important source of KB dust (Yamamoto & Mukai, 1998). Our simulations do not explicitly model these high-velocity grains, which might also be important in destroying KB grains.

Our models also contain only a simplified treatment of particles larger than

about 1400 μm. We chose this cutoff because debris disks generally become too faint to image long-ward of millimeter wavelengths. Modeling large bodies in debris disks presents several complications. Their PR lifetimes may be longer than the lifetime of the system. Collisions with these bodies can produce long-lived fragments, or even enter the cratering regime. We leave this work to future simulations. We assume that these large bodies are adequately modeled as our steady sources, and we trust that smaller grains will dominate the Kuiper Belt dust images, as they dominate, e.g., the zodiacal light.

A related issue is that our treatment of collisions contains no explicit treatment of fragmentation; it assumes that all grain production is associated with the source populations. All the the explicitly modeled collisions between grains yield either complete vaporization or leave the particles unperturbed. Though we estimate that typical collision velocities are high enough (~ 0.5 km s^{-1}) to make vaporization the most common collision outcome for small icy grains, there will be some collisions gentle enough, and some grains strong enough to lead to fragmentation. Those fragments will often be β-meteoroids like those mentioned above. Fragmentation will also be associated with some dissipation of orbital energy, a process we do not model.

Our models also neglect drag from any interstellar gas. Gas drag can potentially be important for grains in the very outskirts of debris disks (e.g. Debes et al., 2009). We chose to neglect this force because we felt that adding too many new ingredients at once to these simulations might make our results too complex to for us to physically interpret. Moreover, the gas drag parameters range widely among

various stars, so including gas drag might hinder the use of our model as a baseline for comparison with other systems.

Finally, the dust cloud created by the KB may be more tenuous than current estimates, but our models do not explicitly examine the distribution of dust in disks with $\tau < 10^{-7}$. However, our results reveal several trends that allow us to qualitatively predict the appearance of such disks. First, the longer collision time associated with a more tenuous disk would allow larger grains to penetrate farther into the inner regions of the disk, creating a disk with a more uniform radial distribution of grain sizes interior to the birth ring. Fewer collisions would also enhance the number of grains in MMRs relative to the background cloud, leading to a disk with more well-defined resonant ring structures. The dip in the grain size distribution would decrease in amplitude, more closely resembling the Dohnanyi power law. Finally, the submillimeter images may start to show hints of structure as the largest grains have time to become resonantly trapped before their collisional destruction.

5.5.3 Input parameters and interpretation

Our models of the Kuiper Belt, scaled up in mass, move beyond simple linear scalings, helping us compare the Kuiper Belt to extrasolar debris disks. But this comparison remains far from perfect. Other debris disks, for example, are not the same age as the Kuiper Belt; they could represent younger systems populated by source bodies that will soon vanish via collisions and orbital instabilities. Or they

could contain planets in the process of migration; this process could influence the morphology of a debris cloud (Wyatt, 2003; Murray-Clay & Chiang, 2005). A few debris disks might even represent a transient event, perhaps analogous to late heavy bombardment in the Solar System (Booth et al., 2009).

Another important point is that the source distributions we chose might not be a good representation of the actual distribution of dust sources in the Kuiper Belt. First of all, the distribution of KBOs is not completely known. For example, there is a strong bias toward detecting KBOs with small perihelion distances, so we do not yet have a good inventory of dynamically-cold KBOs beyond about 46 AU. Since, according to our simulations, the dynamically cold KBOs contribute most of the particles trapped in MMRs, this lack of knowledge hampers our ability to predict the population of dust in the 2:1 MMR with Neptune ($\sim$ 48 AU), and any MMRs exterior to that.

But, even if we knew the exact orbital distribution of KBOs, down to, say 1 km in size, this distribution would not correspond exactly to where the KB dust is launched from, i.e., where recent KBO collisions have occurred. Some dust production in the KB occurs when ISM grains hit KBOs (Yamamoto & Mukai, 1998); our source populations probably represent this mechanism well. But if the KB is like the asteroid belt, then some dust production is probably associated with collisional families, perhaps like the Haumea family (Brown et al., 2007). Therefore, for the time being, it seems appropriate that we content ourselves with simple parametric source distributions, inspired by KBO observations, like those we used here.

5.6 Conclusions

We modeled the 3-D dust distribution in the Kuiper Belt taking into account perturbations from Jupiter, Saturn, Uranus and Neptune, the simultaneous destruction of dust grains via collisions, and the interaction of these two phenomena, including the enhanced destruction of grains in mean motion resonances. We demonstrated the capabilities of the collisional grooming algorithm for approximately reproducing the Dohnanyi (1969) collisional equilibrium size distribution—though resonant trapping tends to modify the size distribution in a resonant ring. The dust level in the KB has never been directly measured; we suggested that one way to measure the dust level would be matching images of the KB dust, e.g., from a probe in the outer Solar System, to the morphology of our models. Searching for a ring with the gap at Neptune in this manner might be easier than measuring the uniform dust background.

Here are the primary conclusions we have drawn from our models, about the Kuiper Belt dust population itself and about debris disks in general.

- An observer looking at the KB dust $\times 1000$ in visible light from afar would mostly see a wide ring at 7-13 AU with an optical depth of $\sim 10^{-5}$ (Figure 5.7). This ring consists of grains with $s \leq s_c$, trapped in the 2:1, 3:2, and other MMRs with Saturn. This secondary central ring of small dust grains may be analogous to the hot central dust cloud seen around Fomalhaut (Stapelfeldt et al., 2004; Absil et al., 2009).

- An observer looking at the KB dust from a nearby star at submillimeter wave-

lengths would probably see an azimuthally-symmetric ring of large grains at 42-45 AU. This ring consists of large grains, > 100 μm in size, associated with the cold classical Kuiper Belt. This submillimeter morphology barely changes as the optical depth is increased over a factor of 1000 (Figure 5.8).

- At lower optical depths, KB dust $\times 10$ or KB dust $\times 1$, the above features persist, and a new component appears at optical wavelengths: a ring of dust in Neptune's orbit, trapped in MMRs with Neptune. This dust occupies two size ranges: large grains originating from plutino parent bodies in Neptune's 3:2 MMR, and and smaller grains with $s \sim s_c$, released outside resonance, and then trapped in MMRs. This ring has a gap at Neptune's location—indicating the current position of the planet. It resembles two rings in optical images because of the central illumination.

- Mean motion resonances can contribute strongly to the appearance of debris disks, despite previous suggestions to the contrary. They contribute in two major ways: 1) large bodies that dominate the submillimeter images remain near their source, which may itself be resonant, like the Plutinos. 2) smaller grains become trapped in MMRs as they spiral into the star. Though the small-grain dust population of the first-order resonances can saturate in the presence of collisions, these smaller particles also interact with a forest of higher-order MMRs. The higher-order MMRs also serve to create a ring-like structure near the orbit of the perturbing planet.

- At high optical depths, debris disk images are likely dominated by the birth

ring, the source of the particles. But at optical depths below $\tau_r \sim v/c$, small dust grains trapped in mean motion resonances can dominate the images. Here v is the local Keplerian speed, and c is the speed of light.

- Dust released by plutinos makes a negligible contribution to the resonant structure in the Kuiper Belt cloud. There are two reasons for this new result: 1) The population of plutinos is a smaller fraction of the dust cloud than previously realized (Hahn & Malhotra, 2005). 2) The grains that dominate optical images tend to be near the critical size, and those grains lose memory of the orbits of their source particles.

- Grain-grain collisions are important in shaping the Kuiper Belt dust cloud, even at an optical depth of 10^{-7}. For example, the interplay between collisions, PR drag, and mean motion resonances sets the dominant grain size in the Kuiper Belt.

Our simulations show us how an analog of the Solar System might appear at a distance of 10 pc, depending on how much dust there actually is in the Kuiper Belt. They illustrate how our changing picture of the KBO orbital distribution has changed our picture of the KB dust. They represent the first self-consistent 3-D model of the Kuiper Belt dust morphology that incorporates both planet-dust interactions and grain-grain collisions.

However, our models leave many potentially important questions unanswered. How do β meteoroids, interstellar grains, and fragmentation of small grains affect the appearance of the KB disk? How do collisional families and other transient

phenomena influence the KB dust?

We expect that the next generation of models, together with more observations of the Kuiper Belt and other debris disks, will help answer these questions and refine our understanding of resonant structures in disks. Two observational goals stand out that would especially help us take the next steps with our models: 1) we would like to know the population of KBOs in the 2:1 MMR with Neptune at low eccentricity, and 2) we would like to have more resolved images of debris disks with low optical depth ($\lesssim 10^{-5}$) where the collisional physics is relatively simple. We expect that survey telescopes like the Large Synoptic Survey Telescope (LSST) may help achieve the first goal, and that deep submillimeter and coronagraphic imaging of debris disks, e.g. with the with the Atacama Large Millimeter Array (ALMA) and the James Webb Space Telescope (JWST), should help attain the second.

Chapter 6

Conclusions & discussion

To date, the majority of resolved debris disks show radial and/or azimuthal structures. My investigations into the structure of debris disks reveal that structures can arise from and be affected by a variety of mechanisms, including, but not limited to, MMR trapping of dust grains or planetesimals, ejection of dust grains by massive planets, radial size-sorting of dust grains by collisions, and the interplay between collisions and dust trapped in MMRs.

Our spatially resolved KIN measurements of the debris disk around 51 Oph, combined with VLTI-MIDI observations and a Spitzer IRS spectrum, reveal a dust distribution with two components: a hot inner exozodiacal disk of large grains and an outer cool disk of small silicate grains. Our preferred model of the 51 Oph disk is consistent with an inner "birth" disk of continually colliding parent bodies producing an extended envelope of ejected small grains. This picture resembles the disks around Vega, AU Microscopii, and β Pictoris, supporting the idea that 51 Oph may be a β Pictoris analog.

Will future missions be able to detect fine structure, like resonant rings, in exozodiacal clouds similar to that around 51 Oph? My collisionless simulations showed that terrestrial-mass planets can create resonant ring structures with contrasts $\sim$10:1 for grain sizes $\sim$100 μm. Although my collisional simulations demonstrate that col-

lisions tend to remove grains in and near resonances, reduce the appearance of asymmetries within the cloud, and prevent large grains from spiraling into regions of resonance, there will likely be conditions under which these ring structures are still highly contrasted and detectable. For example, the semi-major axes of parent bodies' orbits may be just exterior to a planet's first order MMRs, or within them, making for quick capture of the large grains. Parent bodies could also occupy orbits with smaller inclinations and eccentricities, producing dynamically cold dust that is trapped with greater probability. Future models of collisional exozodiacal clouds, processed with simulators of proposed exoplanet-imaging missions, should answer this question.

Exozodiacal resonant ring structures may even be detected by other means prior to the launch of an exo-Earth-imaging mission. The dust in our zodiacal cloud and other debris disks has proven to be fairly forward-scattering at visible wavelengths. For a disk viewed at moderate inclination, the disk-integrated scattered light will change in amplitude as the clumpy, asymmetric resonant ring structure rotates in lock with the perturbing planet; a resonant ring adds a variable signature to a star's light curve with a period equal to the planet's orbital period. My preliminary collisionless simulations estimate this signal's amplitude $\sim 10^{-7}$ for a 1 zodi dust cloud inclined 60° from face-on. Models of collisional exozodiacal disks are necessary to determine whether more dense ring structures could create a signal $\sim 10^{-5}$, possibly detectable with the transit-detecting Kepler mission.

My analysis of resonant rings produced by terrestrial-mass planets in collisionless disks shows that we may be able to use the morphology of ring structures to

constrain the planet mass, planet semi-major axis, and dominant dust grain size, even if the planet is not detectable. I provide simple analytic expressions to do so. However, interpretation of these resonant rings will be hindered by a morphological degeneracy for systems with similar ratios of $\sqrt{a_{\rm p}}$ to β for the grain size that dominates the optical depth of the resonant ring. Although the effects of collisions may further complicate our interpretation of these structures, I showed that to first order we can equate the PR time and collision time to estimate the dominant grain size in a resonant ring, s_c.

Will asymmetries in resonant ring structures obscure the detection of exo-Earths? This question can only be answered by simulating the response of specific, proposed exo-Earth imaging missions to collisional, multi-grain-size models of exozodiacal cloud structures. I am currently creating such models. I will synthesize images of these disk models with proposed internal coronagraphs, like PIAA, and external occulters, like NWO. I will investigate the degree to and conditions under which the planet signal can become lost in the surrounding disk and look for methods by which we can separate the planet's signal from the disk's. We may be able to exploit differences in color between the planet and disk to separate the signals. However, as I showed in Figure 4.9, the resonant ring morphology changes with grain size, and thus does not exhibit a uniform color.

We can apply the collisional models I have developed to currently-detectable dust structures in the outer $\sim$100 AU of planetary systems, such as Fomalhaut and ϵ Eridani. But what can we learn from our models about the architectures of these systems? To answer this question I started with a system whose architecture we

already know fairly well, the Solar System, and simulated the dust disk generated by the Kuiper Belt. I found that the large grains dominate the submillimeter images of the Kuiper Belt, which would appear as a uniform ring at 40–45 AU. Visible wavelengths reveal a resonant ring structure in lock with Neptune. Neptune resides in a gap within the resonant ring, a tell-tale signature of a planet.

From afar, a much more dense version of the Kuiper Belt dust cloud (scaled up to 1000 times the current optical depth) would look morphologically similar to the current Kuiper Belt at submillimeter wavelengths. However, at visible wavelengths the KB $\times$1000 model no longer exhibits a resonant ring created by Neptune, which is removed by grain-grain collisions almost entirely. Instead, optical images would reveal two distinct rings: one at 7–13 AU and another at 40–45 AU. The outer ring is dominated by large grains > 20 μm in size, mostly associated with the cold classical Kuiper Belt. The inner ring consists of small dust grains $\lesssim 5$ μm in size in MMRs with Saturn.

The KB $\times$1000 simulations demonstrate that even in disks with very dense "birth" rings of dust, the smallest grains can quickly migrate inward and escape the highly collisional birth ring. These small grains can continue to spiral inward in a region of reduced collision rates and interact with interior planets, possibly forming resonant ring structures. This process can form inner regions of warm dust that are dynamically linked to the outer disk, and may help explain the hot inner dust disk observed around Fomalhaut.

Collisional models of the outer regions of exoplanetary systems will be helpful in understanding the architecture of currently observed debris disks and disks to be

observed in the near future. However, the hot, cold, and plutino components of my KB dust model show that the appearance of a dust cloud depends strongly on the distribution of parent bodies. Before we can interpret the dust distribution in an observed, highly-collisional debris disk with any degree of confidence, we need to better understand the possible distributions of parent bodies and their affect on the morphology of the dusty debris disk.

Bibliography

A'Hearn, M. F., et al. 2005, Science, 310, 258

Absil, O., Mennesson, B., Le Bouquin, J.-B., Di Folco, E., Kervella, P., & Augereau, J.-C. 2009, ApJ, 704, 150

Agol, E. 2007, MNRAS, 374, 1271

Augereau, J. C., Nelson, R. P., Lagrange, A. M., Papaloizou, J. C. B., & Mouillet, D. 2001, A&A, 370, 447

Backman, D. E., & Paresce, F. 1993, in Protostars and Planets III, ed. E. H. Levy & J. I. Lunine (Tucson: Univ. Arizona Press), 1253

Backman, D. E., Dasgupta, A., & Stencel, R. E. 1995, ApJ, 450, 35

Barry, R. K., et al. 2008, ApJ, 677, 1523

Beaulieu, J.-P., et al. 2006, Nature, 439, 437

Beaugé, C., & Ferraz-Mello, S. 1994, Icarus, 110, 239

Beckwith, S. V. W. 2007, preprint (arXiv:0710.1444v2)

Beichman, C. A. 1996, A Road Map for the Exploration of Neighboring Planetary Systems (JPL Publication 96-22)

Beichman, C. A., Woolf, N. J., & Lindensmith, C. A. 1999, The Terrestrial Planet Finder: Origins of Stars, Planets, and Life (JPL Publication 99-3)

Beichman, C. A., et al., 2006, ApJ, 639, 1166

Berthoud, M. G., Keller, L. D., Herter, T. L., Richter, M. J., & Whelan, D. G. 2007, ApJ, 660, 461

Binney, J., & Tremaine, S. 1987 Galactic Dynamics (3rd ed.; Princeton, NJ: PUP)

Booth, M., Wyatt, M. C., Morbidelli, A., Moro-Martin, A., & Levison, H. F. 2009, MNRAS, 399, 385

Brandeker, A., Liseau, R., Olofsson, G., & Fridlund, M. 2004, A&A, 413, 681

Bromley, B. C., & Kenyon, S. J. 2006, AJ, 131, 2737

Brown, M. E. 2001, AJ, 121, 2804

Brown, M. E., Barkume, K. M., Ragozzine, D., Schaller, E. L. 2007, Nature, 446, 294

Brownlee, D., et al. 2006, Science, 314, 1711

Bryden, G., et al. 2006, ApJ, 636, 1098

Burns, J. A., Lamy, P. L., & Soter, S. 1979, Icarus, 40, 1

Cellino, A., Michel, P., Tanga, P., Zappala, V., Paolicchi, P., & DellOro, A. 1999, Icarus, 141, 79

Chambers, J. E. 1999, MNRAS, 304, 793

Charnoz, S., & Morbidelli, A. 2003, Icarus, 166, 141

Chiang, E. I., & Goldreich, P. 1997, ApJ, 490, 368

Chiang, E. I. et al. 2003, AJ, 126, 430

Chiang, E., Kite, E., Kalas, P., Graham, J. R., & Clampin, M. 2009, ApJ, 693, 734

Clampin, M., et al. 2003, AJ, 126, 385

Colavita, M. M., et al. 2008, in Proc. SPIE 7013, Optical and Infrared Interferometry, ed. M. Schöller, W. C. Danchi, & F. Delplancke, 70130A

Debes, J. H., Weinberger, A. J., & Schneider, G. 2008, ApJ, 673, L191

Debes, J. H., Weinberger, A. J., & Kuchner, M. J. 2009, ApJ, 702, 318

Defrère, D., Absil, O., Coudé du Foresto, V., Danchi, W. C., den Hartog, R. 2008, A&A, 490, 435

Defrère, D., Absil, O., den Hartog, R., Hanot, C., Stark, C. C. 2010, A&A, 509, 9

Deller, A. T., & Maddison, S. T. 2005, ApJ, 625, 398

Dermott, S. F., Jayaraman, S., Xu, Y. L., Gustafson, B. Å. S., & Liou, J. C. 1994, Nature, 369, 719

Dermott, S. F., Nicholson, P. D., Burns, J. A., & Houck, J. R. 1985, in Properties and interactions of interplanetary dust, ed. R. H. Giese & P. Lamy (Dordrecht: D. Reidel Publishing Co.), 395

Dermott, S. F., Nicholson, P. D., Burns, J. A., & Houck, J. R. 1984, Nature, 312, 505

Doering, R. L., Meixner, M., Holfeltz, S. T., Krist, J. E., Ardila, D. R., Kamp, I., Clampin, M. C., & Lubow, S. H. 2007, AJ, 133, 2122

Dohnanyi, J. S. 1969, J. Geophysical Research, 74, 2531

Draine, B. T., & Lee, H. M. 1984, ApJ, 285, 89

Dullemond, C. P., Dominik, C., & Natta, A. 2001, ApJ, 560, 957

Duncan, M. J., Levison, H. F., & Lee, M. H. 1998, AJ, 116, 2067

Dunkin, S. K., Barlow, M. J., & Ryan, S. G. 1997, MNRAS, 286, 604

Durda, D. D., Flynn, G. J., Sandel, L. E., & Strait, M. M. 2007, in ESA SP-643, Workshop on Dust in Planetary Systems, ed. H. Krueger & A. Graps, 77

Fajardo-Acosta, S. B., Telesco, C. M., & Knacke, R. F. 1993, ApJ, 417, 33

Fixsen, D. J., & Dwek, E. 2002, ApJ, 578, 1009

Golimowski, D., et al. 2006, AJ, 131, 3109

Grady, C. A., & Silvis, J. M. S. 1993, ApJ, 402, 61

Greaves, J. S., et al. 1998, ApJ, 506, 133

Greaves, J. S., Wyatt, M. C., Holland, W. S. & Dent, W. R. F. 2004, MNRAS, 351, L54

Grigorieva, A., Artymowicz, P., & Thébault, P. 2007, A&A, 461, 537

Gustafson, B. Å. S. 1994, Annu Rev. Earth Planet. Sci., 22, 553

Hahn, J. M., & Malhotra, R. 2005, AJ, 130, 2392

Heap S., et al. 2000, ApJ, 539, 435

Henrard, J. 1982, Celest. Mech., 27, 3

Holland, S., et al. 1998, Nature, 392, 788

Holmes, E. K., Dermott, S. F., Gustafson, B. Å. S. & Grogan, K. 2003, ApJ, 597, 1211

Ipatov, S. I., Kutyrev, A. S., Madsen, G. J., Mather, J. C., Moseley, S. H., & Reynolds, R. J. 2008, Icarus, 194, 769

Jackson, A. A., & Zook, H. A. 1989, Nature, 337, 629

Jayawardhana, R., Fisher, R. S., Telesco, C. M., Piña, R. K., Barrado y Navascués, D., Hartmann, L. W., & Fazio, G. G. 2001, AJ, 122, 2047

Jewitt, D., Moro-Martin, A., Lacerda, P. 2009, Astrophysics in the Next Decade, Astrophysics and Space Science Proceedings, Springer Netherlands, p. 53

Kalas, P., Graham, J. R., & Clampin, M. 2005, Nature, 435, 1067

Kalas, P., et al. 2008, Science, 322, 1345

Kavelaars, J. J., Jones, L., Gladman, B., Parker, J. W., & Petit, J. M. 2008, in The Solar System Beyond Neptune, M. A. Barucci, H. Boehnhardt, D. P. Cruikshank, and A. Morbidelli (eds.), University of Arizona Press, Tucson, p.59

Kavelaars, J. J., et al. 2009, AJ, 137, 4917

Keller, L. D., et al. 2008, ApJ, 684, 411

Kelsall, T., et al. 1998, ApJ, 508, 44

Kenyon, S. J., & Bromley, B. C. 2001, AJ, 121, 538

Krivov, A. V., Löhne, T., & Sremčević, M. 2006, A&Ap, 455, 509

Krivov, A. V., Queck, M., Löhne, T., Sremčević, M. 2007, A&Ap, 462, 199

Krivov, A. V., Sremčević, M., & Spahn, F. 2005, Icarus, 174, 105

Krüger, H., et al. 1999, Planet. Space Sci., 47, 363

Kuchner, M. J., & Holman, M. J. 2003, ApJ, 588, 1110

Landgraf, M., Liou, J.-C., Zook, H. A., & Grün, E. 2002, AJ, 123, 2857

Lawler, S. M. et al. 2009, ApJ, 705, 89

Lawson, P. R., & Traub, W. A. 2006, NASA Navigator Science Plan

Lecavelier des Etangs, A., et al. 1997, A&A, 321, 39

Leinert, Ch., et al. 2004, A&A, 423, 537

Leinhardt, Z. M., Richardson, D. C., Lufkin, G., & Haseltine, J. 2009, MNRAS, 396, 718

Levine, M., Shaklan, S., & Kasting, J. 2006, Terrestrial Planet Finder Coronagraph: Science and Technology Definition Team (STDT) Report (JPL Publication D-34923)

Liou, J. C., Dermott, S. F., & Xu, Y. L. 1995, Planet. Space Sci., 43, 717

Liou, J. C., & Zook, H. A. 1999, AJ, 118, 580

Löhne, T., Krivov, A. V., Rodmann, J. 2008, ApJ, 673, 1123

Low, F. J., et al. 1984, ApJ, 278, 19L

Lunine, J. I., et al. 2008, Astrobiology, 8, 875

Mann, I., Krivov, A., & Kimura, H. 2000, Icarus, 146, 568

Meeus, G., Waters, L. B. F. M., Bouwman, J., van den Ancker, M. E., Waelkens, C., & Malfait, K. 2001, A&A, 365, 476

Michel, P., & Valsecchi, G. B. 1996, CeMDA, 65, 355

Monnier, J. D., et al. 2009, ApJ, submitted

Moran, S. M., Kuchner, M. J., & Holman, M. J. 2004, ApJ, 612, 1163

Moro-Martín, A., & Malhotra, R. 2002, AJ, 124, 2305

Moro-Martin, A., & Malhotra, R. 2003, AJ, 125, 2255

Murray-Clay, R. A., & Chiang, E. I. 2005, ApJ, 619, 623

Muzerolle, J., D'Alessio, P., Calvet, N., & Hartmann, L. 2004, ApJ, 617, 406

Nesvorny, D., Jenniskens, P., Levison, H. F., Bottke, W. F., & Vokrouhlicky, D., 2009, preprint (arXiv:0909.4322)

Perryman, M. A. C., et al. 1997, A&A, 323, L49

Queck, M., Krivov, A. V., Sremčević, M., & Thébault, P. 2007, Celestial Mechanics and Dynamical Astronomy, 99, 169

Quillen, A. C. 2006, MNRAS, 372, L14

Reach, W. T., et al. 1995, Nature, 374, 521

Reach, W. T., Lisse, C., von Hippel, T., Mullally, F. 2009, ApJ, 693, 697

Reche, R., Beust, H., Augereau, J.-C., & Absil, O. 2008, A&A, 480, 551

Roberge, A., Feldman, P. D., Lecavelier des Etangs, A., Vidal-Madjar, A., Deleuil, M., Bouret, J.-C., Ferlet, R., & Moos, H. W. 2002, ApJ, 568, 343

Roberge, A., et al. 2009, Astro2010: The Astronomy and Astrophysics Decadal Survey, Science White Papers, no. 250.

Robertson, H. P. 1937, MNRAS, 97, 423

Schneider, G., Weinberger, A. J., Becklin, E. E., Debes, J. H., Smith, B. A. 2009, AJ, 137, 53

Schramm, L. S., Brownlee, D. E., & Wheelock, M. M. 1989, Meteoritics, 24, 99

Serabyn, E., et al. 2005, in Proc. SPIE 5905, Techniques and Instrumentation for Detection of Exoplanets II, ed. D. R. Coulter, 272

Stapelfeldt, K. R., et al. 2004, ApJS, 154, 458

Stark, C. C., & Kuchner, M. J. 2008, ApJ, 686, 637

Stark, C. C. & Kuchner, M. J. 2009, ApJ, 707, 543

Stark, C. C., et al. 2009, ApJ, 703, 1188

Stern, A. 1996, A&Ap, 310, 999

Strubbe, L. E., & Chiang, E. I. 2006, ApJ, 648, 652

Su, K. Y. L., et al. 2005, ApJ, 628, 487

Telesco, C. M., et al., 2000, ApJ, 530, 329

Thébault, P., Augereau, J. C., & Beust, H. 2003, A&A, 408, 775

Thi, W.-F., van Dalen, B., Bik, A., & Waters, L. B. F. M. 2005, A&A, 430, 61

Tatulli, E., et al. 2008, A&A, 489, 1151

Trilling, D. E., et al. 2008, ApJ, 674, 1086

Trujillo, C. A. & Brown, M. E. 2001, ApJ, 554, 95

van den Ancker, M. E., Meeus, G., Cami, J., Waters, L. B. F. M., & Waelkens, C. 2001, A&A, 369, 17

Waters, L. B. F. M., Coté, J., & Geballe, T. R. 1988, A&A, 203, 348

Weidenschilling, S. J., & Cuzzi, J. N. 1993, in Protostars and Planets III, ed. E. H. Levy & J. I. Lunine, 1031

Wilner, D. J., Holman, M. J., Kuchner, M. J., & Ho, P. T. P. 2002, ApJ, 569, L115

Wisdom, J. 1980, AJ, 85, 1122

Wyatt, M. C. 1999, Ph.D. Thesis, University of Florida

Wyatt, M. C. 2003, ApJ, 598, 1321

Wyatt, M. C. 2005, A&A, 433, 1007

Wyatt, M. C. 2006, ApJ, 639, 1153

Wyatt, M. C., Smith, R., Su, K. Y. L., Rieke, G. H., Greaves, J. S., Beichman, C. A., & Bryden, G. 2007, ApJ, 663, 365

Wyatt, M. C., Dermott, S. F., Telesco, C. M., Fisher, R. S., Grogan, K., Holmes, E. K., & Piña, R. K. 1999, ApJ, 527, 918

Wyatt, M. C., Smith, R., Su, K. Y. L., Rieke, G. H., Greaves, J. S., Beichman, C. A., & Bryden, G. 2007, ApJ, 663, 365

Wyatt, S. P., & Whipple, F. L. 1950, ApJ, 111, 134

Yamamoto, S. & Mukai, T. 1998, A&Ap, 329, 785

Zolensky, M. E., et al. 2006, Science, 314, 1735

Zuckerman, B. 2001, ARA&A, 39, 549